Czech Technical University in Prague
Faculty of Electrical Engineering
Department of Electromagnetic Field

Modal Approach for Antenna Design

Doctoral Thesis

Jan Eichler

Prague, March 2014

Ph.D. Programme: Electrical Engineering and Information Technology
Branch of study: Radioelectronics

Supervisor: Doc. Ing. Pavel Hazdra, Ph.D.
Supervisor specialist: Prof. Ing. Miloš Mazánek, CSc.

To my wife Olga and all members of my family.

Acknowledgement

In the first place, I would like to express my sincere gratitude to my supervisor Dr. Pavel Hazdra, associate professor at the CTU in Prague, for his guidance and inspiring opinions throughout my studies and I fully appreciate the freedom he gave me in every aspect of my doctoral work. I would also like to thank my fellow doctoral candidate Miloslav Čapek for sharing new ideas, fruitful discussions and careful reading of my manuscripts. I also thank to Prof. Miloš Mazánek for his advices and the leadership of the department.

I am also grateful to Dr. Lukáš Jelínek for sharing his pure physical and mathematical understanding of electrodynamics and to Dr. Vratislav Sokol from whom I learned to treat challenging problems in a systematic way.

It was a pleasure to work in such a friendly collective of the Department of electromagnetic field. Many of my colleagues helped me with particular problems in the field of their expertise. I would also like to thank to Prof. Daniel Segovia-Vargas for a pleasant and productive time during my secondment at the Carlos III University in Madrid.

Last but not least, I express my deepest appreciation to my beloved wife Olga, who always supported me and believed in my abilities. My sincere thanks go to my parents, my sister, Olga's parents, sister, and brother for their care, patience, and encouragement.

Abstrakt

Efektivní numerická analýza vyzařujících struktur je předmětem výzkumu již několik dekád a s rostoucí popularitou bezdrátové komunikace se její aplikace dále vyvíjejí. Pro velké a komplexní struktury jsou jsou velmi významné metody umožňující separaci jednotlivých částí vysokofrekvenčního zařízení, nebo poskytující hlubší pochopení fyzikálních principů. Mezi takovéto přístupy patří i modální metody.

Tato práce se zabývá teorií charakteristických modů, která definuje množinu funkcí, ortogonálních vzhledem k vyzářenému výkonu, která je jednoznačně definovaná geometrií vyzařující struktury. Klíčovou vlastností je, že pro dostatečně přesný popis vyzářeného pole elektricky malé a středně velké struktury, obvykle postačuje pouze několik modů. Charakteristické mody již byly použity pro návrh různých typů antén, mimo jiné MIMO, širokopásmových, nebo elektricky malých antén.

V této disertační práci je popsán kompletní návrh, začínající specifikací anténních parametrů až po vyrobený a změřený prototyp dvoupásmové planární antény pomocí teorie charakteristických modů. Závislost modální resonanční frekvence a vyzařovacího činitele jakosti na rozložení proudové hustoty a výšce nad nekonečnou elektricky vodivou rovinou je vysvětlena na základě informace poskytnuté modální analýzou. Dále je prezentován prototyp aktivní, diferenčně napájené antény, včetně měření diferenčních rozptylových parametrů. Přednosti, omezení a možnosti použití charakteristických modů jsou diskutovány s ohledem na návrh aktivních diferenčně napájených antén.

V rámci disertace byl vyvinut nástroj pro tvorbu povrchové mříže, který spolupracuje s modálním řešičem vyvíjeným na Katedře elektromagnetického pole FEL ČVUT a umožňuje efektivní analýzu parametrizovaných antén. Bylo ukázáno, že nástroj je flexibilní a vhodný pro implementaci nových výzkumných přístupů souvisejících s numerickým výpočtem charakteristických modů. Práce popisuje vliv chyby numerické integrace a aproximační chyby na numerický výpočet charakteristických modů pomocí metody momentů. Provedená odvození byla verifikována numerickou konvergencí resonanční frekvence, činitele jakosti a maximální

směrovosti s rostoucí hustotou mříže. Na základě analýzy chyb byla formulována doporučení pro postup zahuštění mříže, která byla aplikována na modální řešič a také na komerční implementaci v programu FEKO.

Byla odvozena metoda výpočtu vazebních a budicích modálních koeficientů pro elektricky vázané struktury. Metoda vykazuje velmi dobrou shodu s přímým řešení integrální rovnice pro elektrické pole.

Abstract

Effective numerical analysis of radiating structures has been a relevant topic over the last few decades and applications are constantly being developed as wireless communications become increasingly popular. For large and complex structures, methods which can separate the independent effects of particular parts of a high-frequency device, or provide deeper understanding of physical principles are of great interest. One class of such methods are the modal methods.

This thesis deals with the theory that when uniquely defined by the scattering surface, characteristic modes for conducting bodies define a complete set of basis functions orthogonal with respect to radiated power. The key property is that only a small number of modes for electrically small and intermediate bodies usually suffices to characterize the radiated or scattered fields with sufficient accuracy. These modes have already been used for various antenna designs, such as multiple-input multiple-output, ultra-wideband, and electrically small amongst others.

A complete work-flow from antenna specifications to the final manufactured and measured dual-band antenna using modal information is presented in this thesis. The characteristic modes are used to interpret the effect of current distribution and height over an infinite conducting plane on a modal resonant frequency and radiation quality factor. A prototype of a low-noise active differential antenna, including differential S-parameters measurements, is described. The strengths, weaknesses and possible usage of characteristic modes are discussed with respect to active differentially fed antenna application.

To enable the efficient analysis of various antenna geometries, a tool for surface mesh generation was developed to be used in conjunction with an in-house modal analyzer. The tool was shown to be versatile and suitable for implementing new research approaches related to the numerical aspects of computation of characteristic modes. The effect of quadrature errors on the numerical computation of characteristic modes by the method of moments is described. The derivations have been verified by the numerical convergence of modal

resonant frequency, radiation quality factor and maximal directivity with increased mesh density. Recommendations for mesh refinement strategy, based on the error analysis, have been successfully applied to the in-house tool, as well as to a commercial FEKO package.

A method of computing modal excitation coefficients for capacitely coupled conducting bodies has been derived and good agreement between the proposed and direct electric field integral equation solution was observed.

List of Publications

Journal Papers

- M. Capek, L. Jelinek, P. Hazdra, and **J. Eichler**, "The Measurable Q Factor and Observable Energies of Radiating Structures," *IEEE Transactions on Antennas and Propagation*, vol. 62, no. 1, pp. 311-318, Jan. 2014.

- P. Hazdra, M. Capek, and **J. Eichler**, "Comments to "Reactive Energies, Impedance, and Q Factor of Radiating Structures" by G. Vandenbosch, " *IEEE Transactions on Antennas and Propagation*, vol. 61, no. 12, pp. 6266-6267, Dec. 2013.

- M. Capek, P. Hamouz, P. Hazdra, and **J. Eichler**, "Implementation of the Theory of Characteristic Modes in MATLAB," *IEEE Antennas and Propagation Magazine*, vol. 55, no. 2, pp. 176-189, April 2013.

- **J. Eichler**, P. Hazdra, M. Capek, and M. Mazanek, "Modal Resonant Frequencies and Radiation Quality Factors of Microstrip Antennas," *International Journal of Antennas and Propagation*, vol. 2012, pp. 1-9, 2012.

- M. Capek, P. Hazdra, and **J. Eichler**, "A Method for the Evaluation of Radiation Q Based on Modal Approach," *IEEE Transactions on Antennas and Propagation*, vol. 60, no. 10, pp. 4556-4567, Oct. 2012.

- **J. Eichler**, P. Hazdra, M. Capek, T. Korinek, and P. Hamouz, "Design of a Dual-band Orthogonally Polarized L-probe-fed Fractal Patch Antenna Using Modal Methods," *IEEE Antennas Wireless Propag. Lett.*, vol. 10, pp. 1389-1392, 2011.

- P. Hazdra, M. Capek, and **J. Eichler**, "Radiation Q-factors of Thin-wire Dipole Arrangements," *IEEE Antennas Wireless Propag. Lett.*, vol. 10, pp. 556-560, 2011.

- M. Capek, P. Hazdra, P. Hamouz, and **J. Eichler**, "A Method For Tracking Characteristic Numbers and Vectors," *Progress In Electromagnetics Research B*, vol. 33, pp. 115-134, 2011.

Journal Papers (in review)

- M. Capek, L. Jelinek, P. Hazdra, and **J. Eichler**, "An Analytical Evaluation and The Lower Bounds of The Measurable Quality Factor Q_Z," *IEEE Antennas and Propagation Magazine* (in review).

- P. Hazdra, M. Capek, **J. Eichler**, and M. Mazanek, "The Radiation Q-Factor of a $\lambda/2$ Dipole Above Ground Plane," *IEEE Antennas Wireless Propag. Lett.* (in review)

- **J. Eichler**, P. Hazdra, and M. Capek, "Aspects of Mesh Generation for Characteristic Mode Analysis," *IEEE Antennas and Propagation Magazine* (in review).

- M. Capek, **J. Eichler**, and P. Hazdra, "Evaluation of Radiation Efficiency from Characteristic Currents," *IET Microw. Antennas Propag.* (in review)

- P. Hamouz, P. Hazdra, M. Capek, **J. Eichler**, A. Diallo, F. Ferrero, and C. Luxey, " Polarization Diversity in UMTS Mobile Phones analyzed with Characteristic Modes," *IEEE Antennas Wireless Propag. Lett.* (in review)

Conference Papers

- M. Capek, L. Jelinek, P. Hazdra, and **J. Eichler**, "The Source Definition of The Quality Factor Q_Z," *IEEE International Symposium on Antennas and Propagation and USNC-URSI Radio Science Meeeting*, 2014, Memfis, USA.

- L. Jelinek, M. Capek, P. Hazdra, **J. Eichler**, "Lower Bounds of the Quality Factor Q_Z, " *IEEE International Symposium on Antennas and Propagation and USNC-URSI Radio Science Meeeting*, 2014, Memfis, USA.

- M. Capek, P. Hazdra, **J. Eichler**, P. Hamouz, and M. Mazanek, "Acceleration Techniques in Matlab for EM Community," in *Proceedings of the 7th European Conference on Antennas and Propagation (EUCAP)*, Gothenburg, Sweden, April 2013.

- **J. Eichler**, D. Segovia-Vargas, P. Hazdra, M. Capek, and V. Gonzlez- Posadas, "Active Low Noise Differentially Fed Dipole Antenna," in *10th In- ternational Symposium on Antennas, Propagation and EM Theory (ISAPE 2012)*, 2012.

- P. Hazdra, M. Capek, **J. Eichler**, T. Korinek, and M. Mazanek, "On the Modal Resonant Properties of Microstrip Antennas, " in *Proceedings of the 6th European Conference on Antennas and Propagation (EUCAP 2012)*, pp. 1650-1654, 2012.

- M. Capek, P. Hazdra, **J. Eichler**, P. Hamouz, M. Mazanek, and V. Sobotikova, "The Evaluation of Total Radiation Q Based on Modal Approach, " in *Proceedings of the 6th European Conference on Antennas and Propagation (EUCAP)*, Prague, Czech Republic, April 2012.

- P. Hazdra, M. Capek, **J. Eichler**, P. Hamouz, and M. Mazanek, "Radiation Q of Dipole Modal Currents, " in *Proceedings of the 5th European Conference on Antennas and Propagation (EUCAP)*, Rome, Italy, pp. 1578-1581, April 2011.

- P. Hazdra, **J. Eichler**, M. Capek, P. Hamouz, and T. Korinek, "Small Dual-band Fractal Antenna with Orthogonal Polarizations, " in *Proceedings of the 5th European Conference on Antennas and Propagation (EUCAP)*, 2011.

Financial Support Acknowledgement

The research presented in the listed papers was conducted under partial finantial support of these projects:

- GACR P102/12/2223, GACR 13-09086S,

- SGS10/170/OHK3/2T/13, SGS11/065/OHK3/1T/13, SGS12/142/OHK3/2T/13,

- COST IC0603 ASSIST, COST IC1102 VISTA, COST LD12055 AMTAS,

- DG102/08/H018,

- MSM OC08018, MSM 6840770014.

List of Tables

List of Figures

List of Abbreviations

CBFM	Characteristic basis function method
CC	Common mode to common mode (S-parameters)
ChM	Characteristic mode
ChMBF	Chacteristic modes as basis functions
CM	Cavity model
CML	Coupled microstrip line
CMMR	Common mode rejection ratio
CPS	Coplanar stripline
DD	Differential mode to differential mode (S-parameters)
EFIE	Electric field integral equation
FBW	Fractional bandwidth
FCL	Fractal clover leaf
FDTD	Finite-difference time-domain
FE-BI	Finite element - boundary integral
FEM	Finite element method
FIT	Finite integration technique
IFS	Iterated functions system
LNA	Low-noise amplifier
LTCC	Low temperature cofired ceramic
MIMO	Multiple-input mutiple-output
MoM	Method of moments
MPA	Microstrip patch antenna
MS	Modal significance
PCB	Printed circuit board
PEC	Perfect electric conductor
PMC	Perfect magnetic conductor
PIFA	Planar inverted-F antenna

RWG	Rao-Wilton-Glisson (basis functions)
SAU	Self-affine "U"
UAV	Unmanned aerial vehicle
UWB	Ultra-wideband
VSWR	Voltage standing wave ratio

Contents

1

Introduction

Antenna analysis is the process of determining of an antenna's reaction to an excitation. The reactions are manifested primarily through electric and magnetic fields, or current density, which are sufficient for computing of all other antenna properties, such as input impedance or a farfield pattern. This problem is too complex for analytical solution in most practical cases, therefore numerical methods are utilized to find approximate solutions to Maxwell's equations (or equations derived from them) which will satisfy boundary and initial conditions [1, Ch. 3].

The most popular numerical techniques, such as the finite-difference time-domain (FDTD), finite element method (FEM), method of moments (MoM) or finite integration technique (FIT) have been in development for over 40 years and are available in commercial software packages, such as CST MWS [2], Ansys HFSS [3] or EMSS FEKO [4].

All these methods share the common property of approximating field quantities by a finite set of basis functions [1, Ch. 3]. The basis functions can be an entire domain or, more commonly, subsectional, thus the structure is discretized into small elements (hexahedrons, tetrahedrons, triangles, rectangles etc.). It is desirable to approximate the the problem geometry and variations of the field within the elements as closely as possible.

Effective electromagnetic field simulation has been a relevant topic over the last few decades and the number of applications is constantly growing with the increasing popularity of wireless communications. Highly developed numerical methods, in conjunction with the capabilities of modern computers, have enabled engineers and scientists to simulate larger structures more than ever before. Moreover, it is possible to simulate full-wave behavior of not only separate parts of a wireless device, but of the system as a whole. On the other hand, for larger and more complex structures, cut and try methods, brute force optimization and design, based on an engineer's experience, becomes increasingly inefficient. For instance,

designing an antenna array without using the pattern multiplication principle would become quite complex. Thus, methods which can separate the independent effects of particular parts of a high-frequency device, or provide deeper understanding of physical principles are of great interest. One class of such methods are the modal methods which compute field solutions for a particular structure without an excitation. Consequently, they provide a different viewpoint on antenna operation and contribute to the understanding of physical principles.

There are several definitions of modes of a structure and corresponding numerical computation techniques. One is the well-known cavity model [5, Ch. 14] which can be numerically computed with the FEM in COMSOL Multiphysics [6]. The obvious disadvantages are the approximations made during the derivation of the method. Notably, no variations in the vertical component of the field are assumed and the cavity is closed to ideal (non-radiating) boundaries which means that inner couplings are neglected.

Another approach solves the homogeneous Helmoltz equation and finds the resonant frequencies of the structure and corresponding field distribution and can compute the unloaded quality factor [3]. This method is well-suited for cavity or dielectric resonators. However, there are several limitations concerning radiating problems including the difficulty of defining the radiating boundaries for eigenvalue problems. A similar approach in solving the Hemholtz equation is through discrete representation of the curl operator where the obtained matrix eigenvalue equation can be solved by Krylov-Subspace or the Jacobi-Davidson method [2]. It is well-suited for resonators despite the limitations for antenna problems described above.

Next modal method is the theory of characteristic modes (TCM) [7]. Since the theory was developed for radiation and scattering it bodes well for antenna analysis. The comparison between the cavity model and the TCM can be found in [8].

The bases of currently used numerical methods were established several decades ago and the formulations are extensively described in the literature, e.g. FDTD [9], FEM [10], MoM [11]. They are, however, attracting attention today due to their widespread usage by many companies. The research focuses mainly on reducing computation time, memory requirements, or increasing convergence and accuracy e.g. by using higher order basis functions (FEM, MoM [12]) or conformal techniques (FDTD).

Each of the methods has its strengths and weaknesses and is suitable for different types of problems, for an overview see e.g. [1]. Thus, another current research field is combining methods on parts of the computation domain to cover a wider variety of problem types. One such example is the domain decomposition method FE-BI which combines FEM with integral formulation [10].

Design procedures tailored for specific applications also exist. Antenna array synthesis procedures or the complete filter synthesis theory may serve as an example. These methods are not necessarily as flexible as the full wave methods, nonetheless, they provide design solutions which would otherwise be extremely difficult, or even impossible, with the general purpose techniques.

The theory of characteristic modes, which has a solid theoretical basis with few limitations sits amid these methods. However its results can be used for improved design procedures as demonstrated in [13, 14, 15, 16] and numerous other publications.

1.1 Review of the Literature

The concept of characteristic modes was developed by Garbacz and Turpin [17, 18, 19], who showed that it is possible to expand the fields radiated or scattered by a surface S, made from the perfect electric conductor (PEC), into a set of eigenfunctions (characteristic modes). The key properties of these modes are that they are real (equiphasal) on the surface, orthogonal with respect to the radiated power, and only a few modes are usually necessary to characterize the radiated or scattered fields with sufficient accuracy.

The theory was formulated from an alternative viewpoint by Harrington and Mautz [7], whose approach is to diagonalize the electric field integral equation (EFIE) operator. This formulation of the TCM provides explicit formulas for determining the characteristic functions (modes). A numerical computational method with a convergence study of the sum of the modal radiation patterns is also provided by the same authors in [20].

The TCM was also generalized to include dielectric and magnetic bodies [21], where the polarization and the magnetization current has to be considered in a volume of a material body. In the case of lossless materials the eigenvalues and modes are real and preserves orthogonality with respect to radiated power, as do the modes of perfectly conducting bodies. When the losses are present, the modes can be either defined as orthogonal with respect to radiated power, or as real [21]. The TCM for both dielectric and magnetic bodies was formulated using six-vector notation in [21]. An alternative approach to studying modes of dielectric and magnetic currents is through equivalent surface currents [22]. This approach is valid on condition that the materials are homogeneous. Characteristic modes for aperture problems were defined in [23].

The consequences of symmetry in the TCM were studied in terms of group theory in [24]. It was concluded that a symmetry causes degeneracy of the modes. If the proper MoM

expansion functions are selected the symmetry enables block diagonalization of the impedance matrix and, thus, a more efficient computation of the modes [24].

Increased interest in the practical application of TCM is observed in journal articles published in the last 10 years. The work [13, 25] showed advantages of modal approach in antenna design, particularly for circularly polarized antennas, multiple-input multiple-output (MIMO) antennas, electrically small antennas (ground plane radiation) as well as wire antennas and reflectarrays. Usage of characteristic modes as basis and testing functions in the MoM procedure was investigated in [25] and a poor convergence of the imaginary part of input impedance was reported. To solve this issue a so-called source mode was proposed to be added to the set of modes. The source mode can be obtained by subtracting the sum of the modes from the direct solution of EFIE. Since the modes change with frequency, they have to be recalculated at each frequency before they can be used as basis/testing functions. This issue was overcome by defining a set of frequency independent characteristic modes (computed by singular value decomposition). It is then assumed that the source mode is frequency independent and, thus, its recalculation at each frequency point is not necessary. Good convergence of the method was observed for the dipole and also for the rectangular patch antenna [25].

Application of the TCM on an ultra-wideband (UWB) antenna design was studied in [25] and based on the modal approach a two-feed rectangular UWB monopole with increased bandwidth was proposed, manufactured and measured. The results have inspired several other authors in their designs [25, p. 151]. The correspondence of the spherical modes and characteristic modes on a perfectly conducting sphere were studied in [26], then analytical formulas for a conducting cylinder were presented. It was noted that the close form expressions can be used as frequency dependent basis functions. The excitation of characteristic modes was studied from a practical point of view with the main goal being the combination of multiple feed locations to excite desired modes and suppress undesired ones. The multiple feed approach was found especially useful for circularly polarized antennas, where a combination of two orthogonal modes is necessary, and for MIMO antennas to achieve low correlation of received signals. Characteristic modes were fully utilized in the design of the UWB monopole antenna with notched band functionality [26, 27, 16]. The notched band was made tunable by varactor loading of the slot inside the monopole body and highly satisfactory agreement was observed between the full-wave simulation and measurement [16].

Typically, a small antenna is mounted on a metallic support structure, such as a PCB, thus the current is induced on the support structure as well. If the dimensions of the support

structure are bigger than the antenna body, the structure may become a more efficient radiator than the antenna itself. In the context of modal decomposition the small antenna can, therefore, be understood as an excitation or coupling element for the modes of the support structure. Possibilities of exciting PCB modes by an inverted-F antenna and coplanar metallic plate were studied in [26, Ch. 6] and the result was a folded antenna for mobile terminals with 69% fractional bandwidth (S_{11} lower than -6 dB).

The suitability of TCM for fractal antenna analysis and design was studied in [8]. The TCM was also compared with the cavity model (CM) and it was concluded that CM is quite efficient for computing a large number of modes despite its limited accuracy mostly due to approximations considered in the CM formulation. On top of that, TCM eigenvalues provide additional information regarding the physical behavior of the radiating surface, thus, TCM is the preferred modal method. It is interesting to note the relation of the MoM matrix inversion and its spectral representation [28].

The detailed procedure and recommendations on antenna design using modal information can be found in [8]. The L-probe feeding mechanism used for broad-banding a planar antenna, including the equivalent circuit model, is well described in [8]. Radiation efficiency was studied in terms of characteristic modes in [29, 30], however, since the skin effect was not included, the accuracy of the method was limited.

The ongoing question is the dominance of the modes which determine how modes contribute to the overall performance. Related to the issue of dominance is the question of how many modes are necessary to obtain the desired accuracy in a chosen parameter (e.g. input impedance or quality factor). Several modal significance measures were proposed to address the issues. First, the smaller the magnitude of the eigenvalue itself - which corresponds to the ratio of net reactive power to radiated power - the better a mode radiates energy [7].

The next proposed measure is the modal significance which represents normalized current amplitude [13, 14]. But neither modal significance nor the eigenvalue magnitude take into account the feeding position or the magnitude of the current which may vary greatly for different modes due to the normalization of the currents to unit radiated power. The significance measure proposed in [31] represents the case of each mode being excited in the region of its maximal amplitude.

The radiation quality factor, in terms of characteristic modes, was studied in [32] and more extensively in [33] and [34]. The latter work specializes in the coupled usage of characteristic modes and the theory of matching networks to improve antenna bandwidth. It starts with utilizing the modal radiation quality factor for estimating the bandwidth, then, the behavior

of input impedance and equivalent circuit representation are studied. The work concludes that characteristic modes are responsible for series resonance while a combination of two ChM is necessary to create a parallel resonance. This is in contrast to CM modes which are responsible for parallel resonances.

Theoretical part of [34] was followed by a design of a V-antenna for an unmanned aerial vehicle (UAV) with a maximum diameter of 1/17 of the wavelength in [34, Ch. 4]. In the following chapters, a systematic procedure of computing loads for input ports making a desired mode perfectly matched is developed. It was found, however, that for a fixed number of ports, a maximal frequency for which the procedure holds exists. At higher frequencies, the higher order modes are excited and distort perfect matching to the desired mode. It was also found that an ideal broadband matching network should have a negative slope of reactance against frequency. Consequently, non-Foster elements were investigated as the most appropriate loads [34].

Radiation and coupling modes (different from characteristic modes) were defined on sub-structures in [35]. The newly defined modes can be used to optimize coupling between several structures which influence each other. The method was demonstrated on coupled dipoles and a Yagi-Uda antenna with 3 and 6 elements. The drawback of the approach is the necessity of performing two decompositions and mapping the coupling and radiation modes to each other. A similar idea, with different goals and consequences, is to define sub-structure modes [36, 33] whose advantage lies in their ability to optimize a part of the antenna which can be accessed by an excitation. The latter reference also shows the interesting consequences of a single dominant mode, within a certain frequency range, which were successfully used for excitation-free antenna optimization.

After the modes are computed for a radiating structure, the excitation of desired modes have to be considered. For this purpose several feeding geometries were considered by different authors. First, the usual feeding mechanisms, such as coaxial feeding, proximity coupling and aperture coupling were considered [25]. To widen antenna bandwidth, an L-probe feeding mechanism, which can be regarded as a type of proximity coupled element, was investigated in [8]. Electrically small antennas, such as PIFA or small cubes mounted on a PCB, can be considered as feeding geometries [25, 26, 15]. Specialized feeding (or coupling) structures were developed to excite PCB modes [37] and utilized to design a MIMO antenna with reduced channel correlation [38].

Papers on numerical aspects of characteristic modes are more uncommon. Mode tracking algorithms connect the modes computed at different frequencies and are of high value for

broadband modal analysis. One proposed algorithm, which reduces a correlation matrix into a permutation matrix and is capable of wideband tracking of hundreds of eigenvalues, was presented in [39, 40]. It uses an adaptive tracking scheme, i.e. the modes are subsequently calculated in smaller frequency intervals until all relationships are resolved or the smallest frequency step is reached [40]. Another tracking algorithm has been developed in [41]. The advantage of this method is that it does consider that, the TCM decomposition may be ill conditioned and the impedance matrix may be numerically non-symmetrical, at certain frequencies.

The most recent papers are dedicated to the reconstruction of characteristic modes from a far-field pattern [42]. The key input of the method is the choice of the equivalent surface and it is not yet clear which geometry details can be omitted to obtain reliable results.

Another recent paper is focused on the creation of an equivalent circuit model from characteristic modes and eigenvalues [43]. An advantage of the model is that broadband behavior of input impedance as well as of antenna radiation can be extracted. Rather than a series RLC circuit, the paper uses a high pass circuit of different orders to model broadband behavior of eigenvalues. The theory was tested on a dipole and rectangular patch antenna. Behavior of the model for more complex geometries has yet to be analyzed.

There are also papers dedicated to the application of the TCM for antenna design. Specifically the MIMO antennas can be found in [27, 44, 45, 46, 47, 48, 38, 49] electrically small or multiband antennas using ground plane modes [15, 50] the usage of TCM for arrays and reflectarrays [51, 52, 53, 54] antenna integrated on a UAV [55, 56], multiband antennas [57] LTCC antenna [58], logarithmically periodical antenna [59], reconfigurable antennas [60, 61] and other [62, 63].

1.2 Thesis Goals

The general aim of the thesis is to contribute to the theoretical as well as practical knowledge of the theory of characteristic modes. The particular goals are specified as:

- To use the TCM for practical patch antenna design and study physical properties, especially resonant frequencies and the quality factor of patch antennas through modal decomposition (Chapter 3). Part of this goal is to pinpoint the limitations and fields of possible study for the rest of the thesis.

- To outline the possibilities of using characteristic modes for an active differentially fed antenna design (Chapter 4).

- To contribute to the development of an in-house modal analyzer. More specifically to develop a mesh generation tool which will enable further research of the numerical aspects of characteristic modes computation (Chapter 5).

- To study the effect of mesh density on modal results and to give recommendations for mesh refinement strategy (Chapter 5).

- To study the principle of exciting characteristic modes and to develop a method for determining an excitation coefficient for a scatterer coupled to a particular feeding geometry (Chapter 3 and 6).

1.3 Thesis Outline

The thesis is structured as follows: Chapter 2 aims to review the theoretical knowledge of the theory of characteristic modes. While similar theories have been developed for dielectric and magnetic bodies [21, 22] and apertures [23], the description will be restricted to the TCM for conducting bodies, utilized throughout this thesis. Characteristic currents and eigenvalues are considered as primary results, other (secondary) modal parameters such as characteristic angle, modal input admittance, modal radiation pattern and others can be computed from the primary results. An overview of the secondary modal parameters and their properties such as orthogonality and superposition will be also discussed in Chapter 2.

The first part of Chapter 3 is based on journal paper [64] which followed the author's master's thesis [65] and presents the design of a compact dual band antenna using TCM. The antenna has a self-affine U fractal motif and a dual L-probe feeding mechanism, which was developed to excite the desired modes in the two bands of interest. The second part of Chapter 3 is based on journal paper [66] and is dedicated to the analysis of modal resonant frequencies and the quality factor of chosen planar motifs. The paper utilizes expressions for radiation quality factor [67] and builds on the results published in [68]. Throughout the chapter, modal analysis tool, which uses the Rao-Wilton-Glisson (RWG) basis functions for expansion and testing is used [69, 70, 71] .

The work contained in Chapter 4 has been conducted in cooperation with the group of Prof. Daniel Segovia-Vargas of Carlos III University of Madrid and was presented in a conference contribution [72]. The ultimate goal of the research, which is utilizing the TCM for active antenna design, is still a topic for future work. Nonetheless, Chapter 4 presents a practical design of prototype of an active, differentially fed antenna. The design highlighted

the most critical aspects of active antenna design, some of which may be solved effectively by modal decomposition.

Chapter 5 introduces a tool for surface mesh generation in MATLAB called MeshGen. The motivation to implement a mesh generation algorithm was the lack of a serious TCM simulation tool which would enable scientists to create parametrized geometries, as well as to cope with our in-house modal analyzer [71]. The situation changed in September 2012, when FEKO released their modal analyzer [4]. Nevertheless, for research purposes it is invaluable to have the source code of a complete tool which can be modified to implement new ideas. The code structure and capabilities of the MeshGen tool are discussed at the beginning of Chapter 5.

As in other methods, mesh plays a crucial role in TCM since it influences both the speed of a simulation and its accuracy. These aspects were studied using MeshGen and the in-house tool and the results can be found in the second part of Chapter 5. The most important results are summarized in the paper [73] (in review process).

One of the important features of TCM is the possibility of summing the modes to obtain the total current as it would be computed by the direct solution of the electric field integral equation (EFIE). Summation formulas for various antenna parameters such as radiation pattern or input admittance are available when the excitation electric field is defined. The formulas are however valid only on condition that the structure does not change. Thus it is the purpose of Chapter 6 to review the mechanism of the excitation of characteristic modes and to propose a technique for determining excitation coefficients for particular feeding geometry, which will enable fast evaluation if the geometry is moved.

The conclusions and discussion of the achievements and future work possibilities are given in Chapter 7.

2

Theoretical Background

2.1 Theory of Characteristic Modes

Although the complete theory including the orthogonality relations and the superposition of the modal currents and fields is given in [7], this chapter is focused on the derivation and the important properties of modal solutions. It also aims to point out some steps which were not explicitly mentioned in the article and to link the derivations made by other authors with the theory basis.

First consider conducting body (or bodies) defined by surface S. If S is in the presence of an impressed electric field $\boldsymbol{E}^{\mathrm{i}}$ the electric current density $\boldsymbol{J}$ will satisfy the following operator equation for tangential components on S:

$$[\mathcal{Z}\boldsymbol{J} - \boldsymbol{E}^{\mathrm{i}}]_{\tan} = 0, \tag{2.1}$$

where the operator $\mathcal{Z}$ has the dimensions of impedance and is defined as [74, 7]:

$$\mathcal{Z}\boldsymbol{J} = \boldsymbol{E}(\boldsymbol{r}) = \mathrm{j}\omega\boldsymbol{A}(\boldsymbol{J}) + \nabla\phi(\boldsymbol{J}), \tag{2.2}$$

$$\boldsymbol{A}(\boldsymbol{J}) = \mu \oiint_S \boldsymbol{J}(\boldsymbol{r'})G(\boldsymbol{r},\boldsymbol{r'})\ \mathrm{d}s', \tag{2.3}$$

$$\phi(\boldsymbol{J}) = -\frac{1}{\mathrm{j}\omega\varepsilon} \oiint_S \nabla' \cdot \boldsymbol{J}(\boldsymbol{r'})G(\boldsymbol{r},\boldsymbol{r'})\ \mathrm{d}s', \tag{2.4}$$

$$G(\boldsymbol{r},\boldsymbol{r'}) = \frac{e^{-\mathrm{j}k|\boldsymbol{r}-\boldsymbol{r'}|}}{4\pi|\boldsymbol{r}-\boldsymbol{r'}|}. \tag{2.5}$$

Vector $\boldsymbol{A}$ is the magnetic vector potential, ϕ is the electric scalar potential, μ is the permeability of the surrounding medium and ε is the permittivity of the surrounding medium. Next define the *symmetric product* (or a *reaction*) [74]

$$\langle \boldsymbol{X}, \boldsymbol{Y} \rangle_s = \oiint_S \boldsymbol{X} \cdot \boldsymbol{Y}\ \mathrm{d}s. \tag{2.6}$$

Note that symmetric product is not the inner product, however the *inner product* for the complex Hilbert space can be written as $\langle \boldsymbol{X}^{\boldsymbol{*}}, \boldsymbol{Y} \rangle_s$, where asterisk denotes a complex conjugate. It follows from the reciprocity theorem [74] that $\mathcal{Z}$ is symmetrical, but not Hermitian i.e.

$$\langle \boldsymbol{X}, \mathcal{Z}\boldsymbol{Y} \rangle_s = \langle \mathcal{Z}\boldsymbol{X}, \boldsymbol{Y} \rangle_s, \tag{2.7}$$

$$\langle \boldsymbol{X}^{\boldsymbol{*}}, \mathcal{Z}\boldsymbol{Y} \rangle_s \neq \langle \mathcal{Z}^{*}\boldsymbol{X}^{\boldsymbol{*}}, \boldsymbol{Y} \rangle_s. \tag{2.8}$$

The Hermitian parts of $\mathcal{Z}$ are

$$\begin{aligned} \mathcal{R} &= \frac{1}{2}(\mathcal{Z} + \mathcal{Z}^{*}), \\ \mathcal{X} &= \frac{1}{2\mathrm{j}}(\mathcal{Z} - \mathcal{Z}^{*}), \end{aligned} \tag{2.9}$$

thus

$$\mathcal{Z} = \mathcal{R} + \mathrm{j}\mathcal{X}. \tag{2.10}$$

Next formulate a *complex power balance*[1] for an infinite sphere S_∞ enclosing S [74, 7].

$$P_\mathrm{i} = P_\mathrm{f} + \mathrm{j}\omega(W_\mathrm{m} - W_\mathrm{e}), \tag{2.11}$$

where the powers and energies are defined as follows. The *power imposed by current sources*,

$$P_\mathrm{i} = \langle \boldsymbol{J}^{*}, \mathcal{Z}\boldsymbol{J} \rangle_s = \langle \boldsymbol{J}^{*}, \mathcal{R}\boldsymbol{J} \rangle_s + \mathrm{j}\langle \boldsymbol{J}^{*}, \mathcal{X}\boldsymbol{J} \rangle_s. \tag{2.12}$$

The *power leaving the region* is

$$P_\mathrm{f} = \oiint_{S_\infty} \boldsymbol{E} \times \boldsymbol{H}^{\boldsymbol{*}} \, \mathrm{d}\boldsymbol{s}, \tag{2.13}$$

and the *time averaged electric and magnetic energies* are

$$W_\mathrm{e} = \frac{1}{2} \iiint_V \varepsilon |\boldsymbol{E}|^2 \, \mathrm{d}V, \tag{2.14}$$

$$W_\mathrm{m} = \frac{1}{2} \iiint_V \mu |\boldsymbol{H}|^2 \, \mathrm{d}V. \tag{2.15}$$

Note, that there is no dissipated power in (2.11) since we suppose the PEC surface in a lossless linear media. It can be concluded from the real and the imaginary part of (2.11) that $\langle \boldsymbol{J}^{*}, \mathcal{R}\boldsymbol{J} \rangle_s$ is equal to *radiated power* and $\langle \boldsymbol{J}^{*}, \mathcal{X}\boldsymbol{J} \rangle_s$ is equal to *reactive power*.

[1] Throughout this thesis, the time harmonic and complex quantities are related by $\boldsymbol{F}(\boldsymbol{r}, t) = \Im\{\boldsymbol{F}(\boldsymbol{r}) e^{\mathrm{j}\omega t}\}$ which explains factor $\mathrm{j}2\omega$ in the power balance in [74].

Let's consider diagonalizing the operator $\mathcal{Z}$ according to the generalized eigenvalue equation [74]

$$\mathcal{Z}\boldsymbol{J}_n = \nu_n \mathcal{M}\boldsymbol{J}_n, \tag{2.16}$$

where ν_n are the *eigenvalues*, $\boldsymbol{J}_n$ are the *eigenfunctions* (*modes*) and $\mathcal{M}$ is a weight operator to be chosen. For any symmetric weight operator all the eigenfunctions will satisfy orthogonality relation $\langle \boldsymbol{J^*}_n, \mathcal{M}\boldsymbol{J}_n \rangle_s = 0$ for $m \neq n$. For radiation and scattering problems it will be beneficial if the radiation patterns are orthogonal i.e. $\mathcal{M} = \mathcal{R}$. Then (2.16) becomes

$$\mathcal{R}\boldsymbol{J}_n + \mathrm{j}\mathcal{X}\boldsymbol{J}_n = \nu_n \mathcal{R}\boldsymbol{J}_n. \tag{2.17}$$

Setting $\nu_n = 1 + \mathrm{j}\lambda_n$ the formulation of the TCM is obtained

$$\mathcal{X}\boldsymbol{J}_n = \lambda_n \mathcal{R}\boldsymbol{J}_n. \tag{2.18}$$

Since $\mathcal{R}$ and $\mathcal{X}$ are real and symmetric both the eigenvalues λ_n and modes $\boldsymbol{J}_n$ are real. The modes are usually normalized to a unit radiated power i.e. $\langle \boldsymbol{J}_n, \mathcal{R}\boldsymbol{J}_n \rangle_s = 1$. Obviously internally resonant modes (cavity modes) cannot be normalized in this way [74]. All normalized modes satisfy the following orthogonality relationships

$$\langle \boldsymbol{J}_m, \mathcal{R}\boldsymbol{J}_n \rangle_s = \delta_{mn}, \tag{2.19}$$

$$\langle \boldsymbol{J}_m, \mathcal{X}\boldsymbol{J}_n \rangle_s = \lambda_n \delta_{mn}, \tag{2.20}$$

$$\langle \boldsymbol{J}_m, \mathcal{Z}\boldsymbol{J}_n \rangle_s = (1 + \mathrm{j}\lambda_n)\delta_{mn}, \tag{2.21}$$

where $\delta_{mn} = 0$ for $m \neq n$ and $\delta_{mn} = 1$ for $m = n$ is the *Kronecker delta function*. Throughout the rest of the thesis, it is assumed that modes are normalized to the unit radiated power.

2.2 Interpretation of Modal Results

The *primary results* of eigendecomposition (2.18) are the characteristic numbers λ_n and corresponding modes $\boldsymbol{J}_n$. From these primary results other quantities such as the modal electric and magnetic field, modal radiation pattern, modal admitance and others can be computed. These properties will be referred as the *secondary results*. The overview and interpretation of these results will be given in this section.

Taking the symmetric product of both sides of (2.18) we can interpret the characteristic number as a ratio of modal reactive power to modal radiated power. Considering the normalization of characteristic currents we obtain [7, 75]

$$\lambda_n = \frac{\langle \boldsymbol{J}_n, \mathcal{X}\boldsymbol{J}_n \rangle_s}{\langle \boldsymbol{J}_n, \mathcal{R}\boldsymbol{J}_n \rangle_s} = \omega(W_{\mathrm{m},n} - W_{\mathrm{e},n}). \tag{2.22}$$

Variational interpretation of the TCM considers minimizing the functional (2.22) by $\boldsymbol{J}_n$ [8, Ch. 4.6], [75].

The *Characteristic angle* is defined[2] as [76]

$$\alpha_n = \pi - \arctan(\lambda_n). \tag{2.23}$$

As mentioned in [13], α_n represents a phase of the characteristic current. To be more specific, consider a port located at arbitrary point on the antenna with excitation voltage $U_{\mathrm{in}} = 1$ V. Then the input power delivered to the mode will be $P_{\mathrm{in},n} = U_{\mathrm{in}} I^*_{\mathrm{in},n}$ and using the power balance (2.11) and (2.22) we can write

$$\lambda_n = -\frac{\Im\{I_{\mathrm{in},n}\}}{\Re\{I_{\mathrm{in},n}\}}. \tag{2.24}$$

Form (2.24) and (2.23) the input current due to mode $\boldsymbol{J}_n$ is

$$I_{\mathrm{in},n} = |I_{\mathrm{in},n}|\, e^{\mathrm{j}(\alpha_n - \pi)}. \tag{2.25}$$

Because the characteristic modes are equiphase, $\alpha_n - \pi$ represents also a phase of the mode excited by a voltage with zero phaseshift. At *resonant frequency* f_0, characteristic number satisfies the condition $\lambda_n(f_0) = 0$ i.e. the characteristic angle $\alpha_n(f_0) = \pi$, as follows from (2.22). Modal bandwidth can be defined by frequencies where characteristic number or angle reaches a threshold value. For instance, relative half power radiating bandwidth is defined in [25] as a difference of frequencies, at which α_n reaches 135° and 225°, divided by the resonant frequency.

The concept of radiation quality factor has long been studied in the literature, yet there remain unsolved questions, e.g. its exact relation to impedance bandwidth. Several different definitions can be found in literature

$$Q = \frac{\omega(W_{\mathrm{m}} + W_{\mathrm{e}})}{P_{\mathrm{r}}} \qquad \text{conventional definition from fields} \tag{2.26}$$

$$Q_Z = \frac{\omega}{2R_{\mathrm{in}}}\left|\frac{\partial Z_{\mathrm{in}}}{\partial \omega}\right| \qquad \text{impedance definition [77]}, \tag{2.27}$$

$$Q_J = \frac{\omega(W_{\mathrm{m}}(\boldsymbol{J}) + W_{\mathrm{e}}(\boldsymbol{J}))}{P_{\mathrm{r}}(\boldsymbol{J})} \qquad \text{current density definition [67]}. \tag{2.28}$$

[2] Characteristic angle is often plotted in degrees. Note that an idea of inspecting the angle of the eigennumber was allready mentioned in [19].

While the conventional definition is the most widely accepted, for time-harmonic fields the electric and magnetic energy in the whole space are infinite, but the infinities may be subtracted leaving a finite Q value [67]. The impedance formula Q_Z had been defined as an estimation of Q [77] and it can be prooven that $Q_Z = Q_{\mathrm{C}}$ for series and parallel RLC circuit [67]. Interestingly, the impedance quality factor can be computed also from source current density and used without knowledge of feed location or impedance [78]. It is possible to compute Q_J from currents flowing in a finite volume, for more details see [67].

Probably the most useful application of quality factor is the determination of physical limitations of electrically small antennas and the connection to the impedance bandwidth [77]. The latter purpose will be considered in this thesis. The *modal radiation quality factor* $Q_{\mathrm{eig},n}$ was derived in [79] by taking a frequency derivative of matrix Rayleigh quotient formula for λ_n on condition that the dominant frequency change is due to matrix representation of operator $\mathcal{X}$.

$$Q_{\mathrm{eig},n} = \frac{\omega}{2}\left|\frac{\partial \lambda_n}{\partial \omega}\right|. \tag{2.29}$$

The same formula was derived in [32] from Q_Z on condition that $\partial \boldsymbol{J}_n/\partial\omega$ is small compared to $\partial\lambda_n/\partial\omega$. Note that despite the fact that (2.29) was derived for a particular port location, the resulting equation is independant on port location which is in accordance with the modal approach. Considering, that the variation of the current with frequency is negligible,

$$Q_{\mathrm{eig},n} = Q_{X,n} = \frac{\omega}{2}\frac{\partial X_{\mathrm{in},n}}{\partial \omega}, \tag{2.30}$$

where $X_{\mathrm{in},n}$ is the input reactance corresponding to mode n.

The electric field $\boldsymbol{E}$ due to current density is computed by (2.2) and in the far field region, the expression reduces to [80, Ch 14]

$$\boldsymbol{E}_{\mathrm{FF}}(\boldsymbol{r}) \approx -\mathrm{j}\omega\mu\frac{e^{-\mathrm{j}kr}}{4\pi r}[\hat{\boldsymbol{\theta}}F_\theta(\boldsymbol{r}) + \hat{\boldsymbol{\phi}}F_\phi(\boldsymbol{r})], \tag{2.31}$$

where $\hat{\boldsymbol{\theta}}$ and $\hat{\boldsymbol{\phi}}$ are the unit vectors in spherical coordinates directions, r is the distance between the origin and the observation point and the *radiation pattern* $\boldsymbol{F} = \hat{\boldsymbol{\theta}}F_\theta(\boldsymbol{r}) + \hat{\boldsymbol{\phi}}F_\phi(\boldsymbol{r})$ is related to current density as

$$\boldsymbol{F}(\hat{\boldsymbol{r}}) = \iiint_V \boldsymbol{J}(\boldsymbol{r}')e^{\mathrm{j}k\hat{\boldsymbol{r}}\cdot\boldsymbol{r}'}\ \mathrm{d}^3r'. \tag{2.32}$$

Note that $\boldsymbol{F}$ is considered in the far-fiel region[3] and thus it can be rewritten in terms of spherical coordinates as $\boldsymbol{F}(\theta,\phi)$.

[3] Ideally the distance from source $|\boldsymbol{r}-\boldsymbol{r}'| \to \infty$.

The *radiation intensity* is computed as $U(\theta,\phi) = k\omega\mu(|F_\theta|^2 + |F_\phi|^2)/(32\pi^2)$ and the radiated power [80, Ch 15]

$$P_\mathrm{r} = \int_0^\pi \int_0^{2\pi} U(\theta,\phi)\sin(\theta)\ \mathrm{d}\theta\ \mathrm{d}\phi \tag{2.33}$$

To compute a *modal radiation pattern* $\boldsymbol{F}_n$ one can simply replace $\boldsymbol{J}$ with $\boldsymbol{J}_n$ in (2.32).

2.3 Orthogonality and Modal Superposition

It has been shown, that characteristic modes form a complete orthogonal set in the Hilbert space [18], thus any current on surface S can be expressed as an infinite sum of characteristic modes. Considering that an infinite sum produces a finite radiated power, some modes must radiate a negligible power and thus we may, in practice, consider a finite sum of N modes [19, 7]

$$\boldsymbol{J} \approx \sum_{n=1}^{N} a_n \boldsymbol{J}_n. \tag{2.34}$$

The *modal expansion coefficients* a_n can be computed by performing method of moments procedure [11, 81] with the modes as basis and testing functions. In other words, combining (2.1) with (2.34), then taking a symmetric product with $\boldsymbol{J}_m$ and considering the orthogonality (2.21) we arrive to

$$a_n = \frac{\langle \boldsymbol{J}_n, \boldsymbol{E}^\mathrm{i} \rangle_s}{1 + \mathrm{j}\lambda_n}. \tag{2.35}$$

The term $\langle \boldsymbol{J}_n, \boldsymbol{E}^\mathrm{i} \rangle_s$ is called the *modal excitation coefficient* [7].

If the excitation is present, modal characteristics can be summed based on the current expansion (2.34) and (2.35). Since the modal decomposition is computationally demanding, the traditional solution of (2.1) using the method of moments is preferred from the numerical point of view. On the other hand, the knowledge how each mode contribute to the antenna characteristics (such as input impedance, radiation pattern etc.) is extremely valuable and can be used to improve traditional designs.

Any scalar linearly related to current is called a *linear measurement* ρ and is summed in a straightforward way [7].

$$\rho \approx \sum_{n=1}^{N} a_n \rho_n. \tag{2.36}$$

A linear measurement is for instance the input current at a port excited by voltage U_in produced by imposed electric field $\boldsymbol{E}^\mathrm{i}$. Knowledge of port current and voltage is sufficient to

compute input admitance:

$$Y_{\text{in}} = \frac{I_{\text{in}}}{U_{\text{in}}} \approx \frac{1}{U_{\text{in}}} \sum_{n}^{N} a_n I_{\text{in},n}, \tag{2.37}$$

where the modal contribution to the current through the port is $I_{\text{in},n} = \int_{\text{port}} \boldsymbol{J}_n \, \mathrm{d}\boldsymbol{s}$. We shall call the term $Y_{\text{in},n} = a_n I_{\text{in},n}/U_{\text{in}}$ the *modal admittance* [19, 82, 13, 43].

Considering, that each component of a vector linearly related to the current density is a linear measurement, we may express the electric field at every point in space $\boldsymbol{r}$ as

$$\boldsymbol{E}(\boldsymbol{r}) \approx \sum_{n=1}^{N} a_n \boldsymbol{E}_n(\boldsymbol{r}). \tag{2.38}$$

The magnetic field $\boldsymbol{H}(\boldsymbol{r})$ and the radiation pattern $\boldsymbol{F}$ defined by (2.32) can be summed equivalently to (2.38). Note that $\boldsymbol{E}_n$ and $\boldsymbol{H}_n$ are orthogonal both on the surface S and sphere at infinity S_∞ [7].

Summation of quantities, which are not linearly dependent on modes is also possible, but the derivation and interpretation is not as straightforward. The radiation quality factor of an antenna tuned to have zero reactance is such quantity. It can be expressed as a ratio of ω times the total stored energy to the radiated power, and in terms of modes, it is expressed as [68]

$$Q = 2\omega_0 \frac{\max\left\{ \sum_{m=1}^{M} \sum_{n=1}^{N} \beta_{m,n} W_{\text{e},m,n}, \sum_{m=1}^{M} \sum_{n=1}^{N} \beta_{m,n} W_{\text{m},m,n} \right\}}{\sum_{m=1}^{M} \sum_{n=1}^{N} \beta_{m,n} P_{\text{r},m,n}}, \tag{2.39}$$

where $W_{\text{e},m,n}$ and $W_{\text{m},m,n}$ are the modal electric and magnetic energies respectively and the *coupling matrix* $\boldsymbol{\beta} = [\beta_{m,n}]$ is defined as

$$\beta_{m,n} = \Re\left\{ a_m a_n^* \right\}. \tag{2.40}$$

Note that orthogonality of the reactive power (2.21) does not imply orthogonality of $W_{\text{e},m,n}$ and $W_{\text{m},m,n}$. More details and computation of these energies is described in [68].

If the formulation of the TCM assumes no losses, both the orthogonality of the radiation patterns (2.20) and real currents and eigenvalues will be obtained. If the losses in metalization were considered, the TCM could have been reformulated to make either radiation patterns or reactive power orthogonal, in a similar manner as described in [79, 21].

On the other hand, the losses in the metal can be approximated by the following procedure developed in [83] without the need of reformulating the TCM. We suppose that the current density on a common metal surface S of conductivity σ will be very similar to the

current density on the same surface S but made of the PEC. If the surface current density $\boldsymbol{J}$ is computed for a thin metal, the skin-effect is taken into account by introduction of an *equivalent volume current density* $\boldsymbol{J}_{\mathrm{eq}}$ such that

$$\boldsymbol{J}_{\mathrm{eq},}(z) = \boldsymbol{J}_{\mathrm{eq},}(0)e^{-(1+j)\gamma z}, \tag{2.41}$$

where it is assumed, that the metal is oriented in the coordinate system, such that $\boldsymbol{J}$ flows in the XY plane. The *attenuation constant* γ for a highly conductive material [74] reads

$$\gamma = \sqrt{\frac{\omega\mu\sigma}{2}}. \tag{2.42}$$

Then the equivalent volume current density is related to the surface current density of the perfect conductor

$$\left| \int_0^t \boldsymbol{J}_{\mathrm{eq}}(z)\ \mathrm{d}z \right| = |\boldsymbol{J}|\,, \tag{2.43}$$

where t is the thickness of the metalization. From the volume current density the loss power P_{L} is computed

$$P_{\mathrm{L}} = \int_{\Omega} \boldsymbol{E}\cdot\boldsymbol{J}^{*}_{\mathrm{eq}}\ \mathrm{d}V = F(\omega,\sigma,t)\int_{S}|\boldsymbol{J}|^2\ \mathrm{d}s, \tag{2.44}$$

where factor F is independent on S or surface current density:

$$F(\omega,\sigma,t) = \frac{\gamma}{\sigma}\frac{(1-e^{-2\gamma t})}{\left|1-e^{-(1+j)\gamma t}\right|^2}. \tag{2.45}$$

The assumptions made in the derivation were validated on the following antennas: coupled dipoles, an electrically small meandered dipole, and PIFA in a wide frequency range with a very satisfactory result [83].

Next lets define the *modal power loss* for thin metals[4]

$$P_{\mathrm{L},m,n} = F(\omega,\sigma,t)\int_{S}\boldsymbol{J}_m\cdot\boldsymbol{J}_n\ \mathrm{d}s. \tag{2.46}$$

Interpretation of the modal power loss is somehow difficult, since the modal currents are not orthogonal with respect to the losses and therefore there is a contribution to the total loss from all combinations of the considered modes. However, substituting (2.34) into (2.44), modal loss can be summed as

$$P_{\mathrm{L}} \approx F(\omega,\sigma,t)\sum_{m=1}^{N}\sum_{n=1}^{N} a_m a_n^{*} P_{\mathrm{L},m,n}. \tag{2.47}$$

[4]Note that characteristic modes are real vectors.

Using the orthogonal property of characteristic modes (2.20), the radiation efficiency is finally written as

$$\eta = \frac{1}{1+P_{\mathrm{L}}} = \frac{\sum\limits_{m}^{N} \beta_{m,m}}{\sum\limits_{m}^{N} \beta_{m,m} + \sum\limits_{m}^{N}\sum\limits_{n}^{N} \beta_{m,n} P_{\mathrm{L},m,n}}. \tag{2.48}$$

The *modal radiation efficiency* may be defined through a self-contribution of modal power loss as

$$\eta_n = \frac{1}{1+P_{\mathrm{L},n,n}}. \tag{2.49}$$

We would achieve $\eta = \eta_n$ if only the mode n was excited. But a nonzero contributions to the P_{L} from all modes implies that at the resonant frequency of mode n, the radiation efficiency will always be lower than η_n.

A finite sum of modes is considered in practice. For the purpose of determining which modes should be included in modal superposition, so called *modal significance measures* were defined. The simplest is the magnitude of an eigenvalue [79], which, according to (2.22), is equal to the reactive power of a normalized mode. Consequently the closer the eigenangle to 180° the smaller is the reactive power. However, λ_n appears also in the expansion coefficient (2.35) which directly enters the summation of modes. Thus *modal signifficance* MS_n was defined as [14, 13]

$$\mathrm{MS}_n = \left| \frac{1}{1+\mathrm{j}\lambda_n} \right|. \tag{2.50}$$

The major drawback of modal significance is that it does not account for an excitation and thus does not fully represent the significance of a mode in modal superposition. This issue have been pointed out in [31] and a new measure was defined

$$M_n = \frac{\max\limits_{\boldsymbol{r}} \{\boldsymbol{J}_n(\boldsymbol{r})\}}{\sqrt{1+\lambda_n^2}}. \tag{2.51}$$

The measure M_n would represent a magnitude of modal complex power if the mode was excited by $\boldsymbol{E}^{\mathrm{i}}$ at its maximum. Advantage of this measure is that it partially accounts for the excitation, and simultaneously no a priori knowledge of the port location is needed. A more precise measure, when actual feed position is known, is inspecting the contribution of each mode to the power budget [19, 31, 42]

$$P \approx \sum_{n=1}^{N} |a_n|^2 (1+\mathrm{j}\lambda_n). \tag{2.52}$$

3

Using the TCM for Antenna Analysis and Design

3.1 Design of a Dual-Band Orthogonally Polarized L-Probe-Fed Fractal Patch Antenna Using Modal Methods

A dual-band antenna was originally developed in [65] and further studies and improvements from the construction point of view were made. These improvements resulted in a very good agreement between the simulation and the measurement of both S-parameters and radiation pattern cuts. The motivation was to develop a dual-band antenna with compact dimensions and to widen its bandwidth as much as possible. The antenna uses the self-affine 'U' (SAU) fractal motif to ensure a dual-band performance and to lower the resonant frequency.

In order to analyze parametrized fractal shapes (including the effect of the iteration), the well-known cavity model (CM) [5] was used. Whereas the CM is faster than the TCM[1], it is restricted to low substrate heights h and low complexity of a motif shape (inner couplings are neglected by definition). Therefore, the CM results were refined by the TCM. The presented procedure follows the same steps as in [8] and shows its application on a dual-band antenna with a fractal motif.

The bandwidth potential is increased by feeding the antenna via an L-probe [84]. The probe was modified to match the antenna in both bands and to excite the corresponding modes. A negative effect is that the radiation pattern is slightly asymmetrical (5°-8° shift from the normal in main lobe direction).

[1] And produces a different set of modes than TCM, however the current distribution and the resonant frequency computed by CM are used as an estimate of the respective parameters computed by the TCM.

The antenna design procedure is described in the following sections 3.1.1 - 3.6, reprinted from author's article [64], © 2011 IEEE.

3.1.1 Analysis Procedure

At first, an analysis of a parametrized fractal motif was conducted using fast CM in order to find a suitable shape for dual mode (dual-band) operation with the desired ratio of resonant frequencies. The results were subsequently refined by the TCM, which is also suitable for arbitrary air substrate heights (an infinite ground plane is considered). The CM and the TCM routines were programmed in MATLAB [85, 86].

The modal results were validated by a full-wave simulation, where the current distribution on patch is a superposition of all modes i.e. theoretically an infinite series [28]. On the other hand, it is possible to obtain full-wave simulation results similar to the modal results if we choose feeding which predominantly excites the desired mode at its resonant frequency.

3.2 Fractal Motifs

3.2.1 Fractal Generation

A fractal is generated by the Iterated Function System (IFS) [87] implemented in MATLAB [86]. The IFS is defined by a finite family of contractions $S_1, S_2, ..., S_m$ where $m \geq 2$. For microstrip antennas (the 2 dimensional case), each transformation is described by coefficients a, b, c, d, e, f:

$$\begin{pmatrix} x_{i+1} \\ y_{i+1} \end{pmatrix} = \begin{pmatrix} a & b \\ c & d \end{pmatrix} \begin{pmatrix} x_i \\ y_i \end{pmatrix} + \begin{pmatrix} e \\ f \end{pmatrix}, \tag{3.1}$$

where x, y are Cartesian coordinates and i is an iteration order. The zeroth iteration (IT0) denotes the chosen initial shape, e.g. triangle, rectangle, circle etc. Each following iteration is a union of results of transformations $S_1, S_2, ..., S_m$ applied to the previous one. Rigorously, a fractal is generated after an infinite number of iterations. The nth iteration as an approximation of fractal will be used in the following text.

3.2.2 Chosen Fractal Motif

Based on previous experience, the fractal published in [88] was chosen as a potential candidate and will be called SAU (Self-affine 'U'). The original motif was parametrized according to Fig. 3.1. The overall dimensions of the fractal were restricted not to exceed 50 x 50 mm.

The SAU fractal is created from a rectangle by 4 parameter dependent IFS transformations according to Table 3.1, see Fig. 3.1.

Table 3.1: IFS transformations for a generalized SAU fractal, $b = c = 0$

T_n	a	d	e	f
T_1	$W1$	1-$L1$-$L2$	0	$L(L1+L2)$
T_2	1-$W1$-$W2$	1-$L1$-$L2$	$W(W1+W2)$	$L(L1+L2)$
T_3	$W1$	$L1+L2$	0	0
T_4	$W2$	$L2$	$W \cdot W1$	$L \cdot L1$
T_5	1-$W1$-$W2$	$L1+L2$	$W(W1+W2)$	0

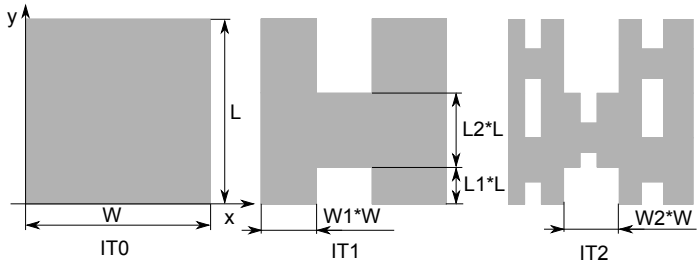

Figure 3.1: Iterations of the SAU motif ($W1 = 0.3, W2 = 0.3, L1 = 0.2, L2 = 0.4$).

3.3 Modal Results

Modal analysis revealed that modes 1 and 2 radiate in a normal direction if parameter L1 approaches 0 (the motif then resembles the letter 'U'). Calculated characteristic currents are shown in Fig. 3.2 and the corresponding modal radiation patterns in Fig. 3.3-3.4.

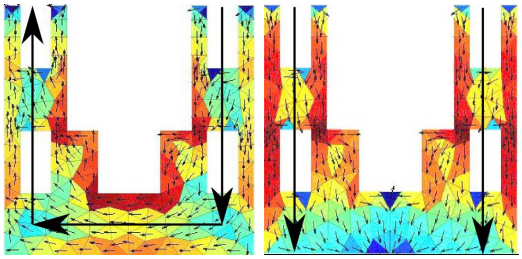

(a) Mode 1 (b) Mode 2

Figure 3.2: Surface current on the SAU IT2 motif with dimensions $W = L$=50mm, $W1 = 0.25, W2 = 0.5, L1 = 0, L2 = 0.5$ (TCM).

Radiation patterns were also calculated in CST MWS [89], where the patch was fed by a discrete port. Modal radiation patterns can quite accurately predict polarization and the direction of maximal radiation, Fig. 3.3-3.4. Orthogonality of polarizations could easily be

explained by inspecting the dominant current lines for modes 1 and 2 from Fig. 3.2.

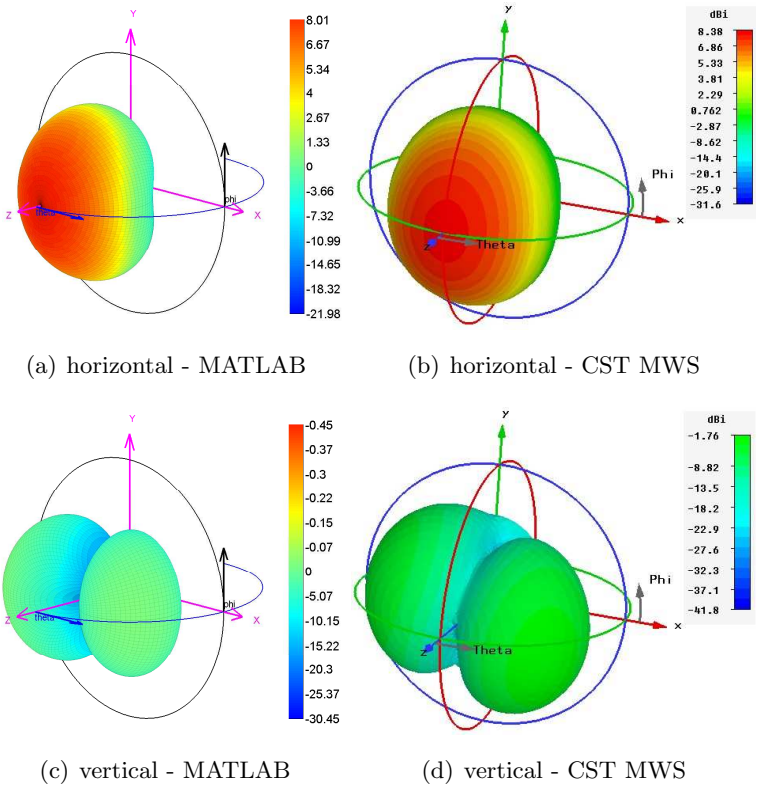

(a) horizontal - MATLAB (b) horizontal - CST MWS

(c) vertical - MATLAB (d) vertical - CST MWS

Figure 3.3: Mode 1 Ludwig3 components of radiation pattern for the motif from Fig. 3.2, 5mm air substrate and a discrete port used in CST MWS.

According to a parametric study of the SAU fractal, it is possible to achieve the modal ratio (CM) of f_2/f_1 to be approximately 1.6 - 3.5. The main influence on f_2/f_1 has the ratio W/L because the major part of the mode 1 current is orientated in the X axis direction and mode 2 forms a standing wave in the Y axis direction (Fig. 3.2).

It is known [90] that the higher the iteration the lower the resonant frequencies. A simple explanation is that higher iteration produces a more complex shape with a longer path for current. This effect is not linear with iteration and also affects different modes differently, Fig. 3.5.

The fractional antenna bandwidth FBW [77] is inversely proportional to the quality factor Q, which consists of contributions caused by different types of loss [5], [77]. The only reasonable option is the lowering of the radiation Q_{rad}, otherwise radiation efficiency $\eta = P_{rad}/P_{in}$ decreases. The Q_{rad} of microstrip antennas depends on current distribution and is inversely proportional to the substrate height h and directly proportional to substrate

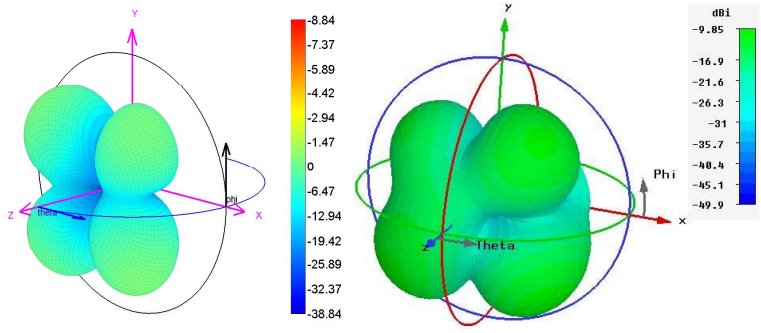

(a) horizontal - MATLAB (b) horizontal - CST MWS

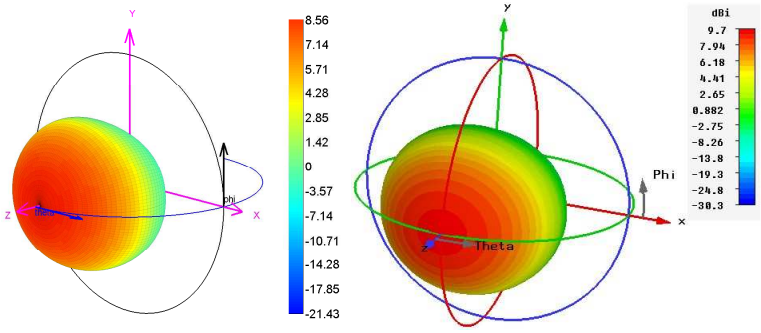

(c) vertical - MATLAB (d) vertical - CST MWS

Figure 3.4: Mode 2 Ludwig3 components of radiation pattern for the motif from Fig. 3.2, 5mm air substrate and a discrete port used in CST MWS.

relative permitivity ε_r [5]. The same effect of substrate height on modal $Q_{rad,n}$ could be seen in Fig. 3.6.

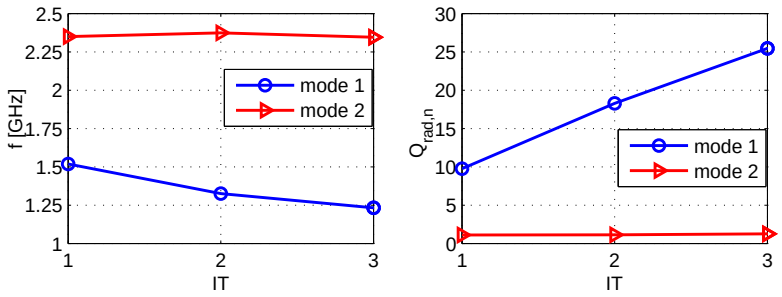

(a) Effect on resonant frequency (b) Effect on modal radiation quality factor

Figure 3.5: Effect of iteration, SAU motif, $W = L = 50$mm, $W1 = 0.25, W2 = 0.5, L1 = 0, L2 = 0.5$, h=30mm (TCM).

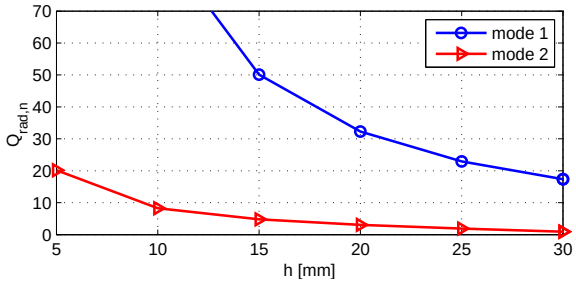

Figure 3.6: Effect of substrate height on modal quality factor of SAU IT2, $W = L = 50$mm, $W1 = 0.25, W2 = 0.5, L1 = 0, L2 = 0.5$ (TCM).

3.4 Full Wave Simulation

The SAU IT2 motif was chosen as a compromise between low resonant frequency and low modal quality factor, Fig. 3.5. Modes 1 and 2 satisfy the demand on low resonant frequency and normal radiation. Here we choose the patch with $W = L$ which corresponds to the modal $f_2/f_1 \approx 1.8$. However, the resonant frequency and the current density depend not only on patch shape, but also on substrate height h.

The selected motif is considerably electrically small (0.208 x 0.208 λ at f_1), therefore the FBW is quite narrow. To compensate this effect (Fig. 3.6) the patch is placed high enough above the ground plane and fed by an L-probe which acts also as a matching circuit. The optimal L-probe length and bend position is different in both bands [84], thus a modification leading to the dual L-probe (DL-probe) was proposed.

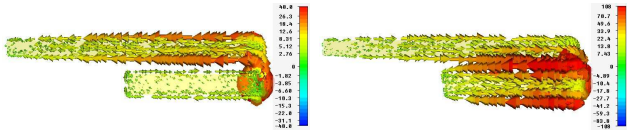

(a) $f = 1.25$ GHz (b) $f = 2.1$ GHz

Figure 3.7: Current density on the dual L-probe in both bands (CST MWS).

Fig. 3.7 shows that the current density in both bands is concentrated on specific and more or less independent parts (arms) of the DL-probe. This allows us to design the arms separately for each working band. An overall view of the CST model with the actual orientation of the DL-probe is shown in Fig. 3.8.

The proper feeding position can be guessed from the current density computed by the TCM (or CM). The horizontal part of the DL-probe arm should be orientated parallel to the modal current on the patch surface (see Fig. 3.2 and Fig. 3.8).

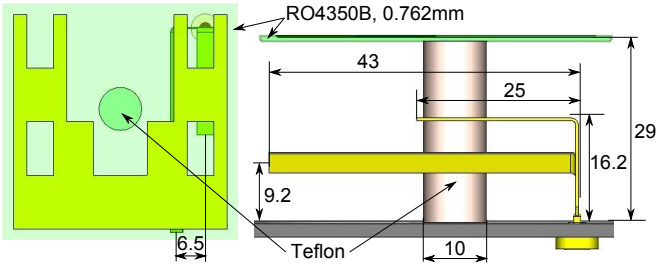

Figure 3.8: SAU IT2 CST model with dimensions in mm.

3.5 Measurement and Comparison of Results

An antenna with the SAU IT2 fractal motif was fabricated (see Fig. 3.9) and measured at the Department of Electromagnetic Field of FEE, CTU in Prague. The simulated and the measured S_{11} are in very good agreement, Fig. 3.10. In the lower band the motif dimensions are 0.208 x 0.208λ which leads to quite a narrow bandwidth. This disadvantage was partially compensated by using DL-probe feeding, which allows 10dB FBW to be 4.18%. The motif is electrically larger in the higher band (0.34 x 0.34λ), therefore the situation is easier and the measured FBW is 11.4%.

The antenna feeding is optimized to maximal bandwidth in the lower band. However, by changing dimmensions of the DL-probe an antenna with the FBW_{lower} = 3.42 % and the FBW_{upper} = 18.7 % was designed in the CST MWS.

Farfield cuts for horizontal an vertical polarization are in Fig. 3.11. Due to unbalanced feeding, the radiation pattern is distorted and the maximal directivity is slightly (5° and 8°) shifted from the normal direction (Fig. 3.11). Radiation pattern measurement confirms mutually orthogonal polarizations in both bands.

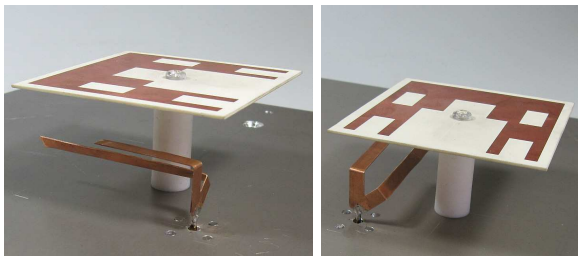

Figure 3.9: Manufactured antenna.

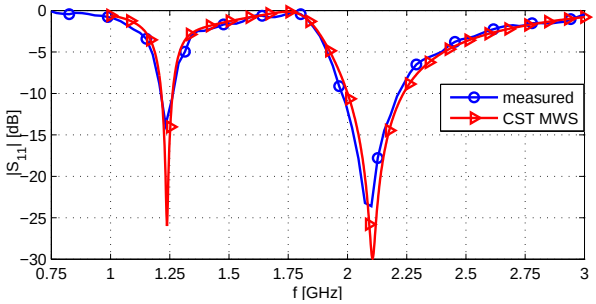

Figure 3.10: Comparison of simulated and measured S11 of SAU IT2.

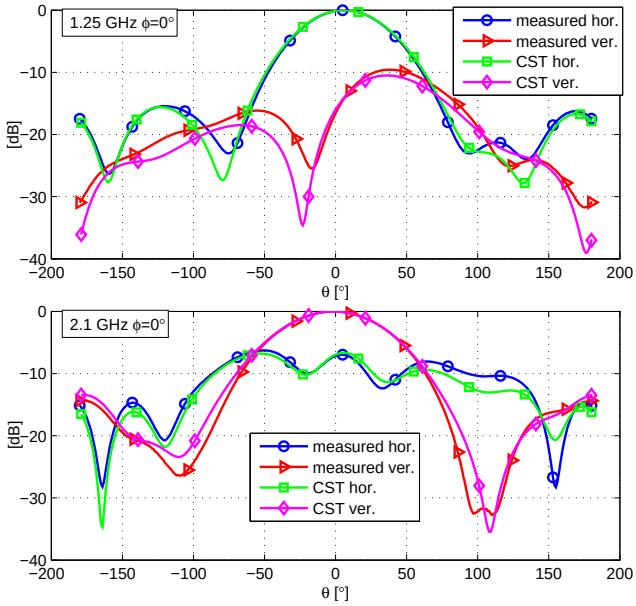

Figure 3.11: Measured and simulated farfield cuts for horizontal and vertical polarization.

3.6 Conclusion

This article summarizes the procedure of planar antenna design using modal methods. They provide information about motif behavior and its suitability for the desired antenna. Because only patch motif is considered, it is possible to effectively analyze even quite complicated shapes like fractals. More importantly, modal decomposition shed some light on the physical behavior of the planar antenna. The last step is a design of patch feeding and a full wave analysis.

Following the above mentioned procedure, a dual band antenna was developed, manufactured and measured. It was found that modal radiation patterns could successfully predict antenna radiation properties such as polarization or main lobe direction. Motif dimensions

are noticeably smaller than a $\lambda/2$ rectangular patch in both bands. The narrow bandwidth was partially compensated by the dual L-probe feeding structure. CST MWS simulation is in very good agreement with measurement.

The possible antenna applications are in point to point dual band systems which could operate with linear polarization. Suggested structure is, after some dimmension adjustments of the DL-probe and the motif, able to cover both WLAN bands 2.4GHz and 5GHz with $FBW_{lower} > 3.2$ % and $FBW_{upper} > 17$ %.

3.7 Radiation Quality Factor and Modal Resonant Frequency

Further studies of modal properties of chosen motifs over an infinite PEC plane were made. These studies utilizes a rigorous expressions for radiation Q_J derived in [67]. The chosen motifs were: a rectangle, a SAU fractal in the first and the second iteration and a fractal clover leaf (FCL) motif. Several important observations were made: the difference between the Q_J computed from modal currents and the Q_{eig} computed from the slope of the characteristic number is less than 1%, providing, that the triangles are small compared to the height over the finite ground. The increase in the error for small heights is probably caused by the centroid approximation in the Q_J calculation. Next it was confirmed on the SAU and FCL motifs that opposing currents increases the radiation quality factor. It was also observed that the resonant frequency of the dominant TM_{01} rectangular patch mode is quite complicated function of height for air substrates thicker than approx. 0.5λ. Finally it was observed that the resonant frequency of the low-Q modes is much more sensitive to the substrate height than of the high-Q modes. This can be explained by intensity of neaf-fields which are kept close to the radiating structure in case of the of high-Q modes.

The above stated results and computation procedure are described in the following sections 3.8 - 3.12, reprinted from author's article [66].

3.8 The Radiation Q Factor

In [67] a novel theory able to rigorously calculate radiated power and stored energies directly from currents flowing along the antenna has been presented. The radiation Q-factor is then readily evaluated by the definition [91]:

$$Q = 2\omega \frac{\max(\widetilde{W}_{\text{m}}, \widetilde{W}_{\text{e}})}{P_{\text{r}}}. \tag{3.2}$$

The equations for radiated power P_r and stored electric and magnetic energies are:

$$P_{\text{r}} = \left(\frac{1}{8\pi\omega\varepsilon_0}\right) \int_{\Omega 1} \int_{\Omega 2} [k^2 \boldsymbol{J}(\boldsymbol{r}_1) \cdot \boldsymbol{J}(\boldsymbol{r}_1) - \nabla \cdot \boldsymbol{J}(\boldsymbol{r}_1) \nabla \cdot \boldsymbol{J}(\boldsymbol{r}_2)] \frac{\sin(kr_{21})}{r_{21}} \, \text{d}\Omega 1 \, \text{d}\Omega 2, \tag{3.3}$$

$$\widetilde{W}_{\text{e}} = \frac{1}{16\pi\omega^2\varepsilon_0}(I_{\text{e}} - I_{\text{R}}), \tag{3.4}$$

$$\widetilde{W}_{\text{m}} = \frac{1}{16\pi\omega^2\varepsilon_0}(I_{\text{m}} - I_{\text{R}}), \tag{3.5}$$

where

$$I_{\mathrm{R}} = \frac{k}{2} \int_{\Omega 1} \int_{\Omega 2} \left[k^2 \boldsymbol{J}(\boldsymbol{r}_1)\boldsymbol{J}(\boldsymbol{r}_2) - \nabla \cdot \boldsymbol{J}(\boldsymbol{r}_1) \nabla \cdot \boldsymbol{J}(\boldsymbol{r}_2) \right] \sin(kr_{21}) \, \mathrm{d}\Omega 1 \, \mathrm{d}\Omega 2, \tag{3.6}$$

$$I_{\mathrm{e}} = \int_{\Omega 1} \int_{\Omega 2} \nabla \cdot \boldsymbol{J}(\boldsymbol{r}_1) \nabla \cdot \boldsymbol{J}(\boldsymbol{r}_2) \frac{\cos(kr_{21})}{r_{21}} \, \mathrm{d}\Omega 1 \, \mathrm{d}\Omega 2, \tag{3.7}$$

$$I_{\mathrm{m}} = k^2 \int_{\Omega 1} \int_{\Omega 2} \boldsymbol{J}(\boldsymbol{r}_1) \cdot \boldsymbol{J}(\boldsymbol{r}_2) \frac{\cos(kr_{21})}{r_{21}} \, \mathrm{d}\Omega 1 \, \mathrm{d}\Omega 2, \tag{3.8}$$

where k is a free-space wavenumber, $\boldsymbol{J}$ is the surface current density and r_{21} is the distance between interacting current elements. The tilde denotes that the radiation contribution I_{R} has been subtracted from the stored energies at every point in space [92]. It is assumed that the currents are flowing in a vacuum.

3.8.1 The Modal Radiation Q Factor

The modal radiation Q factor may be evaluated from the slope of modal eigenvalues [79]:

$$Q_{\mathrm{eig}} = \frac{\omega_0}{2} \frac{\mathrm{d}\lambda}{\mathrm{d}\omega}. \tag{3.9}$$

In [79], (3.9) is supposed to be an approximation of the radiation Q, but in resonance it is actually exact. Since characteristic modes are normalized to radiate unit power $P_{\mathrm{r}} = 1$ [7], (3.2) reduces to:

$$Q = 2\omega \max(\widetilde{W}_{\mathrm{m}}, \widetilde{W}_{\mathrm{e}}). \tag{3.10}$$

For parallel or series RLC circuit (hence, for one mode), the "impedance Q_Z" equals the exact "current Q" [67]:

$$Q = Q_Z = \frac{\omega_0}{2} \left| \frac{\partial Z}{\partial \omega} \right| = \frac{\omega_0}{2} \left| \frac{\partial R}{\partial \omega} + \frac{\partial X}{\partial \omega} \right|. \tag{3.11}$$

Inserting

$$Z = R + \mathrm{j}X = \frac{1}{|I^2|} \left[P_{\mathrm{r}} + \mathrm{j}2\omega \left(\widetilde{W}_{\mathrm{m}} - \widetilde{W}_{\mathrm{e}} \right) \right], \tag{3.12}$$

valid for lossless antennas [74] and using the fact that $P_{\mathrm{r}} = 1$, (3.11) results in

$$Q = Q_X = \frac{\omega_0}{2} \left| \frac{\partial X}{\partial \omega} \right| = \frac{\omega_0}{2} \frac{\partial}{\partial \omega} \left[2\omega \left(\widetilde{W}_{\mathrm{m}} - \widetilde{W}_{\mathrm{e}} \right) \right] = \frac{\omega_0}{2} \frac{\partial \lambda}{\partial \omega} = Q_{\mathrm{eig}}, \tag{3.13}$$

providing that

$$\lambda = 2\omega \left(\widetilde{W}_{\mathrm{m}} - \widetilde{W}_{\mathrm{e}} \right). \tag{3.14}$$

It is therefore concluded that the modal Q_{eig} equals the Q_X by definition and it can be proven (using the reactance theorem [93, 94]) that in resonance it also equals the radiation Q defined from energies by (3.10).

3.8.2 Software Implementation

The above equations were implemented in MATLAB for the RWG triangular mesh where two different interaction situations occur:

(a) Distant Elements. When the triangular elements are not overlapping, current density on triangles may be simply approximated as point sources located at the centre of triangles [95], see Fig. 3.12. No actual integration is then needed. This centroid approach is very fast with satisfactory accuracy as will be shown later (however it may fail for patches located very close to the ground plane).

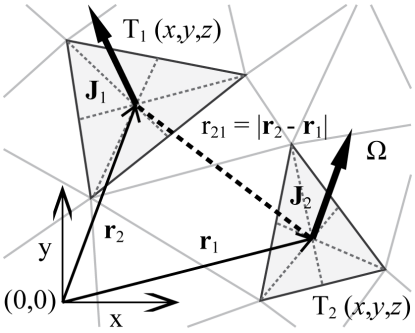

Figure 3.12: Distance between non-overlapping current elements [68].

(b) Overlapping (Self) Elements As known from the method of moments, the so-called "self" contributions are of great importance when dealing with calculations on discrete elements (meshes). Here, the self-interaction occurs when two triangles are overlapping each other. Due to the behavior of integral kernels, only rapidly varying term has to be carefully treated. Since $k_0 R_{21} \to 0$ (R_{21} being the longest side of the triangle T) is satisfied, one needs only to use the first term in the Taylor series expansion. The dominant singular static part is $1/r_{21}$ and the integral to be worked out is

$$I = \int_T \int_{T'} \frac{1}{\sqrt{(x-x')^2 + (y-y')^2}} \, \mathrm{d}x \, \mathrm{d}y \, \mathrm{d}x' \, \mathrm{d}y', \tag{3.15}$$

where $T = T'$ is a triangular area. Using simplex coordinates transformation (Fig. 3.13), the result is [68, 96]:

$$I = -\frac{4}{3} A^2 \left[\frac{\ln(1 - 2h_{12}/L)}{h_{12}} + \frac{\ln(1 - 2h_{13}/L)}{h_{13}} + \frac{\ln(1 - 2h_{23}/L)}{h_{23}} \right], \tag{3.16}$$

where A is the triangle area, h_{ij} are the edge lengths (see Fig. 3.13) and L is perimeter of the triangle.

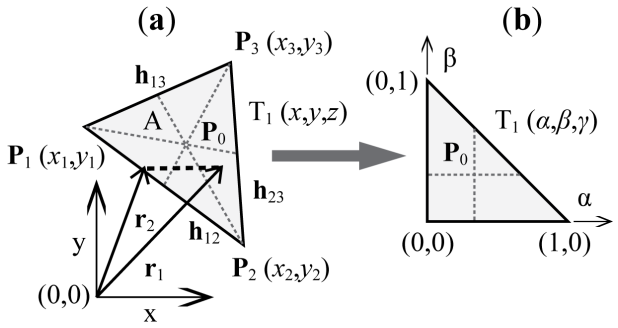

Figure 3.13: Self-term evaluation. a) original problem, b) simplex coordinates transformation, [68].

3.9 Applications: Rectangular Patch Antenna

Let us first concentrate on a rectangular patch antenna of dimensions $L = 50$ mm, $W = 30$ mm (further noted as R50x30) placed in air at a height H above an infinite ground plane. Only the dominant TM_{01} mode will be studied. The reason for choosing a patch with $L/W \neq 1$ is that we do not have to deal with degenerated modes. Using the image theory, the radiator in the XY plane at height $z = H$ above an infinite electric ground plane is modelled as two patches separated by $2H$. The total number of triangular elements is 676. In the TCM analyser, a proper out-of-phase mode is selected (Fig. 3.14).

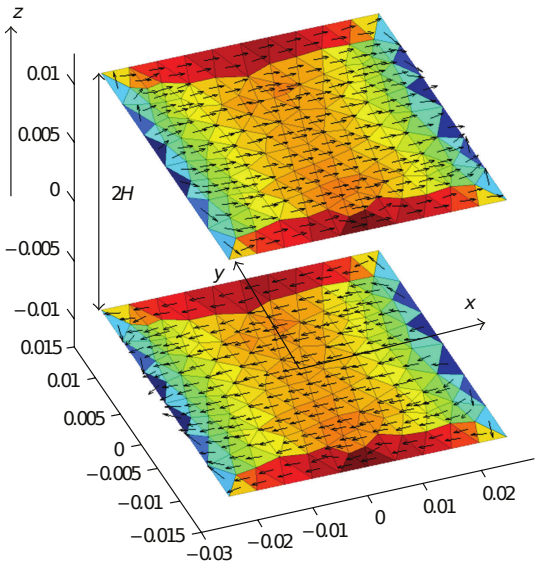

Figure 3.14: Model of MPA above infinite ground plane for $H = 10$ mm, dominant mode TM_{01} shown.

The resonant frequency of the dominant mode is shown as a function of height H, see Fig. 3.15. It has been evaluated from a modal resonant condition for eigenvalues as $2\omega\left(\widetilde{W}_{\mathrm{m}} - \widetilde{W}_{\mathrm{e}}\right) = 0$ employing an adaptive frequency sweep for each height. The behaviour is quite peculiar, especially for greater heights. For low heights ($H < 10$ mm or $H/\lambda_{\mathrm{res}} < 0.08$), the resonant frequency decreases "regularly" and quasi-analytical formulas (see e.g. [97, 98]) based on the fringing field concept are valid below this range. For $H \approx 25$ mm ($H/\lambda_{\mathrm{res}} \approx 0.188$) there is absolute minimum of the TM_{01} resonant frequency. Further on, the resonant frequency rises to reach its maximum for $H \approx 40$ mm ($H/\lambda_{\mathrm{res}} \approx 0.51$). Around this specific height the patch also shows the minimum of the radiation Q. The above described process repeats periodically. It is yet unclear to the authors as what is the physical background to the resonant frequency discontinuity around $H/\lambda_{\mathrm{res}} \approx 0.5$.

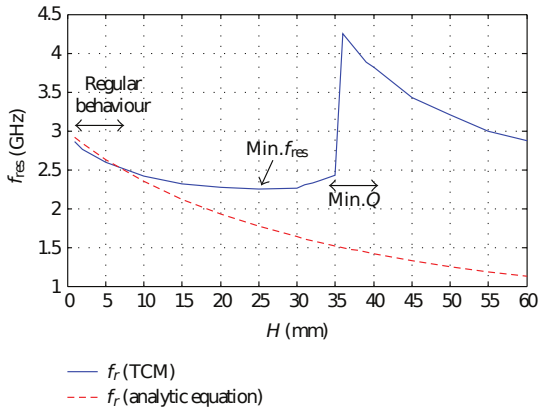

Figure 3.15: R50x30 resonant frequency of the dominant TM_{01} mode. The dashed red curve is a quasi-analytical equation from [97].

The terms $2\omega\widetilde{W}_{\mathrm{m}}$, $2\omega\widetilde{W}_{\mathrm{e}}$, and $2\omega(\widetilde{W}_{\mathrm{m}} - \widetilde{W}_{\mathrm{e}})$ obtained from (3.4) - (3.8) and eigenvalues λ are plotted at Fig. 3.16 for $H = 25$ mm as a function of frequency. There is excellent agreement between the difference in stored energies and the eigenvalues, both obtained in a completely different manner.

There is also very good agreement between the exact Q_J and Q_{eig} confirming the validity of the proposed algorithm via (3.13), see Fig. 3.17. Note that Q_{eig} in (3.9) does not require the currents to be calculated on the structure while Q_J is evaluated in a rigorous way from modal currents (3.10).

From Fig. 3.17 it is seen that the radiation Q has a minimum for a specific height. It is deduced that the reason lies in the cancelling of the radiated power between the two out-of-phase currents. Similar behaviour has been observed in the case of two half-wave thin-wire

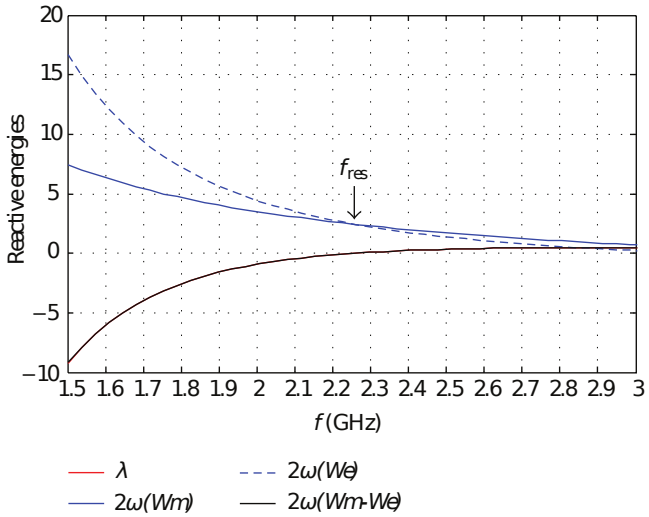

Figure 3.16: Reactive energies and their differences for an R50x30 patch at height of 25mm.

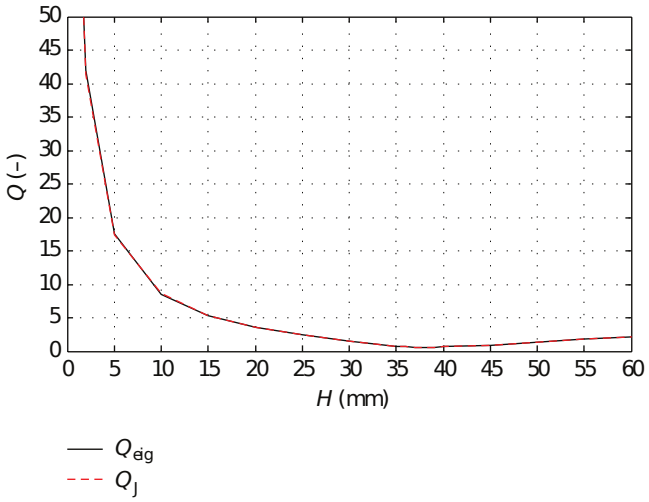

Figure 3.17: The radiation Q for dominant mode of an R50x30 patch as a function of H.

dipoles with opposite sinusoidal currents, separated by $d = 2H$, see [99] for details. Actually these two out-of-phase dipoles may serve as a very simple model for a patch antenna with a dominant mode. When the dipoles are reduced to elementary (Hertzian) ones, an approximate analytical solution is available and in [99] we shown that the Q is led by the function:

$$f_Q(H) \approx \frac{2H}{k2H - \sin k2H}. \tag{3.17}$$

After deriving (3.17), the condition worked-out

$$\tan(k2H) = k2H, \tag{3.18}$$

and the first non-trivial root of (3.18) could be approximated as [99]

$$\left(\frac{H}{\lambda}_{\min}\right) \approx \frac{3}{8} - \frac{1}{6\pi^2} = 0.358. \tag{3.19}$$

For sinusoidal currents on dipoles the minimum (evaluated numerically) occurs for $H = 0.36\lambda$. The minimum of the patch under study is obtained at $H \approx 0.4\lambda$, a value that is remarkably close to the simple dipole model.

3.9.1 Algorithm Convergence

Since no other methods for calculating modal Q are available, Q_{eig} is taken as a reference and the relative error percentage is defined as:

$$\text{relative error} = \frac{|Q_J - Q_{\text{eig}}|}{Q_{\text{eig}}} 100, \tag{3.20}$$

where Q_J is calculated from the currents using (3.10). Four different heights H were chosen, $H = 1$ mm (0.01λ), $H = 2$ mm (0.0185λ), $H = 10$ mm (0.0803λ) and $H = 20$ mm (0.151λ) and the relative error evaluated as a function of total triangular elements (including the mirror), see Fig. 3.18. All quality factors were evaluated at the resonant frequency of the dominant mode for the R50x30 patch. As discussed earlier, the centroid approximation became more inaccurate with low heights H. However, even for the lowest analyzed value $H = 0.01\lambda$, the relative error is in the order of a few percent for reasonable mesh density (hundreds of elements). Further improvements to the integration routine are considered for the future.

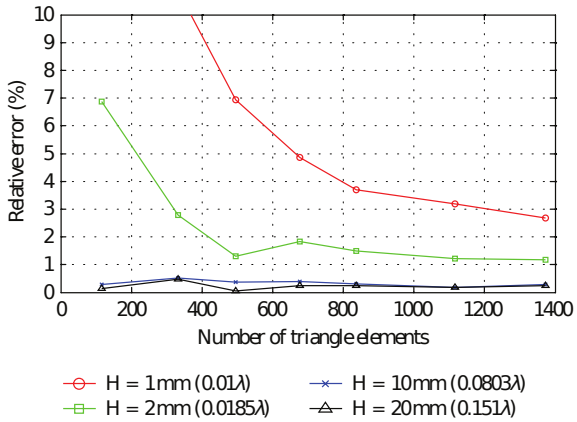

Figure 3.18: Relative error of the Q-factor as a function of triangular elements (mesh density).

3.9.2 Fractional Bandwidth of the R50x30 Patch Antenna

It is known that the fractional bandwidth (FBW) is related to the unloaded Q factor and the desired matching VSWR level. For VSWR$< s$ we have [77]

$$\text{FBW} \approx \frac{s-1}{Q\sqrt{s}}[\%] \tag{3.21}$$

Using a full-wave simulator CST-MWS [89], an R50x30 patch has been simulated and the FBW_{CST} for VSWR < 2 was calculated as:

$$\text{FBW}_{\text{CST}} = \frac{f_2 - f_1}{f_0}, \tag{3.22}$$

where f_2 and f_1 are margins for VSWR < 2 and f_0 is the centre frequency. Only very low heights were studied since we have used a simple probe feed which introduces an inductance component to the total input impedance. The comparison at Fig. 3.19 shows good agreement of both fractional bandwidths.

3.10 Applications: Fractal Antennas

In this section a bit more complex structures will be studied. The first one (The "Self Affine U" fractal, SAU, has been described in [88] and further analyzed in [64]. This kind of radiating motif is employed as a dual-band radiator with mutually orthogonal radiation patterns at both bands. Therefore we are analyzing the first two modes, where the currents are orthogonal. These are depicted at Fig. 3.20 and Fig. 3.21 for first (SAU1) and second

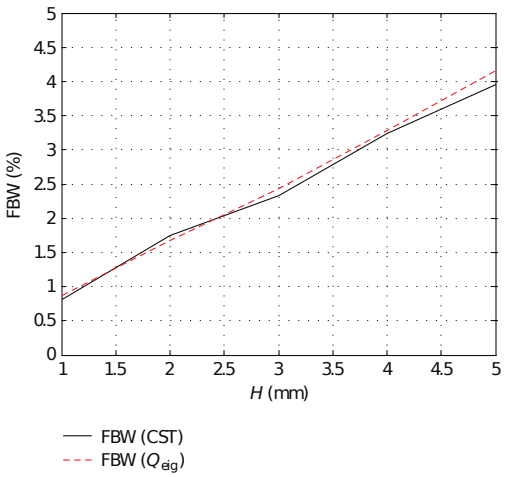

Figure 3.19: Fractional bandwidth FBW (VSWR < 2) for a R50x30 patch.

(SAU2) fractal iteration respectively. The current of the first (lower) mode $\boldsymbol{J}_1$ has two out-of-phase components (see Fig. 3.22 for schematic current paths) while the second mode comprises in-phase currents only. As we know from previous studies, opposite currents contribute to a rapid increase of the radiation Q and it is expected that $\boldsymbol{J}_1$ will have a much higher Q than $\boldsymbol{J}_2$.

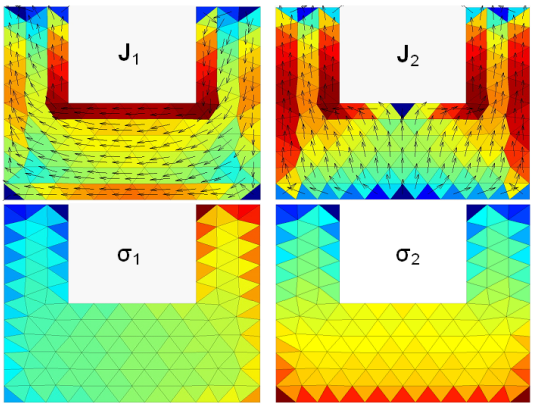

Figure 3.20: The first two characteristic modes (currents and charges) for the SAU1 structure.

Fig. 3.22 presents a very simple concept showing the main current paths for the $\boldsymbol{J}_1$ and $\boldsymbol{J}_2$ modes discussed above including the mirroring effect of the infinite ground plane. It could be simply stated that more opposing current paths lead to significant increase in Q.

We show detailed behaviour only for SAU2 (the situation is similar for SAU1) - see Fig. 3.23 that confirms high-Q for the $\boldsymbol{J}_1$ mode. Characteristic angles are calculated for

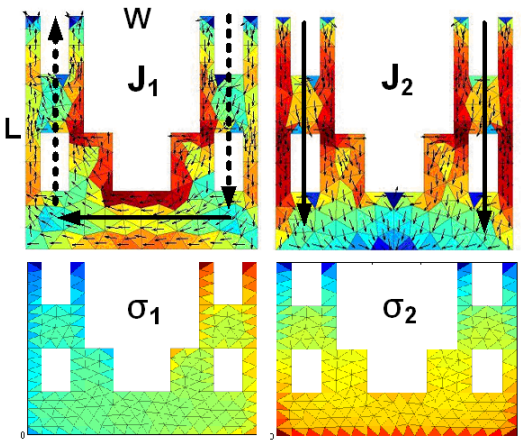

Figure 3.21: The first two characteristic modes (currents and charges) for the SAU2 structure.

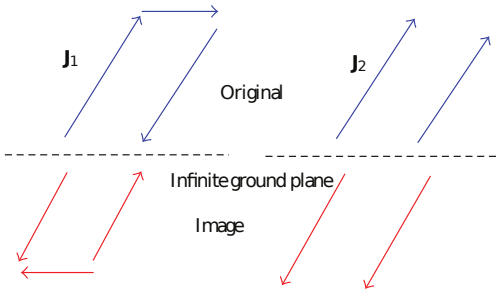

Figure 3.22: The main current paths for the first two modes of the SAU1/2 structure.

$H = 29$ mm, the actual height for which the dual-band antenna was designed [64].

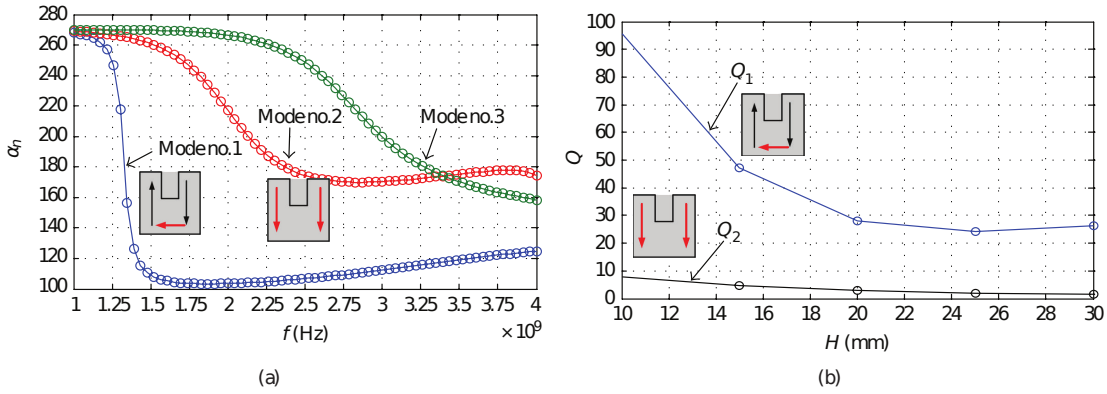

Figure 3.23: Characteristic angles (left) and radiation Q for the SAU2.

3.10.1 The FCL-2 Fractal Antenna

The second presented structure is the so-called Fractal Clover Leaf (FCL) of the second iteration, [86]. The antenna is fed by an L-probe [100] that excites its dominant mode and is located at height $H = 36$ mm. Actually, the dominant mode is composed of two degenerated modes $\boldsymbol{J}_1$ and $\boldsymbol{J}_2$ (Fig. 3.24). The second higher mode $\boldsymbol{J}_3$ is shown at Fig. 3.25 for completeness. Fig. 3.26 shows the main current paths of these modes and we can again deduce that the dominant mode will exhibit lower Q compared to $\boldsymbol{J}_3$. This is confirmed by Fig. 3.27 - $\boldsymbol{J}_3$ has more than 200x higher radiation Q.

3.11 Resonant Properties of Studied Antennas

The properties of studied antennas are summarized in this section. At first we observed that microstrip antenna could support different kinds of modes regarding their Q factors (see Fig. 3.28):

a) Low-Q modes with the current flowing in one direction and not changing its phase (dominant modes of simple shapes like rectangular, circular patch etc..)

b) High-Q modes with part of the currents flowing in the opposite direction. These modes exist even on simple "U" shaped patch (Fig. 3.20 left) and on complex (fractal) geometries.

Secondly it has been observed that resonant frequency is quite a complicated function of height. Unfortunately we do not yet have any physical explanation as to why some modes present minimum values of f_r.

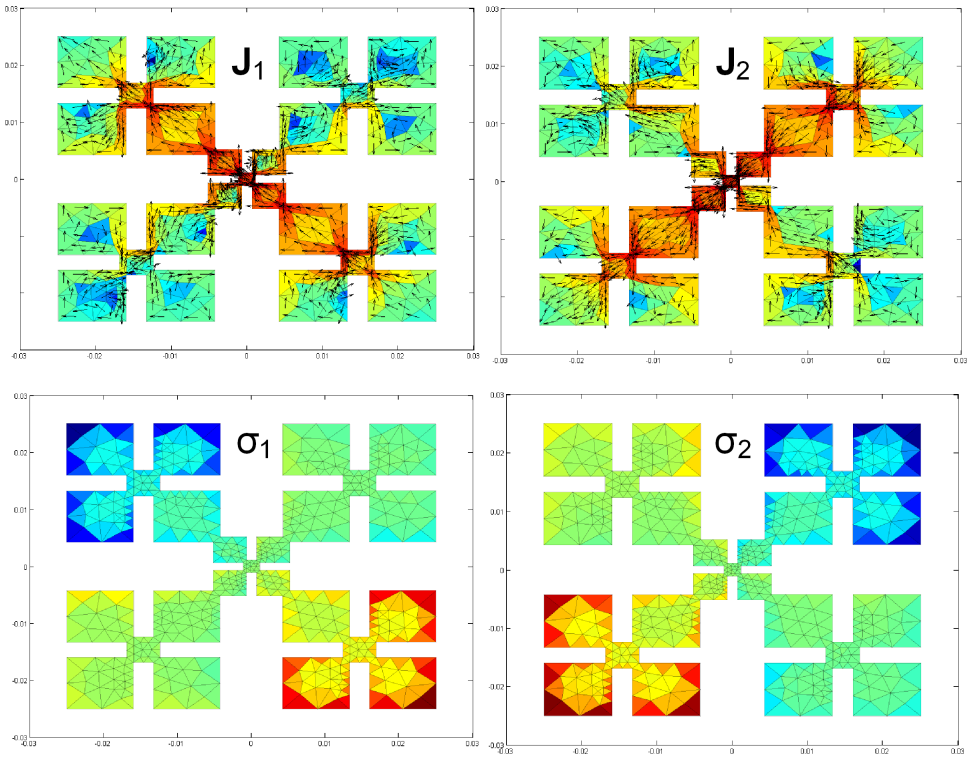

Figure 3.24: Degenerated dominant mode $\boldsymbol{J}_1$, $\boldsymbol{J}_2$ of the FCL2 antenna (currents and charges).

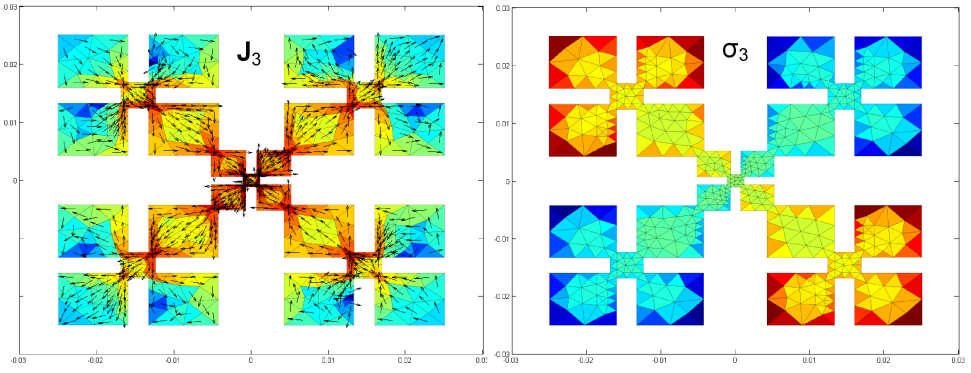

Figure 3.25: Second higher mode $\boldsymbol{J}_3$ (currents and charges).

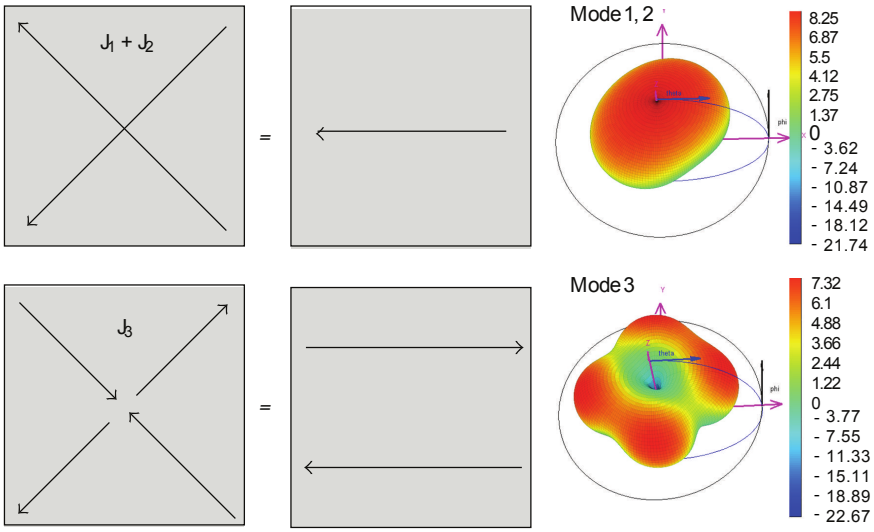

Figure 3.26: Schematic depiction of the dominant current paths for the dominant ($\boldsymbol{J}_1$+$\boldsymbol{J}_2$) and the second higher $\boldsymbol{J}_3$ modes together with their modal radiation patterns.

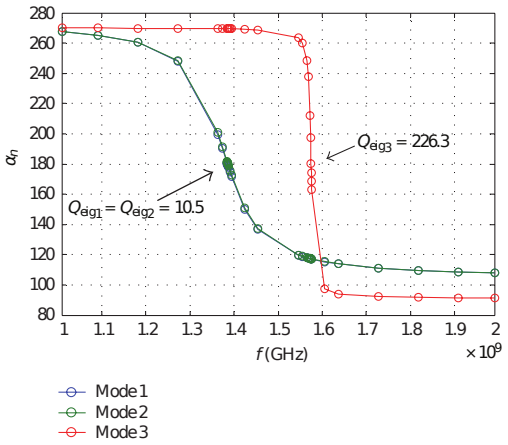

Figure 3.27: Characteristic angles for the FCL2 structure at $H = 29$ mm.

Looking at Fig. 3.29 it is clear (and interesting) that the resonant frequency behaves quite differently for low-Q and high-Q modes. The resonant frequency of low-Q modes is much more sensitive to the height, whereas high-Q modes exhibit almost constant fr when the height is varied. The proposed explanation is that the opposite currents (responsible for high Q) keep reactive fields very close to the radiating structure so the effect of a fringing field coupled to the ground plane becomes almost negligible.

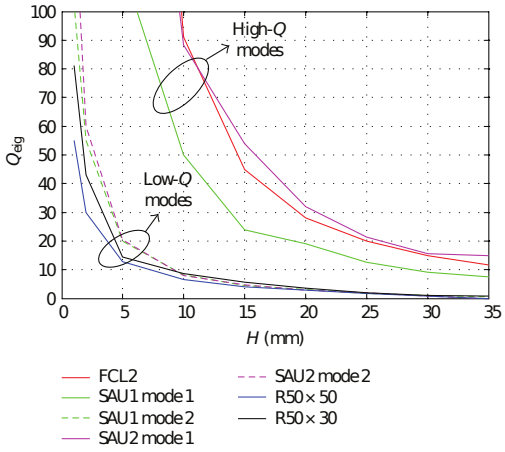

Figure 3.28: Radiation Qs for different antennas / modes.

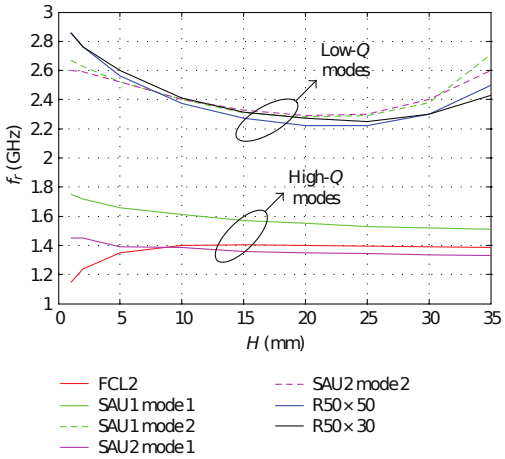

Figure 3.29: Resonant frequencies for different antennas / modes.

3.12 Conclusions

Modal resonant properties of selected microstrip patch antennas have been studied with the help of Characteristic modes and the novel theory published by G. Vandenbosch. It has been found that the resonant frequency of a simple rectangular patch antenna is quite a complicated function of its height above the infinite ground. Moreover, the dependency of resonant frequency is also found to be a function of the radiation Q-factor (which it is now possible to calculate in a rigorous way). Due to the complexity of the problem, no physical explanation for the resonant frequency behaviour has yet been found. It is observed that the radiation Q-factor decreases for "standard" heights ($<\sim 0.1\lambda$), however there exists an absolute minimum value of Q that has already been predicted by simple modeling of two elementary out-of-phase dipoles. Using proper feeding techniques (like with the L-probe) allows us to design wideband compact antennas. The theory now puts current distribution and the radiation Q factor into objective context. Whenever the current mode exhibits opposite components, high-Q may appear. Future work is needed to connect the presented theory with parameter sweeps or even optimization, so we will be able to design novel wideband / multimode compact antennas.

4

Active Differential Antennas

4.1 Introduction

A classical approach to the RF front end design of a wireless terminal is to create an antenna and match its impedance to a chosen line impedance Z_0 which could be the impedance of a connector e.g. SMA approximately 50 Ω. Then usually an amplifier or a low-noise amplifier (LNA), which is matched to the same reference impedance Z_0, is necessary. Since there is a common interface between the antenna and the LNA, their construction is independent and they can be designed by different persons or companies. The main drawback is that two matching circuits are necessary which can be a problem if there is a limited space for the RF circuit such as in mobile devices. Another drawback is that the matching circuit represents certain loss connected to the input of the LNA and thus it limits the minimal equivalent noise temperature of the device [101].

The differential circuits have been used for decades in analog circuits, however they were usually studied under the lumped element assumptions. In recent two decades the limits of differential circuits were pushed to the RF and microwave frequencies. Because of the increasing complexity and density of today integrated circuits the signal integrity becomes an issue [102]. The differential circuit can provide a low-cost solution in the noisy environment because of several reasons. Among other benefits, in an ideal differential circuit, no signal is propagating through the ground, thus the coupling to the neighboring lines is lowered. Also the crosstalk usually forms a common mode and can be suppressed by the differential circuit [102]. Drawbacks of the differential approach are increased power demands and an increased complexity of the circuit, resulting in longer design and verification times.

At RF and microwave frequencies a suitable tool for distributed element assumptions was necessary. This tool are the mixed-mode S-parameters [103]. They 'decompose' the n-port

circuit into $n/2$ mixed-mode ports which are excited by a mode specific waves; the common mode (CM) and the differential mode (DM). Note, that these modes refer to transmission

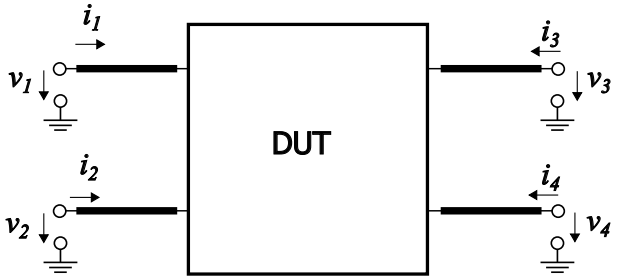

Figure 4.1: Mixed-mode S-parameter definition.

line waves, not the currents on the antenna, as is the case of characteristic modes.

The input mixed-mode port consists of single-ended ports 1 and 2, Fig. 4.1. Then the differential mode is defined for voltage $v_1 = -v_2$ and current $i_1 = -i_2$ and the differential voltage, current and impedance are:

$$v_\mathrm{d} = v_1 - v_2 \tag{4.1}$$

$$i_\mathrm{d} = \frac{1}{2}(i_1 - i_2) \tag{4.2}$$

$$Z_\mathrm{d} = \frac{v_\mathrm{d}}{i_\mathrm{d}}. \tag{4.3}$$

The common mode is defined for voltage $v_1 = v_2$ and current $i_1 = i_2$ and the common voltage, current and impedance are:

$$v_\mathrm{c} = \frac{1}{2}(v_1 + v_2) \tag{4.4}$$

$$i_\mathrm{c} = i_1 + i_2 \tag{4.5}$$

$$Z_\mathrm{c} = \frac{v_\mathrm{c}}{i_\mathrm{c}}. \tag{4.6}$$

From the above equations it can be concluded that for a line impedance Z_0 the common mode line impedance is $Z_{0\mathrm{c}} = Z_0/2$ and the differential line impedance is $Z_{0\mathrm{d}} = 2Z_0$. The mode specific S-parameters are defined in a similar manner as single-ended S-parameters i.e. as ratios of mode specific normalized waves. Detailed explanation including the transformation between the single-ended and differential S-parameters is available in [102].

The recent progress in active antennas exploits the differential feeding mechanisms, e.g. in [104] the patch antenna is fed by a push-pull power amplifiers avoiding an output balun. The topology can be regarded as a differential feeding of the antenna. Another interesting technique - aperture differential coupling - was published in [105]. It is a modification of

aperture coupling technique used for increasing the bandwidth of patch antennas [106]. The antenna is in a stacked configuration where a virtual short circuit in a microstrip line is located under the coupling aperture (slot) and on top of the aperture is the patch.

Since the differential active antennas achieves significantly lower noise temperature and high gain, they find applications especially in wireless communication systems or as array elements in direction detecting systems or radio detection experiments.

4.2 Advantages and Limitations of the TCM for Active Antenna Design

It has been shown, that the TCM can be used in conjunction with non-Foster elements to design electrically small antennas with increased bandwidth [34]. In the reference, it was realized, that the ideal load has necessary negative slope of reactance vs. frequency.

In this chapter, slightly different possibility will be investigated. The idea is to use characteristic modes to design a differentially fed active antenna. The impedance bandwidth will be inherently wider due to the usage of amplifiers while the farfield bandwidth is mainly determined by the passive part of the antenna. In fact, farfield properties of a single mode remain fairly constant over very wide BW. An example may be triangular patch with a slot in Fig. 5.17, in frequency range 4.5 - 6.5 GHz. The maximal directivity of the antenna fed by a discrete port varies from approximately 8 to 10 dBi, while the first and the second mode directivity is within 9.14 and 9.51 dBi. Therefore characteristic modes can be used to improve active antenna properties by widening the single mode operation bandwidth.

The sections 4.3 - 4.3 describe an active printed dipole antenna with a very low equivalent noise temperature and a natural suppression of common mode noise and are reprinted from author's conference contribution [72]. After completing the prototype, it was intended to use the TCM to modify the passive part of the active antenna. The goal was found to be problematic to achieve, since the input impedance of the passive part plays a crucial role in the design. It has to be optimized to ensure wideband stability of the amplifier for both the common and differential modes. Moreover, tuning the input impedance of the passive part can significantly improve its equivalent noise temperature and gain [102]. To be able to benefit from modal analysis, a method for effective recalculation of the input impedance for different position of antenna excitation is necessary. Therefore the work on the active differential antenna is has directed the following work to to the procedure presented in Chapter 6.

4.3 Printed Dipole Antenna

A printed dipole antenna will be used as a radiating element of the active antenna. The printed dipole is mainly chosen for demonstrating the active antenna benefits since the dipole is well-known with predictable behavior. Its input impedance at resonance is 88 Ω but it is not possible to achieve broadband impedance matching without additional matching circuit. The length of the dipole is 70 mm which corresponds to $0.5\lambda_0$ at the center frequency 2.15 GHz, the width is chosen 4 mm to lower the conduction losses and increase the bandwidth. The substrate is 0.508 mm RO4350B. While the antenna is fed through a coplanar strip line (CPS), the amplifier input is connected through 2 microstrip lines which could be considered as a coupled microstrip line (CML), see Fig. 4.2. Although the ground plane is present only under the CML it affects the dipole radiation pattern, which becomes more directive. It is known that the presence of a ground plane will reduce the radiation efficiency and radiation resistance. However the distance between the dipole and the ground plane is 30 mm which is significantly larger than the substrate height and the radiation efficiency is higher than 91% in the frequency range of interest. The dipole was designed in the CST MWS [89] using the waveguide port for feeding and electric symmetry plane. The symmetry plane ensures that only differential mode will be excited by the waveguide port. It is clear that the ground plane represents a discontinuity in the transmission line, Fig. 4.2. Thus a transition between CPS and CML will be considered next. Both lines can be described by two parameters: the gap width Wg and strip width Ws (the substrate height and metallization thickness is considered constant). These parameters are sufficient to describe both lines in terms of line impedance. The line impedance of a CPS is mainly defined by the width Wg between both stripes. On the other hand the differential impedance of the CML is mainly dependent on the impedance of the microstrip i.e. the width Ws. However the differential line impedance of the CML is not independent of Wg and the line impedance of the CPS is not independent of Ws. Nonetheless it is possible to design both transmission lines with the same dimensions and with only a small difference in the line impedance. Here it was chosen $Ws = 1.08$ mm and $Wg = 0.4$ mm which corresponds to 102 Ω for CPS and 75 Ω for CML. Another degree of freedom is the distance between the dipole and the ground plane. The segment of coplanar strip line is terminated by the dipole on one side and on the other side by the CML. This means it acts as a resonator and adjusting its length the S_{11} can be improved (according to the needs of the active part). The effect of the ground plane on the radiation pattern is clearly visible in Fig. 4.3. Further improvements in the input matching are also possible, however they will not lead to broadband matching in the frequency range from 1.7 - 2.6 GHz. The

input impedance of the active antenna will be dominantly defined by the amplifier output. On the other hand it is important to design the passive element to represent a suitable input load for the amplifier. Here we should consider the amplifier gain, noise figure as well as the broadband stability. The directivity of the dipole in the frequency range of interest is less dependent on frequency than the input impedance. This is useful for broad banding the antenna with an active part. In this case the maximum directivity varies from 7.15 dBi at 1.7 GHz to 4.58 dBi at 2.6 GHz (CST MWS).

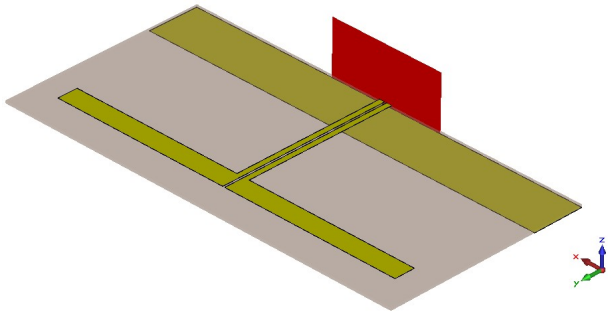

Figure 4.2: Printed dipole connected to CPS, CST MWS.

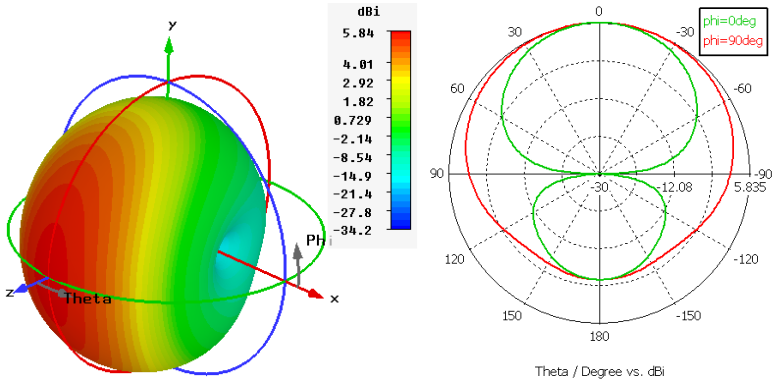

Figure 4.3: Radiation pattern of printed dipole connected to CPS at 2 GHz, CST MWS.

4.4 Differential Amplifier

The active part of the antenna is a single stage differential amplifier. The amplifier is studied in terms of the mixed-mode S-parameters. The goal of the design process is a low noise unconditionally stable amplifier with as high gain as possible. The amplifier will be directly connected to the printed dipole antenna. Since both the passive and the active parts have the differential topology there is no need for symmetrization or conversion to the single ended

mode. This is quite beneficial for low noise applications because symmetrization circuit represents a loss connected to the input of the amplifier. Due to the well-known Friis formula this loss has a very negative impact on the equivalent noise temperature Te of the whole system. Other benefit is reduction of circuit size. The dominant mode of a dipole is the differential mode. However the antenna will also receive a spurious common mode signal. Therefore it is necessary to ensure both the common and the differential mode amplifier stability. The stability criteria used is the geometrical stability factor μ [107]. The proposed amplifier has a fully differential topology which has certain advantages. They are a reduction of common mode noise and a high common mode rejection ratio (CMMR) [102]. This ratio describes how much of the common mode signal representing the interferences will appear at the output. The CMMR is defined as:

$$\mathrm{CMMR} = S_{21\mathrm{dd}} - S_{21\mathrm{cc}} \tag{4.7}$$

Where $S_{21\mathrm{dd}}$ is the differential to differential mode gain and $S_{21\mathrm{cc}}$ is the common to common mode gain in dB. Both the above mentioned properties are crucial especially in systems where a high coupling between RF and power lines can be expected. The amplifier was designed with AWR Microwave Office [108]. A circuit representation of the proposed amplifier is shown in Fig. 4.4. Both transistors used are the low noise HEMT ATF-34143 from Avago Technologies. The transistors are biased by Rg, Rd end Rs resistors. The DC voltage supply is separated from the RF part by capacitors Cin, Cout and Cd. Their values are chosen to be 33 pF which represents a good shortcircuit for the RF signal. The value of Cin is 10 pF to realize a better match between the dipole and the amplifier. Inductors Lg, Ls and Ld helps to stabilize the amplifier at high frequencies. They also affect the input and the output impedance. A particularly difficult part of the design is the broadband stabilization of the amplifier for both differential to differential mode (DD) and common to common mode (CC) operation. Here the R1, R2, L2 and C2 are used for that purpose. Their values were optimized to minimize the noise figure and maximize the gain. The ATF-34143 transistors were successfully used to design a two stage differential amplifier for lower frequency band (0.3-1 GHz) [109]. The two stage topology presented in [109] is more complicated and has higher power consumption (and higher gain) but it solves the problems with the stability. Component values for proposed single stage amplifier are listed in Table 4.1.

The final design was optimized using Simplex and Pointer AWR Microwave Office build-in optimizers. It was found that microstrip line TLd (Fig. 4.5) is beneficial for the stability. Therefore, the output L2, R2, C2 resonant circuit was omitted in the final design (Fig. 4.5).

Table 4.1: Component values for proposed amplifier

Component	Value
Cout,Cd	33 pF
Cin	10 pF
C2	0.5 pF
Lg	3 nH
Ld	47 nH
Ls	2.75 μH
L2	12 nH
Rg	270 Ω
Rd	47 Ω
Rs	3 Ω
R1	27 Ω
R2	330 Ω

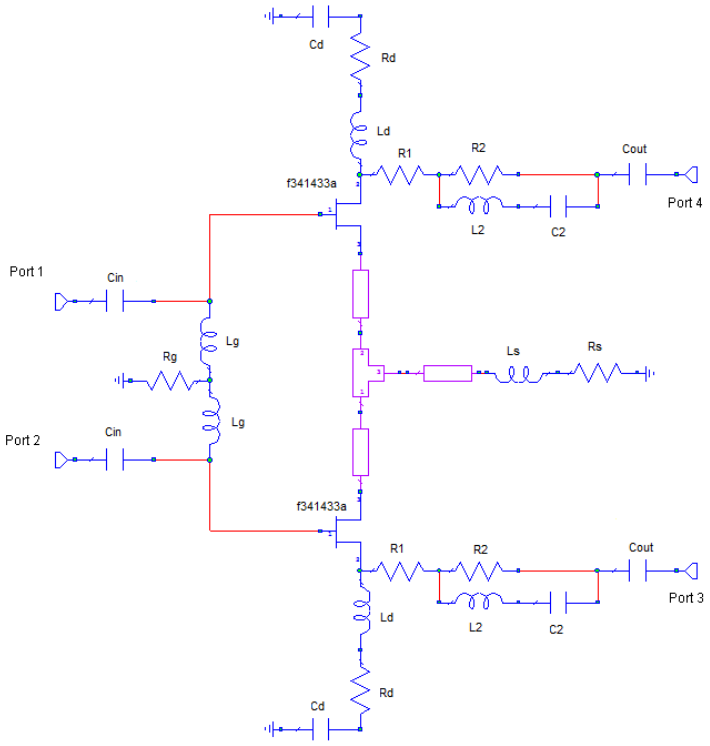

Figure 4.4: Circuit schematic of the proposed differential amplifier.

The distance between both transistors is critical both for the stability and differential gain and it should be as short as possible. The transistors are rotated 45 degrees for that reason.

The layout of proposed differential amplifier designed on RO4350B 0.508 mm substrate is in Fig. 4.5. The differential gain S_{21dd} is higher than 11.2 dB and the common mode gain is lower than -22.97 dB (from 1.7 to 2.6 GHz). This means that the CMRR is at least 34.17 dB. The noise figure predicted by the simulation is better than 0.73 dB (equivalent noise temperature smaller than 53 K) for ideally matched amplifier input i.e. 100 Ω differential load. For the actual antenna the amplifier noise figure is smaller than 2 dB (Te is smaller than 169 K in the whole frequency range), Fig. 4.6. The S_{21dd} with the dipole load is higher than 10 dB.

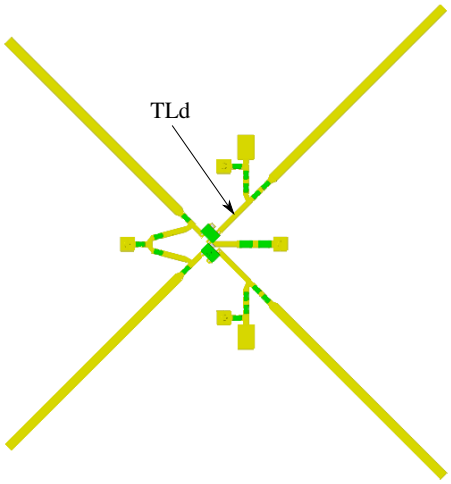

Figure 4.5: Layout of the differential amplifier.

The layout of the proposed active antenna with printed dipole antenna directly connected to the amplifier is in Fig. 4.7. The simulated S_{11} of the active antenna was obtained by importing the S_{11} of the dipole in to AWR and using it as an input load for the amplifier. The return loss is better than 10 dB in the band of interest (1.7 - 2.6 GHz) which means that relative bandwidth is at least 41.86%.

4.5 Measurement

The amplifier and the active antenna were manufactured and measured; the prototypes are in Fig. 4.8, 4.9. The mixed mode S-parameters were obtained in a true differential measurement with Rohde and Schwarz ZVA 67. The measured S_{21dd} is in a very good agreement with the simulation - the discrepancy is less than 0.5 dB, Fig. 4.10. The measured CMMR is a little lower than predicted (at least 31.8 dB), which is still a very good value. There is a difference

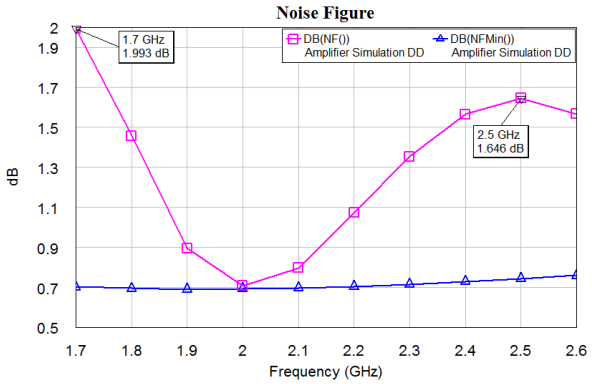

Figure 4.6: Noise figure of the amplifier with input load corresponding to antenna impedance.

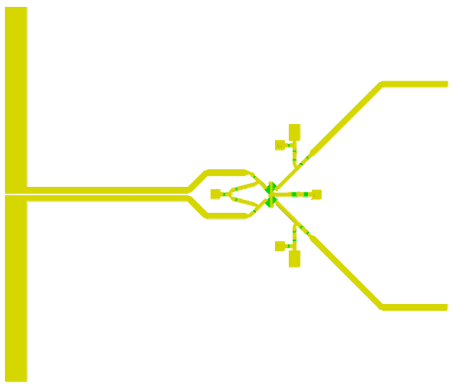

Figure 4.7: Layout of proposed active antenna.

in S_{11} of the active antenna prototype, Fig. 4.11, however it is below -10 dB in the band of interest.

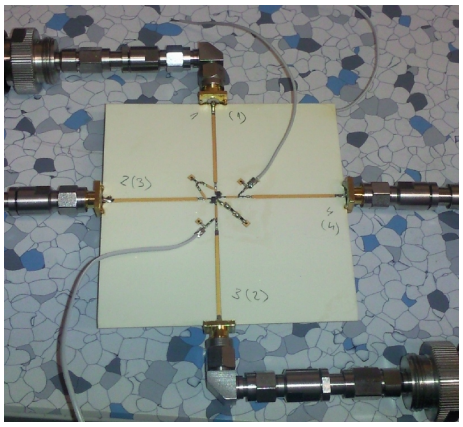

Figure 4.8: Measurement of amplifier prototype.

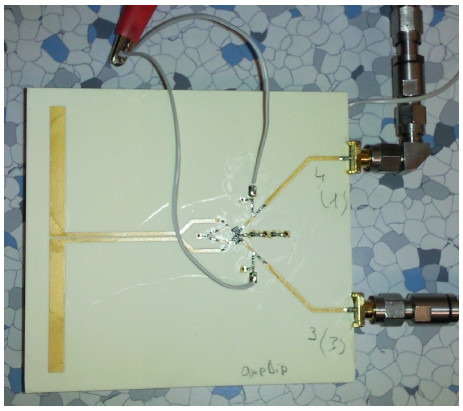

Figure 4.9: Measurement of the active antenna.

4.6 Conclusion

An active antenna is a very promising concept for broad banding a narrow band passive antenna. Furthermore it is possible to design a system with a very low equivalent noise temperature by optimizing both the passive and the active part. The active antenna presented in this paper has a fully differential topology. This means high CMRR (high suppression of spurious CM signals). It has a very low equivalent noise temperature (lower than 169 K) and gain higher than 15 dBi. It is shown that by the active approach it is possible to achieve a very good performance in a wide frequency band (relative bandwidth 41.86%) even with a

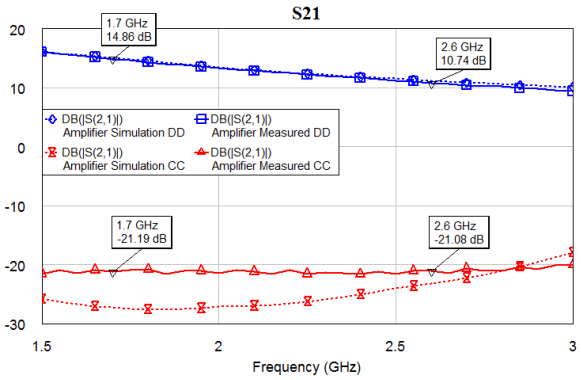

Figure 4.10: Comparison of simulated and measured S_{21} of the amplifier.

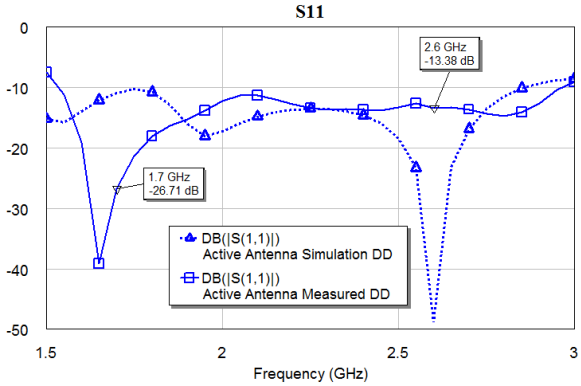

Figure 4.11: Comparison of simulated and measured $S_{11\mathrm{dd}}$ of the active antenna.

passive radiating element with a narrow band performance. A very good agreement between the measurement and the simulation was obtained.

Characteristic modes may become beneficial for differential active antenna design, because of their small dependance on frequency. On the other hand, input impedance is crucial and needs to be effectively optimized. It directly affects stability, gain, noise figure and S_{11}. The capabilities of current TCM tools have to be improved with regard to input impedance optimization to fully utilize modal approach in active differential antenna design.

5

Mesh Generation for TCM

5.1 Introduction

Researchers studying the TCM usually develop their in-house tools for modal analysis, e.g. [25, 33]. One of the tools has been developed in MATLAB at the Department of Electromagnetic Field by M. Capek and P. Hazdra and also the author of this thesis [86, 71]. Nowadays, a coomercial implementation of the TCM is available in the FEKO [4].

As in the case of other methods, in the MoM and the TCM the mesh is one of the crucial inputs which significantly influences both computation efficiency and the accuracy of the results. Thus the aim of this chapter is to present a tool for surface mesh generation, which cooperates with the in-house modal analyzer [71]. Then a simple error analysis is presented for the TCM and using the mesh generation tool, the numerical properties of the solution are verified. This chapter will also present a practical study of the convergence of different modal parameters with mesh density. The important parameters are resonant frequency, the eigen radiation quality factor Q_{eig}, and maximal directivity. The main output of the study is a recommendation for mesh generation for TCM. Sources of the error will be discussed in the following and will be applied to the in-house tool [71] and also the FEKO commercial software [4].

The inputs for the in-house tool [71] are matrices $\mathbf{p}$ and $\mathbf{t}$, containing the surface mesh. Each column of $\mathbf{p}$ contains Cartesian coordinates of a mesh node, and each column of $\mathbf{t}$ contains the indices of three points creating a triangle. There are several mesh generators both commercial and free available. Let's briefly compare some of them in terms of their potential to be used for the in-house TCM tool. The Partial Differential Equation Toolbox (pdetool) [110] for MATLAB offers a mesh generator which is easy to integrate into established tools. However some tests on fractal geometries revealed an unnecessary mesh density in the

regions of overlapping shapes. Also a full mesh density control is rather complicated, because pdetool was designed for partial differential equations with adaptive mesh refinement. The FEKO contains a surface mesh generator designed for MoM. It is possible to run FEKO task from MATLAB i.e. automatically generate the mesh. The NetGen [111] is a C++ code with input geometry defined either by CSG or STL format. It uses the advancing front method to create an initial mesh which is then refined. The mesh density is controlled by assigning a maximal allowed edge length to a piece of the geometry. The CGAL [112] package is written in C++ and contains a plenty of distinct tools for various geometry computations. Among them is a mesh generation package based on the Delaunay refinement algorithm. The distmesh algorithm [113] is based on a force equilibrium idea which produces meshes of high quality. The basic distmesh is only one page of a MATLAB code, however this algorithm is not entirely robust. The mesh density is controlled by a mesh density function. The inputs of the distmesh routine are the signed distance function, representing the geometry, and the element size function, representing the relative distribution of desired edge lengths inside the geometry. Although the geometry can be defined implicitly (by an analytical function) we prefer defining the geometry as a set of polygons and compute the distance from their boundaries.

Important properties of the mentioned generators are listed in Tab. 5.1.

Table 5.1: Comparison of selected mesh generators.

Program name	Input	License	MATLAB code
pdetool [110]	Polygon points	Retail	YES
FEKO [4]	Prefeko file	Retail	NO
NetGen [111]	CSG, STL	LGPL	NO
CGAL [112]	Polygon points	Open Source License	NO
distmesh [114, 113]	Distance function	GNU GPL	YES

5.2 Mesh Generation for TCM

A tool called MeshGen was developed in MATLAB in order to easily define and parametrize the geometry and generate its surface mesh. A suitable algorithm for mesh generation is distmesh [113], written in MATLAB. It allows full mesh control (fixed points, mesh density control), but the biggest advantage is that it is simple to understand and to integrate into

our MATLAB tools. On the other hand, unlike the advanced version of the code, written in C++, the basic version is not fully robust and the generation of the initial set of nodes is not deterministic [113].

MeshGen is capable of surface meshing of 3D planar structures by executing the following steps for each 2D plane of the structure[1]:

- Automatic fixed points are placed on the border to respect the mesh density function, and to avoid small distance from user defined fixed points.
- Mesh points from previously generated 2D planes are used as fixed points.
- An initial set of mesh points is created.
- The mesh point distribution is optimized by the distmesh algorithm.
- The 2D mesh is validated to be conformal with the shape boundary. If the validation is not successful, the mesh will be refined.
- Transformations are applied to the 2D mesh and the result is merged with the previously generated mesh.

Due to the distmesh algorithm, MeshGen produces meshes of high mean triangle quality as well as high minimal triangle quality[2].

The following improvements to the basic MATLAB code [113] have been implemented:

- A deterministic algorithm to generate the initial point set.
- A check that the mesh is conformal with boundary.
- A function which moves points in the proximity of shape boundary to the boundary.
- A posibility to add points to the center of the edge which is longer than the required edge length.
- An edge, which is shorter than the required edge length is replaced with a center point.

All of these features rapidly increase the convergence of the algorithm to a high quality mesh, as well as the algorithm robustness. The initial mesh and the optimized mesh, including simple examples of the local mesh improvements, are plotted in Fig. 5.1.

[1] It is possible to create a mesh of an arbitrary non-planar surface in 3D, e.g. on a Beziér surface, by applying a transformation on $\mathbf{p}$, as was done in [114, p. 64].

[2] The triangle quality $q = 2r_{\text{in}}/r_{\text{out}}; q \in < 0, 1 >$, where r_{in} is the radius of the biggest inscribed circle and r_{out} is the radius of the smallest circumscribed circle [114].

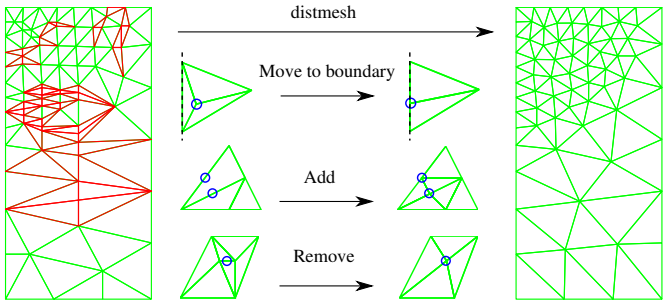

Figure 5.1: Initial mesh (left), triangles with low quality are marked with a red contour. Operations improving algorithm convergence to a high quality mesh (middle). Final mesh (right).

The progress of the generation is plotted in Fig. 5.2, where it can be seen that mean triangle quality is improved with the increasing iteration. The minimal triangle quality is generally improved as well, but there are step increases in the curve due to local mesh improvements and retriangulation if the nodes change position.

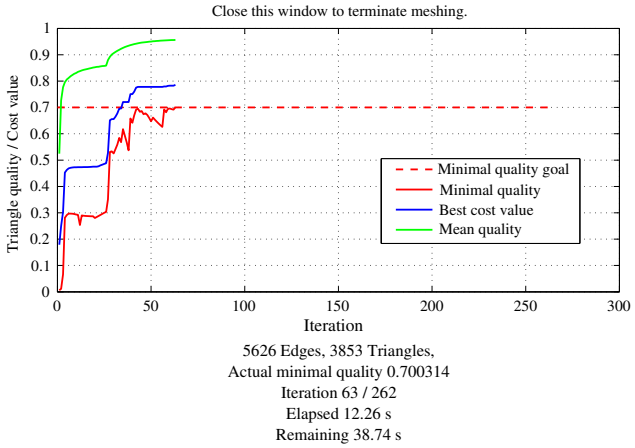

Figure 5.2: Graphical representation of the mesh generation progress.

The structure is implicitly parametrized, so it is not need to write any additional function to change the structure. Instead an internal parameter of the MeshGen object is modified. All features of MeshGen can be started from MATLAB command line and therefore used in a parametric sweep or optimization. MeshGen also supports import and export of the NASTRAN mesh format, so the meshes can be exchanged with other computational tools. The interested reader can download MeshGen from [115]. An example of a mesh generated for an L-probe fed patch antenna is shown in Fig. 5.3.

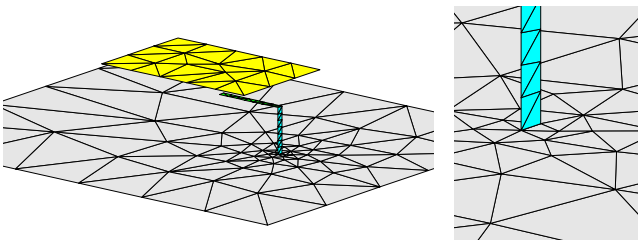

Figure 5.3: Example of the mesh generated by MeshGen: L-probe fed patch antenna (left), detailed view on the connection between the ground plane and the probe (right).

5.3 MeshGen Tool Description

MeshGen is a collection of MATLAB classes and functions[3] dealing with geometry definition, parametrization, boolean operations, transformations and mesh generation. Specifically, the core of the tool is a structure description class CsDesc. This class is responsible for geometry definition, parametrization and mesh generation. For generalized polygon description (i.e. polygon including holes) class Cpd has been created. The class is also responsible for plotting and manipulation with the polygon. Closely related class Cmerge provides polygon merging in 2D.

The whole geometry is created by combining several distance functions (geometry elements). There are predefined distance functions to create a rectangle, a circle, a polygon, an IFS fractal, and a strip. A distance function can be any function with one arbitrary input parameter (usually a vector or a matrix) and two output parameters: Cpd object and a set of mesh fixed points organized into a two column matrix. Therefore, distance functions can be defined by user with the advantage of parametrization by CsDesc class. Such distance function may represent e.g. a meandred dipole. Graphical representation of the structure of the code in in Fig. 5.4.

The mesh generated for particular geometry is organized in $\mathbf{p}, \mathbf{t}$ matrices. A class Cmesh is responsible for mesh operations, such as plotting, merging, duplicate points removal, import and export to NASTRAN format, mirroring and other. Once a final mesh is prepared, characteristic modes or a direct EFIE solution can be computed by the in-house tool [71].

It is also possible to fix the mesh of one or more geometry cuts, while changing dimmensions (or mesh settings) of another part. This can be especially useful for testing sensitivity of numerical methods to mesh changes. Transformations can be applied on the mesh points to produce e.g. conformal or symmetrical meshes. All features of MeshGen are available from

[3]Current version is v03p and contains more than 5000 lines of code.

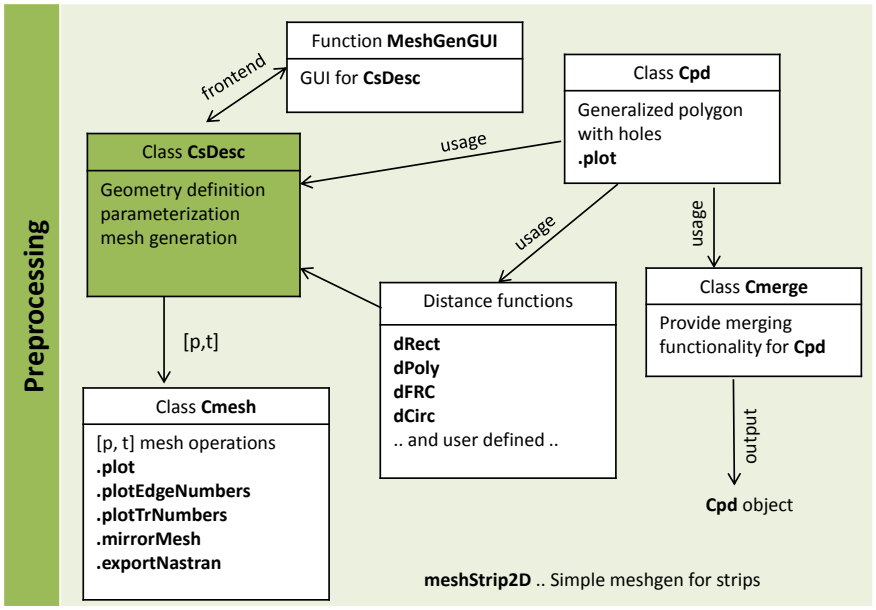

Figure 5.4: Relation between classes and functions in MeshGen.

command line for an optimization or a parameter sweep. The most often used operations can be also defined by a simple graphical user interface meshGenGUI. Examples of meshes generated by MeshGen are in Fig. 5.5.

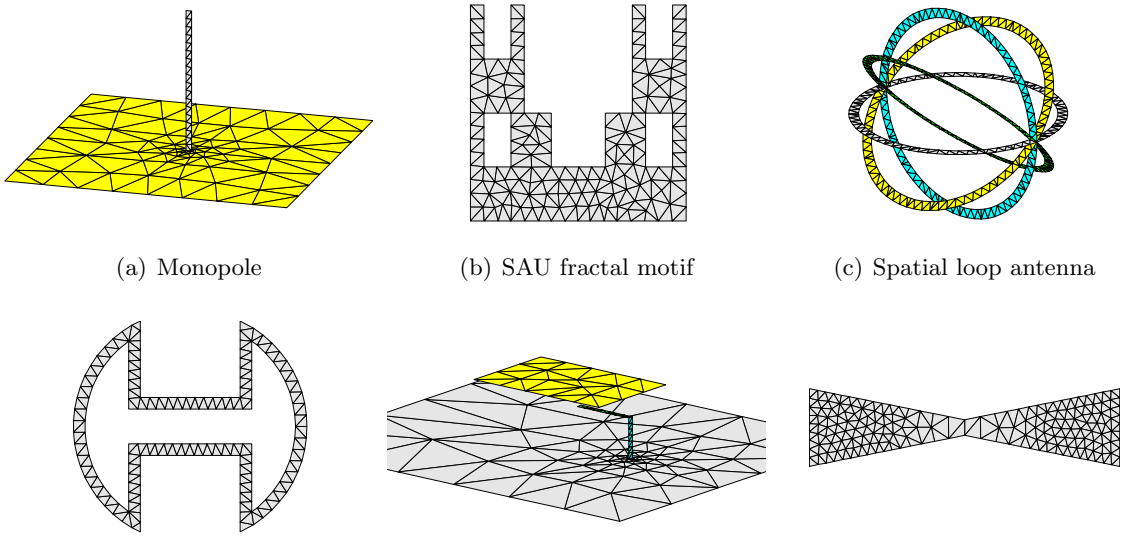

(a) Monopole (b) SAU fractal motif (c) Spatial loop antenna

(d) Modified loop antenna (e) L-probe fed patch antenna (f) Bowtie antenna

Figure 5.5: Example of meshes generated by MeshGen.

5.4 Numerical Computation of Characteristic Modes

Characteristic modes $\boldsymbol{J}_n$ of surface S satisfy the operator equation

$$\mathcal{X}\boldsymbol{J}_n = \lambda_n \mathcal{R}\boldsymbol{J}_n, \tag{5.1}$$

where $\mathcal{X}$ and $\mathcal{R}$ are the imaginary and real parts of the EFIE operator relating tangential components of the surface current and scattered electric field. Corresponding to each mode is the eigennumber λ_n. Harrington and Mautz [20] proposed to numerically solve (5.1) by the method of moments. Thus the current density of mode n is approximated by a set of basis functions $\boldsymbol{w}_v$ multiplied by unknown coefficients $I_{n,v}$.

$$\boldsymbol{J}_n \approx \sum_v I_{v,n}\boldsymbol{w}_v. \tag{5.2}$$

Applying the usual MoM procedure with testing functions $\boldsymbol{w}_u$ we obtain the following matrix equation [20]

$$\mathbf{X}\boldsymbol{I}_n = \hat{\lambda}_n \mathbf{R}\boldsymbol{I}_n. \tag{5.3}$$

Note that λ_n is not exactly equal to $\hat{\lambda}_n$ due to an approximation made in (5.2).

The integrals involved in calculating matrix elements are usually evaluated by numerical quadrature and thus contain errors. Such errors (perturbations) have been mathematically studied in [116] with the following result. Consider a perturbed problem

$$\tilde{\mathbf{X}}\tilde{\boldsymbol{I}}_n = \tilde{\lambda}_n \tilde{\mathbf{R}}\tilde{\boldsymbol{I}}_n, \tag{5.4}$$

where the matrices are of the form $\tilde{\mathbf{X}} = \mathbf{X} + \varepsilon\mathbf{G}$ and $\tilde{\mathbf{R}} = \mathbf{R} + \varepsilon\mathbf{H}$, and $\|\mathbf{G}\| = \|\mathbf{H}\| = 1$. Supposing that $\hat{\lambda}_n$ is a simple eigenvalue, $\mathbf{R}$ is nonsingular[4] [116] and considering that both $\mathbf{R}$ and $\mathbf{X}$ are symmetrical,

$$\tilde{\lambda}_n - \hat{\lambda}_n = \varepsilon \frac{\boldsymbol{I}_n^{\mathrm{T}}(\mathbf{G} - \hat{\lambda}_n\mathbf{H})\boldsymbol{I}_n}{\boldsymbol{I}_n^{\mathrm{T}}\mathbf{R}\boldsymbol{I}_n} + \mathcal{O}(\varepsilon^2). \tag{5.5}$$

Omitting the higher order terms

$$\tilde{\lambda}_n - \hat{\lambda}_n \approx \varepsilon \frac{\sum_u \sum_v I_{n,u} I_{n,v}(G_{u,v} - \hat{\lambda}_n H_{u,v})}{\sum_u \sum_v I_{n,u} I_{n,v} R_{u,v}}. \tag{5.6}$$

From (5.6) it is evident that for minimizing the difference $\tilde{\lambda}_n - \hat{\lambda}_n$ one should minimize the term $(G_{u,v} - \hat{\lambda}_n H_{u,v})$ in the regions with high $\boldsymbol{I}_n$. Note that the value of $I_{n,u}$ is related to

[4] Note that for certain frequencies, EFIE impedance matrix can be close to singular [81].

the dot product of the $\boldsymbol{J}_n$ vector and the vector basis function $\boldsymbol{w}_u$. Thus it is more robust to refine regions with high $\boldsymbol{J}_n$ than to refine regions with high $I_{n,u}$.

In the in-house tool [71], $\boldsymbol{w}_v$ and $\boldsymbol{w}_u$ are the RWG basis functions [69] and (5.3) is computed by direct decomposition or by an iterative method in MATLAB. FEKO uses the Implicitly Restarted Arnoldi Method [117], an iterative procedure to obtain several most significant characteristic numbers and vectors. The time consumption of both approaches for one frequency is plotted in Fig. 5.6. The in-house tool uses a 9-point barycentric subdivision and centroid approximation [70, Ch. 2] in the computation of $\mathbf{Z}$ matrix elements, thus it is a bit faster than FEKO, however one can expect more accurate results for the same mesh from FEKO.

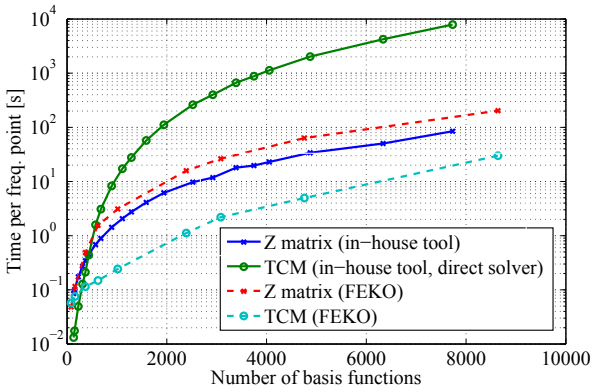

Figure 5.6: Computation time as a function of the number of basis functions, two modes are required in FEKO. Computations performed in single-core mode, on an Intel Core i7-3770K @ 3.5GHz CPU.

The complexity of the direct solver is much higher than the complexity of the $\mathbf{Z}$ matrix computation as well as the iterative method, Fig. 5.6. The iterative solver is, however, preferred for structures larger than approx. 800 inner edges (i.e. RWG basis functions). All simulations were computed in a single-core mode on an Intel Core i7-3770K @ 3.5GHz CPU.

5.5 Numerical relative convergence of modal parameters

This section presents a convergence study of modal resonant frequency $f_{\mathrm{res},n}$, defined as the frequency where $\lambda_n = 0$, modal radiation quality factor

$$Q_{\mathrm{eig},n} = \frac{\omega}{2}\left|\frac{\partial \lambda_n}{\partial \omega}\right|, \tag{5.7}$$

and maximal modal directivity $D_{\max,n}$ with mesh density. The surrounding medium for all structures is a vacuum.

Convergence studies are necessary to eliminate the effect of the error cancellation mechanism [118], which can be observed if several sources of error eliminate each other and the result thus appears to be accurate.

Let us define a relative error as

$$\epsilon(x) = \frac{|x - x_{\text{ref}}|}{x_{\text{ref}}}, \tag{5.8}$$

where x is one of the quantities of interest: $f_{\text{res},n}$, or $Q_{\text{eig},n}$ or $D_{\max,n}$. The reference value x_{ref} should ideally be the precise value (as computed e. g. from an analytical formula) or a measured value. Analytical formulas for modes on a conducting sphere can be found in [26], however they will not be used here since an RWG mesh cannot fully describe the geometry curvature. Measured values are not available for the modal quantities. Other full-wave methods also cannot be used as a reference. For instance, the commonly used measure of resonance (input susceptance of the antenna is equal to zero) is not equal to the modal resonance unless only one mode is excited. Thus there are two options: to use a result from much denser RWG mesh as a reference, or to use a solution using higher order basis functions as a reference. Results from FEKO software using a relatively fine mesh and basis functions denoted as order 2.5 are chosen as a reference in this paper.

In order to compare different mesh refinement schemes for different structures, we use the following number associated with each mesh

$$m = \frac{c_0}{f_{\text{res,ref},n} \min(L)}, \tag{5.9}$$

where c_0 is the speed of light and $f_{\text{res,ref},n}$ is the resonance frequency of mode n computed by FEKO reference software and L is the set of lengths of edges inside the structure. Number m has thus the meaning of the number of smallest edges per wavelength. Note that m does not take into account the actual distribution of the edge lengths in the structure, and that such criteria will be much more difficult to define, implement and understand.

Meshes will be generated using MeshGen requiring minimal triangle quality of 0.8. While this criterion is not always satisfied (generation stops because the maximal number of iterations is exceeded) the minimal quality for all the studied meshes is not lower than 0.6.

5.5.1 Strip Dipole

The first studied structure is a strip dipole 30 mm in length and 0.6 mm in width. The structure was simulated using an adaptive frequency sweep [71] with increasing uniformly distributed mesh density.

Fig. 5.7 shows that the dominant resonant frequency converges with increased number of edges inside the structure. Even the coarsest mesh presents $\epsilon(f_{\mathrm{res},1})$ smaller than 1.5%, and meshes with more than 91 edges have the relative error $\epsilon(f_{\mathrm{res},1})$ under 0.5%. However even for 16557 edges, there is still a small difference of 4 MHz (0.096%) from the FEKO result using 2.5th order basis functions. This fact can indicate either very slow convergence of our tool for small relative errors, or that our tool converges to a slightly different value.

There is a very small dependance of the results on the number of triangles across the strip, with the exception of the step increase from 1 triangle per strip width to two triangles which appears between $m = 107$ and $m = 223$, Fig. 5.7. In other words proper discretization of the edge singularity of the charge (see e.g. [119]) is not the crucial point for eigenvalue precision.

In the next step, the central part of the dipole was meshed with higher or lower density than the rest and the size of the central part was varied. However, the difference in convergence was disputable and the uniform scheme converged more smoothly than the others, thus it was recognized as the optimal refinement scheme for the dipole.

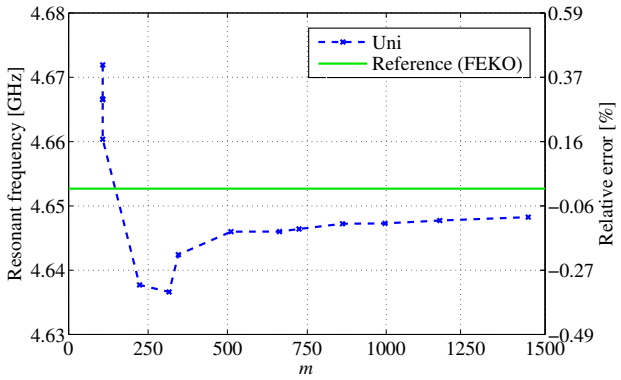

Figure 5.7: Convergence of the resonant frequency of mode 1 of the dipole 30 mm in length and 0.6 mm in width. Uniformly refined mesh.

5.5.2 Rectangular Patch

The second structure is a rectangular patch 25 mm in length and 21.5 mm in width, placed 3 mm above an infinite PEC plane. Since the current density of the first mode is spread over the patch, Fig. 5.8, the convergence of the uniformly refined mesh was generally better than the locally refined mesh. The exception was the scenario denoted as V01, in which the mesh was coarser in the regions with high magnitude of current density, Fig. 5.8. This paradoxical behavior can be explained as follows. The two edges of the patch are discretized by bigger triangles, thus the corresponding current density is lower, see Fig. 5.8. This means that according to (5.5) these big triangles (with bigger error) become less significant for computation of $\tilde{\lambda}_n$, in other words the value of $\tilde{\lambda}_n$ will be more affected by smaller triangles with smaller error.

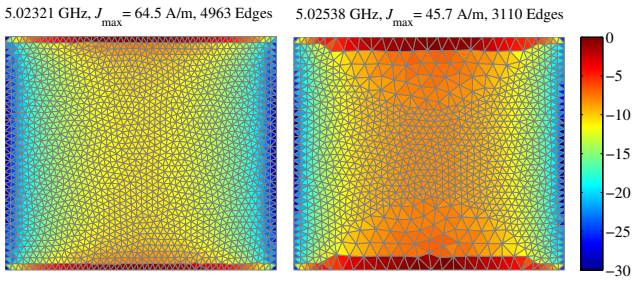

Figure 5.8: First mode of a rectangular patch 3 mm above ground plane at its resonance, uniformly refined mesh (left) and V01 refined mesh (right). A normalized logarithmic scale is used for both cases.

Fig. 5.9, 5.10 show very similar convergence of both uniform refinement (denoted as Uni) and the V01 refinement of the resonant frequency and Q_{eig}. This behavior was expected since both results are related to the eigenvalue. In contrast, there is a difference in maximal directivity, Fig. 5.11, which results from the difference in current density for Uni and V01 refinement. However the difference between them is reduced with increasing m.

5.5.3 U Shaped Patch

The next structure is the same patch as in the previous section with a slot 15 mm in length and 2 mm in width. The dominant mode has a very localized current density, Fig. 5.12, thus it is ideal for applying a non uniform mesh refinement scheme. To observe the differences between a properly refined mesh and an ineffective refinement, two schemes were proposed. Meshes that are properly refined in the regions with high amplitude of the modal current

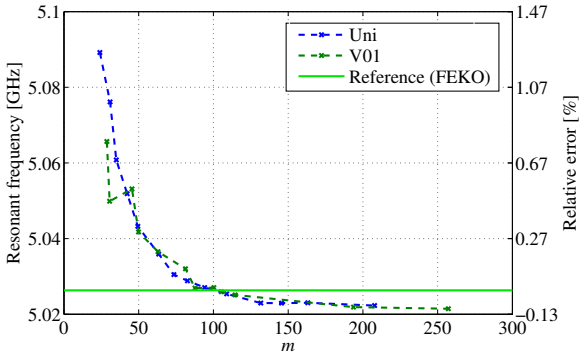

Figure 5.9: Convergence of the resonant frequency of the rectangular patch for different refinement schemes.

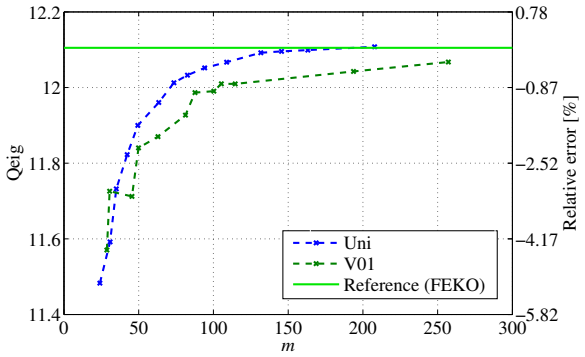

Figure 5.10: Convergence of Q_{eig} of the rectangular patch for different refinement schemes.

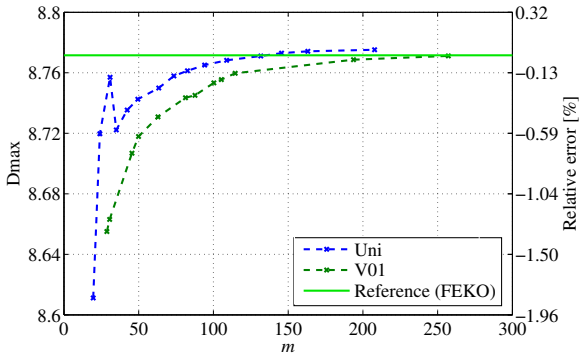

Figure 5.11: Convergence of maximal directivity at resonance of the rectangular patch for different refinement schemes.

density are denoted as V01, Fig. 5.12. By contrast, the scheme denoted as V02 is not refined near the maximum of $\|\boldsymbol{J}_n\|$, see Fig. 5.13, and is ineffective from the error minimization point of view.

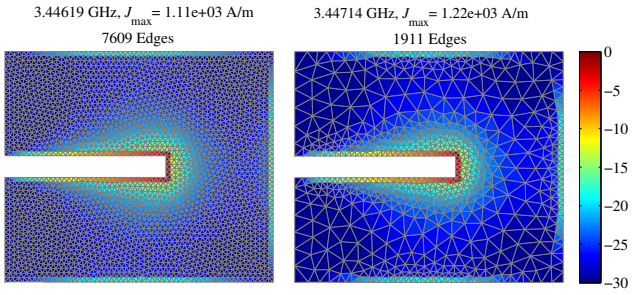

Figure 5.12: First mode at its resonance, uniformly refined mesh (left) and V01 mesh (right), normalized logarithmic scale.

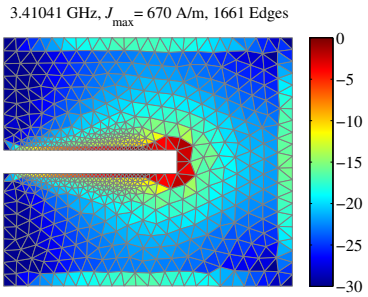

Figure 5.13: First mode at its resonance, V02 refinement scheme, normalized logarithmic scale

The slow convergence of V02 is clearly visible in Figs. 5.14, 5.15, 5.16. On the other hand, the V01 results are very close to Uni with similar minimal edge length. Note that the total number of edges, which directly influences the simulation speed, Fig. 5.6, is reduced approximately by a factor of 3-4 for the V01 mesh. Therefore computing 6 frequencies took 9.25 minutes and 1 minute for the uniform and V01 structures of Fig. 5.12, respectively. The nice speedup of 9.25 is interesting, especially for an optimization. The difference would be enormous for the direct solver: 15.41 hours versus 10.74 minutes (6 freq. samples).

5.5.4 Circularly Polarized Triangular Patch

In this section, a triangular patch with a slot will be analyzed and convergence graphs both for the in-house tool and for FEKO will be presented. This type of patch can be used for

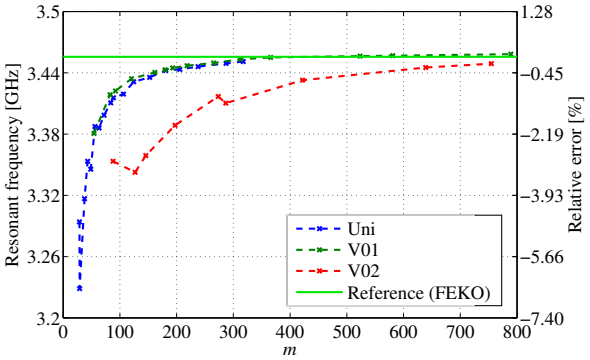

Figure 5.14: Convergence of resonant frequency of the patch with a slot for different refinement schemes.

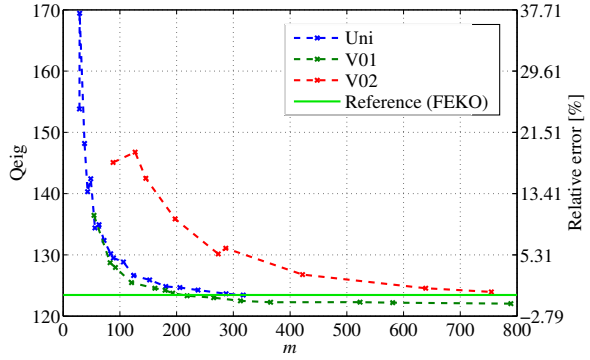

Figure 5.15: Convergence of Q_{eig} of the patch with a slot for different refinement schemes.

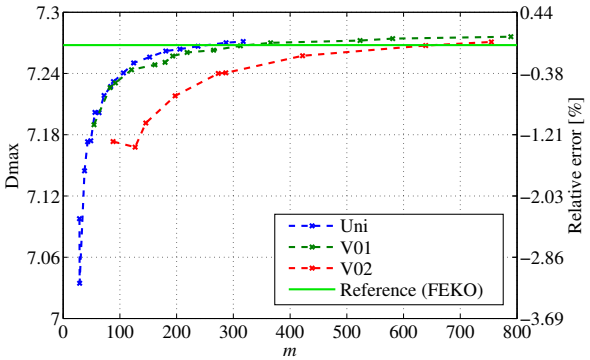

Figure 5.16: Convergence of maximal directivity of the patch with a slot for different refinement schemes.

circular polarization [120, Ch. 5]. For proper functionality, circularly polarized antennas combine two orthogonal modes in a specific way. Thus in order to analyze (and design) such antennas, accurate results for both modes have to be obtained.

While the first mode of the triangle with a slot has the current density localized near the slot, the second mode is distributed over a dominant part of the patch, Fig. 5.17. From the mesh refinement point of view, mode 1 will resemble the dominant mode of a slotted patch and mode 2 will resemble the mode of a rectangular patch. The mesh refinement strategies from sections 5.5.2 and 5.5.3 should therefore also apply for the triangle with a slot.

The mesh refinement appropriate for mode 1 is denoted as V01, Fig. 5.18, and it reduces the number of edges by a factor of approx. 1.6-1.8 for a uniform mesh with similar accuracy. The convergence of $f_{\mathrm{res},1}$ is quite comparable for the Uni and the V01 mesh, Fig. 5.19, while the convergence $f_{\mathrm{res},2}$ is significantly better for Uni, Fig. 5.20. Although the absolute values obtained for the same meshes imported into FEKO and using low order basis functions differ, the trend of the curves in Fig. 5.19 - 5.20 is the same as the trend of the curves computed by the in-house tool. The reason why $f_{\mathrm{res},2}$ differs for V01 and Uni is that the mode 2 current has high values in the regions with low mesh density of the V01 mesh Fig. 5.18.

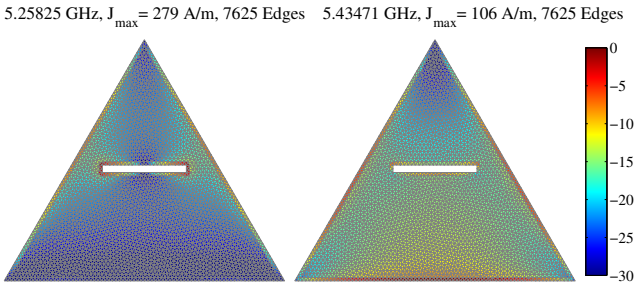

Figure 5.17: First mode at its resonance, uniformly refined mesh, normalized logarithmic scale.

The Q_{eig} of both modes is affected by the refinement strategy in the same manner as f_{res}. Note that the eigen Q factor is somehow more sensitive to mesh density than the resonant frequency or the maximal directivity.

The V01 mesh is not suitable for obtaining the small ϵ of mode 2 results, therefore the mesh is additionally refined in the lower part of the triangle denoted as V02, Fig. 5.18. This refinement scheme preserves good convergence for both modes, Fig. 5.19 - Fig. 5.24, however, the mesh density with respect to a uniform mesh is reduced only in the top part of the patch and the reduction factor is only 1.1-1.2. Nonetheless for a high number of edges this factor

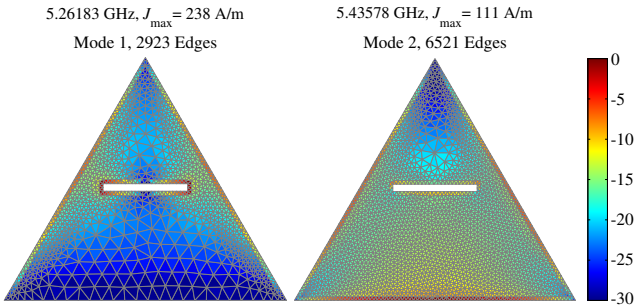

Figure 5.18: First mode at its resonance, V01 refined mesh (left) and V02 refined mesh (right), normalized logarithmic scale.

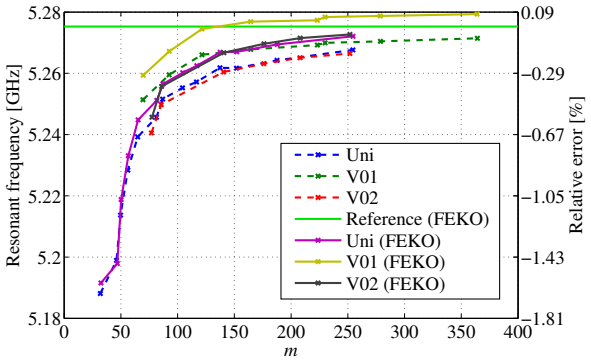

Figure 5.19: Convergence of the resonant frequency of the triangle with a slot, mode 1.

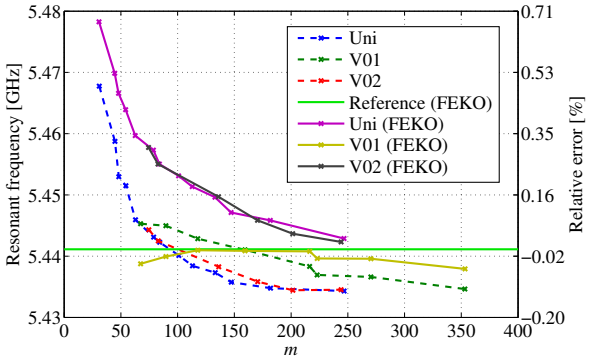

Figure 5.20: Convergence of the resonant frequency of the triangle with a slot, mode 2.

will become more significant, e.g. a Uni mesh of 7625 edges was computed in 11.95 minutes while a V02 mesh of 6521 edges took only 8.57 minutes (8 frequency points, iterative solver).

The V02 meshes were also imported to FEKO and the results are quite close to the FEKO Uni mesh results. Thus we conclude that the presented results are applicable to the commercial implementation of characteristic modes theory [4].

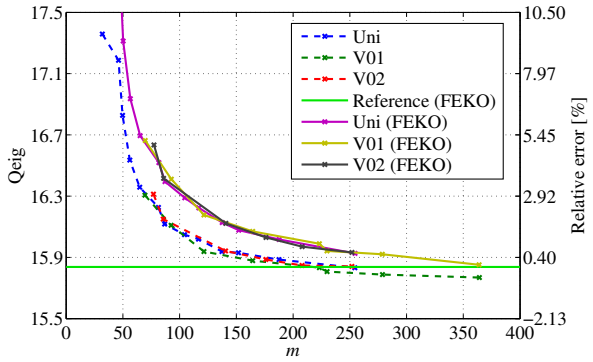

Figure 5.21: Convergence of Q_{eig} of the triangle with a slot, mode 1.

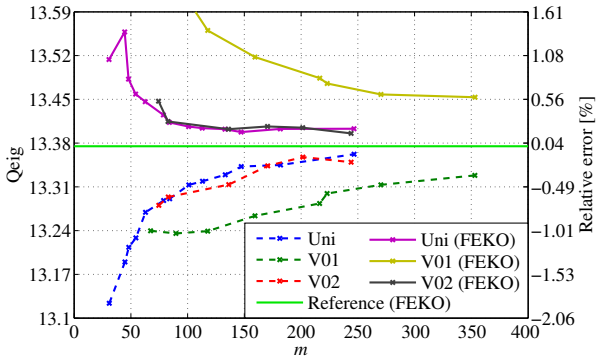

Figure 5.22: Convergence of Q_{eig} of the triangle with a slot, mode 2.

5.6 Conclusion

In this chapter a tool for surface mesh generation in MATLAB has been described. This tool is used in conjunction with an in-house TCM tool to study the convergence of the numerical implementation with increased mesh density. A simple error analysis of the TCM formulation is presented. It reveals the interesting property that the eigenvalues are affected by the

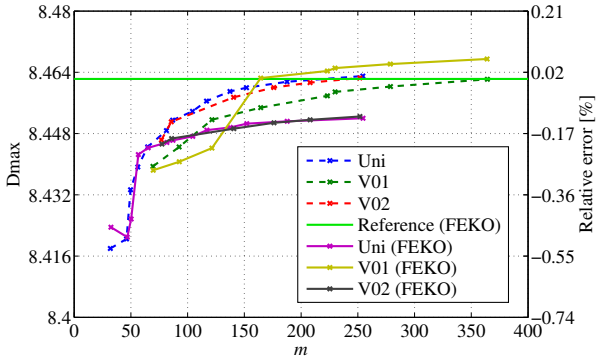

Figure 5.23: Convergence of $D_{\max}$ of the triangle with a slot, mode 1.

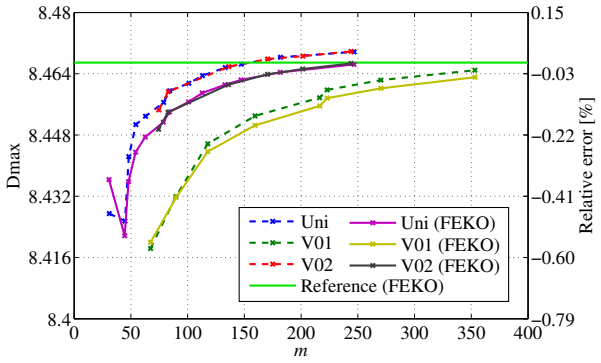

Figure 5.24: Convergence of $D_{\max}$ of the triangle with a slot, mode 2.

approximation errors in the matrix elements multiplied by $I_{n,u}I_{n,v}$. This result indicates that the mesh should be refined in the regions where the current magnitude is high.

The theory has been tested on the dominant mode of a dipole, a rectangular patch, and a rectangular patch with a slot. Convergence curves for resonant frequency, Q_{eig} and maximal directivity for different mesh refinement schemes have been compared. The results are in accordance with the theoretical derivation. It has also been observed that mesh refinement is much more suitable for modes with localized current, where high simulation speedup can be obtained for non-uniform mesh refinement with good relative accuracy.

Generally, the computation of characteristic modes by MoM converges with an increased number of basis functions (we suppose that the round off errors were insignificant for all presented computations). However, no rule of thumb for number of basis functions per wavelength for a given relative error has been deduced. Specifically, the number m necessary to obtain relative error $\epsilon(f_{\text{res}}) < 1\%$ for the dipole, the rectangular patch, the rectangular patch with a slot and the circularly polarized triangle was (less than 100), 30, 109 and 53 respectively. Q_{eig} tends to be the most sensitive parameter, and needs careful choice of the mesh.

The recommendations for mesh refinement have been tested on a circularly polarized patch in the in-house tool and also in FEKO (using low order basis functions). Although they were slightly different in absolute values, which may be due to approximations in the in-house tool, the results were qualitatively equivalent and preserved the same trends.

6

Excitation of Characteristic Modes

6.1 Introduction

It is implied by the definition of characteristic modes, that they are computed without an excitation, which is represented by an arbitrary impressed field $\boldsymbol{E}^{\mathrm{i}}$. It have to be noted, that once the geometry, on which current density can flow, is changed, the modes will change as well. This fact complicates a usage of characteristic modes for quantitative analysis of antennas. For instance, modes of a patch antenna with a discrete port (or a stub) of certain dimensions are valid only for the particular position of the discrete port. On the other hand, number of examples support the speculation, that the change of the position of the port, which is electrically much smaller than the patch, actually does not dramatically change the modes on the patch. Similar behavior was observed in [26, Ch. 6], where the input impedance of the antenna correlates with the position of the feed with respect to the mode. Another example may be the transmission line model of a rectangular patch antenna, which implies, that the position of the edge connected microstrip line affects the input impedance in correspondence with the current on the patch. Similar principle was utilized to develop specialized small capacitive and inductive coupling elements to excite multiple modes for MIMO applications [38, 37].

These examples, found in literature inspired the author to seek for a method which can explain coupling of the modes to an excitation structure and to express it in a qualitative way. So far, the modes have been used for qualitative and quantitative analysis of various wire and planar antennas. While for wire antennas even the feed (port) position can be optimized without the necessity to recalculate the modes, to be able to change feed position for planar antennas, the modes have to be recalculated in general.

The aim of this chapter is to review the mechanism of excitation of characteristic modes and develop a method which will enable computing of excitation coefficients for a feeding structure coupled to a planar motif. Consequently, it will become possible to take advantage of one of the important features of TCM - summation formulas for various antenna parameters such as radiation pattern or input admittance. The developed procedure should be faster than a recalculation of the modes when the position of a feed with respect to a planar motif is changed.

6.2 Modes of a System of Coupled Scatterers

The method determining a coupling between individual characteristic modes on a planar structure uses the modes computed by the in-house TCM solver [71, 86] with the core implemented by Miloslav Čapek. The individual structure at free space will be denoted as a *scatterer* and several coupled scatterers will be called a *system of scatterers* (or simply a system). The terms scatterer and system of scatterers in this sense was adopted from [33], where they were used to describe a sub-structure modes. Note, however, that here both scatterers may be excited, but it is assumed, that they are not electrically connected.

The idea presented in this section may resemble the characteristic basis function method (CBFM) [121], where the structure is divided into blocks and basis functions are computed in each of the blocks. The main difference is that CBFM is more general[1] and computationally effective but the basis functions does not provide an interpretation of scatterer physical behavior.

Characteristic modes were used as expansion functions already in [7], with the difference, that the modes of entire system were considered. The idea of using modes of a scatterer as sub-sectional basis functions was investigated in [25, 122] with possible application to antenna arrays. However a residue between the proposed method and the direct solution was reported [122], and had to be suppressed by adding a "source mode" to the set of characteristic modes. We will demonstrate, that in our approach the source mode is not necessary.

Throughout this section, m, n will denote mode indexes, which may be on different scatterers and u, v will denote the indexes of RWG basis functions. First, consider expanding the surface current density $\boldsymbol{J}$ on a system of scatterers.

$$\boldsymbol{J} \approx \sum_{n=1}^{N} c_n \boldsymbol{J}_n \tag{6.1}$$

[1] There is no restriction with regard to the electrical connection of the blocks.

where $\boldsymbol{J}_n$ are the characteristic modes of individual scatterers. Note that the modes are not equal to the modes of an entire system. Then the usual method of moments procedure is applied on (2.1) and a matrix equation reads

$$\mathbf{Z}\boldsymbol{c} = \boldsymbol{g}, \tag{6.2}$$

where $\boldsymbol{g}$ is an excitation vector with elements $\langle \boldsymbol{J}_m, \boldsymbol{E}^{\mathrm{i}} \rangle_s$ and the $\mathbf{Z}$ matrix elements are

$$Z_{m,n} = \langle \boldsymbol{J}_m, \mathcal{Z}\boldsymbol{J}_n \rangle_s. \tag{6.3}$$

Characteristic modes of a scatterer are computed numerically by method of moments using RWG basis functions $\boldsymbol{w}$ for expansion and testing, i.e. the modes are approximated as

$$\boldsymbol{J}_n \approx \sum_{v=1}^{V} I_{n,v} \boldsymbol{w}_v. \tag{6.4}$$

Next it is necessary to compute the elements of $\mathbf{Z}$ matrix. By comparing (6.3) with (2.21) we find a simple relations if the modes m and n are on the scatterer:

$$Z_{m,n} = \begin{cases} 1 + \mathrm{j}\lambda_m, & m = n \\ 0, & m \neq n. \end{cases} \tag{6.5}$$

If the modes are located on a different scatterer, elements $Z_{m,n}$ have to be evaluated numerically

$$Z_{m,n} = \langle \boldsymbol{J}_m, \mathcal{Z}\boldsymbol{J}_n \rangle_s = \int_{\Omega} \boldsymbol{J}_m \cdot \mathcal{Z}\boldsymbol{J}_n \, \mathrm{d}S = \sum_{u=1}^{U} \sum_{v=1}^{V} I_{m,u} I_{n,v} \langle \boldsymbol{w}_{m,u}, \mathcal{Z}\boldsymbol{w}_{n,v} \rangle_s. \tag{6.6}$$

Notice that $\langle \boldsymbol{w}_{m,u}, \mathcal{Z}\boldsymbol{w}_{n,v} \rangle_s$ is the u,v-th element of RWG impedance matrix. There is no singularity in the integral kernel of (6.6), since for different scatterers $m \neq n$.

The result of the described procedure is vector of modal expansion coefficients $\boldsymbol{c}$, thus if the modes expansion vector in (6.4) is known, the port current I_{in} can be computed. Interestingly, characteristic modes of entire system can be reconstructed from the modes of individual scatterers. Following the notation of (6.2)

$$\Im\{\mathbf{Z}\}\boldsymbol{c}_a = \lambda_a \Re\{\mathbf{Z}\}\boldsymbol{c}_a, \tag{6.7}$$

where $\boldsymbol{c}_a$ are expansion coefficients of mode a of the system and with eigenvalue λ_a. If the structure is changed, only the $Z_{m,n}$ for different scatterers need to be recalculated and $\mathbf{Z}$ inverted. It is expected, that number of modes necessary to approximate the system is much smaller than total number of RWG basis functions, the inversion time will be negligible. The time required for recalculation will be thus determined by the evaluation of matrix elements

in (6.6). It is interesting to note, that storage requirements for characteristic modes of a scatterer are much smaller than storage requirements of a scatterer's impedance matrix. The methods of obtaining direct solution and characteristic modes described in this section will be called ChMBF[2] method.

6.3 Verification of the ChMBF Method

It will be shown in this section, that characteristic modes of a scatterer in free space can be used as basis functions for an antenna consisting of a system of coupled scatterers. The results will serve as a verification of the derivations of the previous section and of the numerical implementation. Coarse meshes are used for comparison purposes to speedup the simulation. The ChMBF code is not yet as optimized as the in-house tool, which has been developed for much longer time. Nonetheless, the complexity of the algorithm is lower than the full TCM when a sweep or an optimization of relative position of the scatterers is in concern, as discussed in the end of Section 6.4.

First, consider a rectangular patch 56 x 37 mm, placed in the height $H = 22.5$ mm above an infinite PEC plane and excited by a strip L-probe of width $W_s = 2$ mm, vertical part length $L_v = 15$ mm and horizontal length $L_h = 22.5$ mm and probe offset $D = 0$, Fig. 6.1(a), [8]. Using the method of images, the geometry will be modeled in a mirrored configuration[3], Fig. 6.1(b).

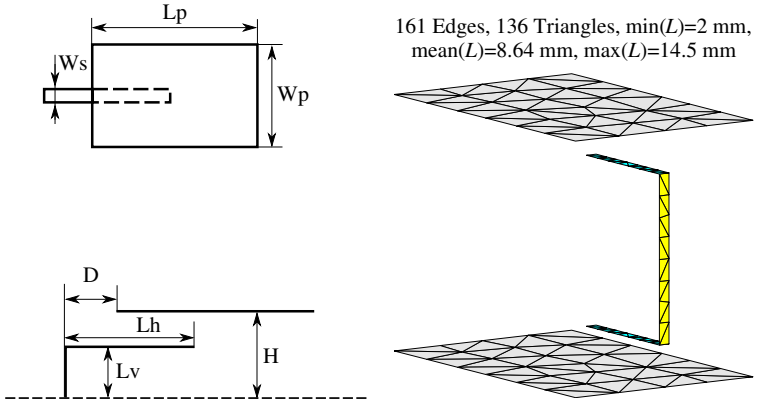

(a) Dimensions (b) Mesh

Figure 6.1: Mirrored configuration of a rectangular patch, excited by an L-probe.

[2]Characteristic modes as basis functions.

[3]The mirrored configuration is chosen because the in-house tool currently does not support meshes touching the infinite PEC plane.

The structure is meshed by MeshGen, Chapter 5, excited by a voltage gap, connected to the middle of the mirrored L-probe. Input impedance is computed by the RWG MoM. Than, characteristic modes of individual scatterers - the patch and the L-probe - are computed. Note, that the mesh of the scatterers is kept the same in all simulations. For comparison purposes, maximal number[4] of numerically obtained modes is used. All modes which has nonzero current in the middle of the L-probe are used for structure excitation represented by vector $\boldsymbol{g}$ in (6.2) and the input impedance is computed by the ChMBF method, Fig. 6.2. The real and imaginary part of input impedance of the L-probe fed rectangular patch antenna is in perfect agreement wit the RWG MoM solution. The coupling between the two structures plays important role, Fig. 6.2, and is taken into account by both approaches.

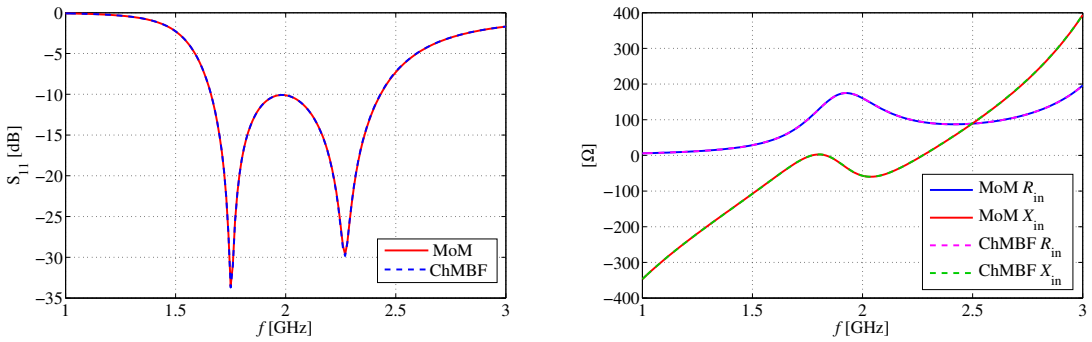

(a) All modes used in ChMBF method.

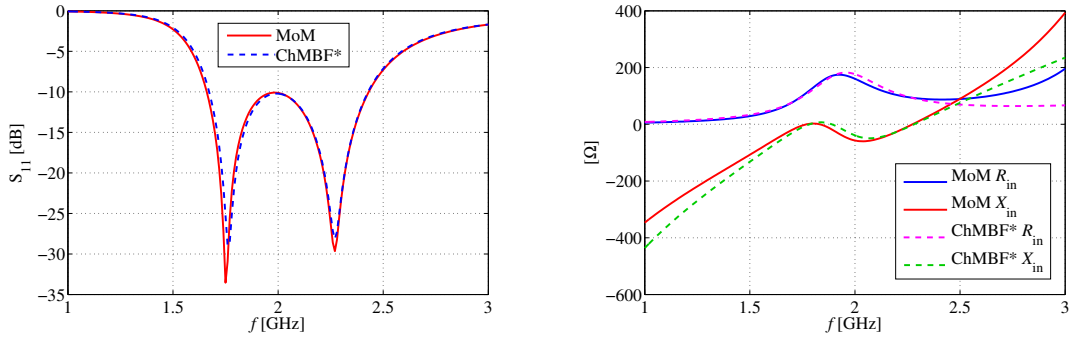

(b) One mode on the patch and one mode on the probe was used (denoted as ChMBF*).

Figure 6.2: S_{11} and input impedance computed by a direct moment solution of EFIE and by ChMBF method. The reference impedance for S-parameters is 100 Ω, which is equivalent to 50 Ω in the case of infinite PEC plane.

It is expected, that for the ChMBF method, excitation of higher order modes, together with a strong coupling between the structures will become a challenging problem. Therefore

[4]Equal to the dimension of the impedance matrix.

the second considered example is the second iteration SAU fractal motif from Fig. 3.2, closely coupled to an asymmetrically placed L-probe. The gap between the motif and the probe is 1 mm (0.0083 wavelengths at 2.5 GHz).

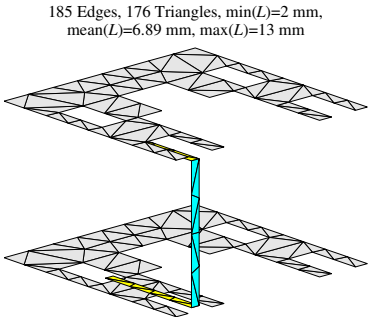

Figure 6.3: Mirrored configuration of a SAU motif, excited by an L-probe.

Moreover the probe is placed asymmetrically and provides a localized coupling, which will excite higher order modes of the self-affine motif. This can be easily checked by inspecting the current distribution in Fig. 6.4, which is highly asymmetrical and different from the several first modes, see Fig. 3.2.

The input impedance is plotted in Fig. 6.5, and a difference between the two methods is observed. On the other hand, its magnitude is quite small, thus it is probably due to finite numerical precision of the method[5]. Note, that the impedance is a nontrivial function of frequency, which confirms, that several modes are strongly contributing to the antenna performance in the selected frequency range.

6.4 Correlation between Scatterer ChM and System ChM

It was demonstrated, that the total current on a system of scatterers can be understood as a weighted sum of individual scatterer's characteristic modes. It has been observed that the modes of a system often resemble the modes of a single scatterer. This effect will be investigated in terms of the correlation of a current density distribution in this section. The tests will be performed on the same antennas as in the previous section.

Consider an a-th mode of the system of scatterers, represented by RWG expansion coefficient vector $\boldsymbol{I}_{\mathrm{sys},a}$, see (6.4). Then the *correlation coefficient* ρ with the m-th mode of a

[5] Also matrix condition number can play important role, further investigation of the discrepancy have not been yet undertaken.

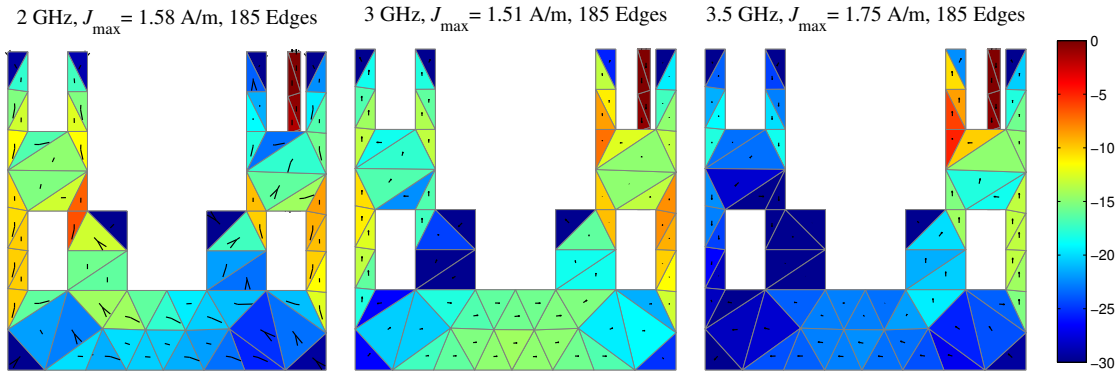

(a) RWG MoM, normalized logarithmic scale.

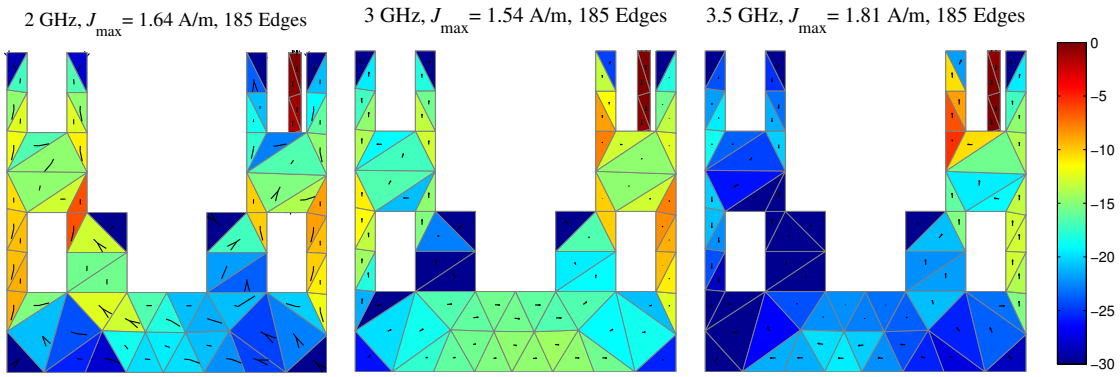

(b) ChMBF, normalized logarithmic scale.

Figure 6.4: Top view of the current distribution on the SAU, highly coupled to the L-probe at 2, 3, and 3.5 GHz. The small difference between RWG MoM and ChMBF is noticeable in the amplitude of the currents and in the lower left part of the motif.

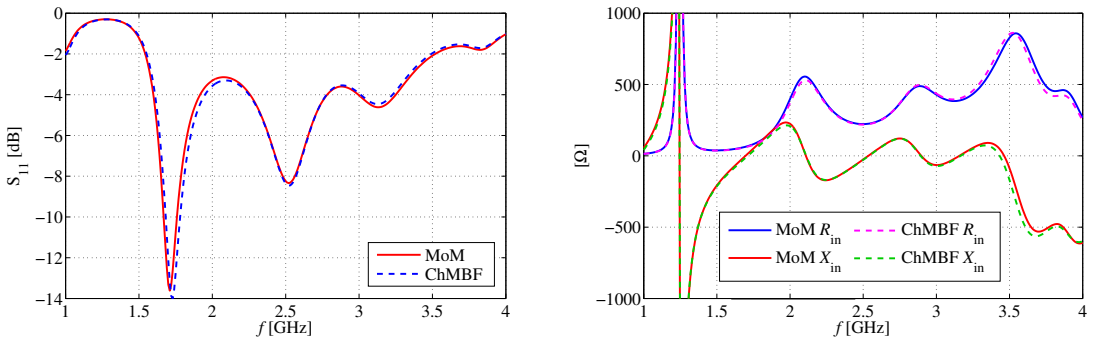

Figure 6.5: Input impedance computed by a direct solution of EFIE and by ChMBF method using all numerically obtained modes.

scatterer is computed by MATLAB function corrcoef [123, p. 41]. The correlation coefficients are computed for all modes considered on the patch motif at all frequencies.

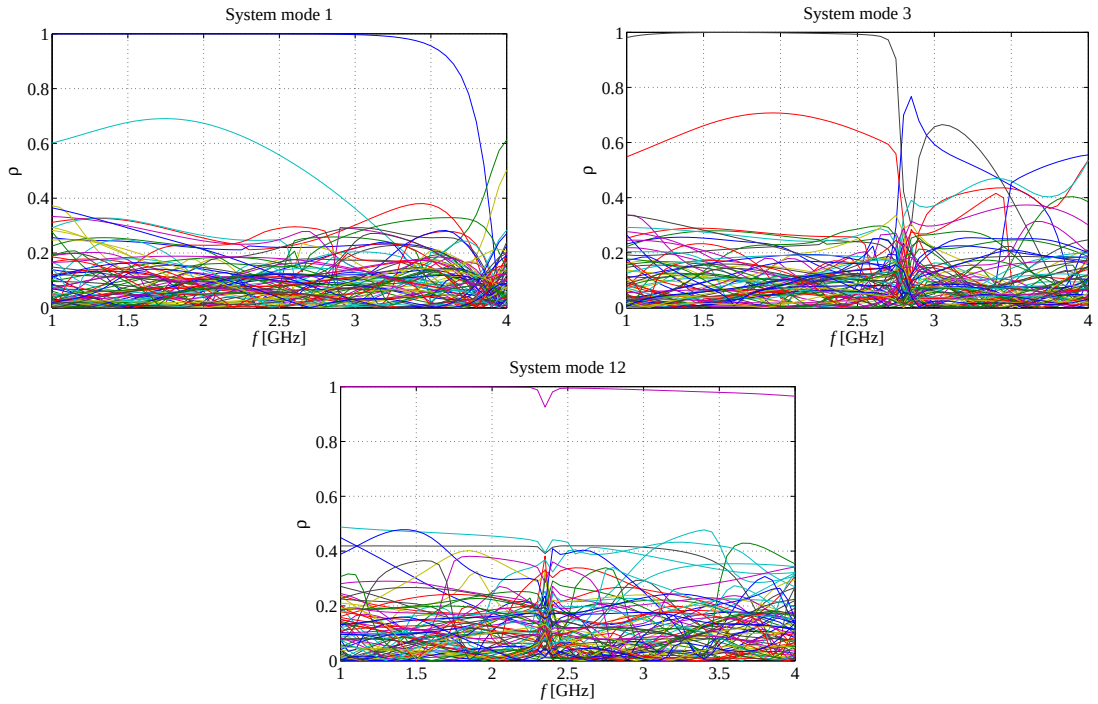

Figure 6.6: Correlation of all modes on SAU motif with modes 1, 3, and 12 of the system in Fig. 6.3.

Selected cases of the correlation coefficients are plotted in Fig. 6.6. Similar graphs can be generated for each mode of the system. It was observed, that the modes of the system may be dominantly correlated with a single mode of a scatterer. On the other hand, it is common, that there exist a frequency range, where a mode of the system is in fact constituted by a combination of several modes of its scatterers.

The above mentioned combining of the scatterers' modes may be confirmed by another approach. If the TCM is performed using the ChMBF method, we will obtain the expansion coefficients $\boldsymbol{c}_a$, which represent how the scatterer's modes are summed to constitute a system mode.

6.5 Investigating the Effect of an Infinite PEC and PMC Plane

The ChMBF method can be used to investigate the effect of a height of a planar motif over an infinite PEC or PMC[6] plane. These two cases are computed at once if the structure is mirrored over XY plane. The out-of-phase currents correspond to the PEC plane and the in-phase currents correspond to the PMC plane.

The ChMBF method can be applied on a single mode of a planar motif placed in height H over an infinite conducting plane. The eigenvalue equation (6.7) for single mode takes a simple form of

$$\begin{pmatrix} X_{11} & X_{12} \\ X_{12} & X_{22} \end{pmatrix} \begin{pmatrix} c_{a,1} \\ c_{a,2} \end{pmatrix} = \lambda_a \begin{pmatrix} R_{11} & R_{12} \\ R_{12} & R_{22} \end{pmatrix} \begin{pmatrix} c_{a,1} \\ c_{a,2} \end{pmatrix}, \tag{6.8}$$

where $X_{11} = X_{22} = \lambda_m$ and $R_{11} = R_{22} = 1$ and the off-diagonal elements are evaluated by (6.6). There exist two solutions of the equation, $c_{a,1} = c_{a,2}$ and $c_{a,1} = -c_{a,2}$ which represents the in-phase and out-of-phase currents (PEC and PMC planes). Associated with these two eigenvectors are the eigenvalues

$$\lambda_a^+ = \frac{\lambda_m + X_{12}}{1 + R_{12}}, \quad \lambda_a^- = \frac{\lambda_m - X_{12}}{1 - R_{12}}. \tag{6.9}$$

The eigenangles computed by TCM and by (6.8) are plotted in Fig. 6.7. It can be seen that the eigenvalues of a mirrored mode (PEC and PMC cases) oscillate about the eigenvalue λ_m of the mode in free space. With the increased height, more oscillations with smaller amplitude are observed within a fixed frequency range.

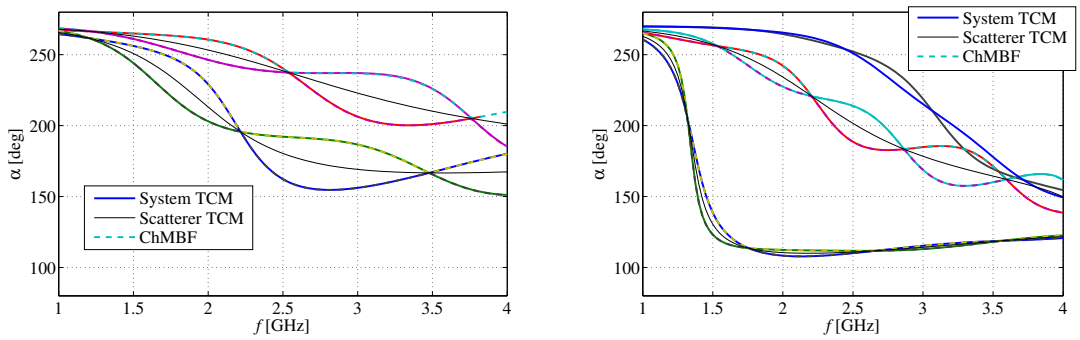

(a) Rectangular patch, $H = 50$ mm. (b) SAU, $H = 90$ mm.

Figure 6.7: Eigenangles of the mirrored configuration of scatterers.

[6] Perfect magnetic conductor.

While the eigenvalues computed by (6.8) and (6.9) are exactly the same, the second equation is more suitable for explaining the oscillations. It is intuitively expected, that the oscillations are caused by the evolution of coupling between the two modes with height. Using ChMBF, the coupling may be computed in terms of the off-diagonal terms of the modal impedance matrix, Fig. 6.8. It seams, that the oscillations occur independently on the current distribution, at least for the first two modes of a rectangular patch and the SAU motif, Fig. 6.8. It is therefore possible to address the behavior of the modal resonant frequency in Fig. 3.15 to the evolution of coupling, which for certain heights causes a very high sensitivity of f_{res} on H.

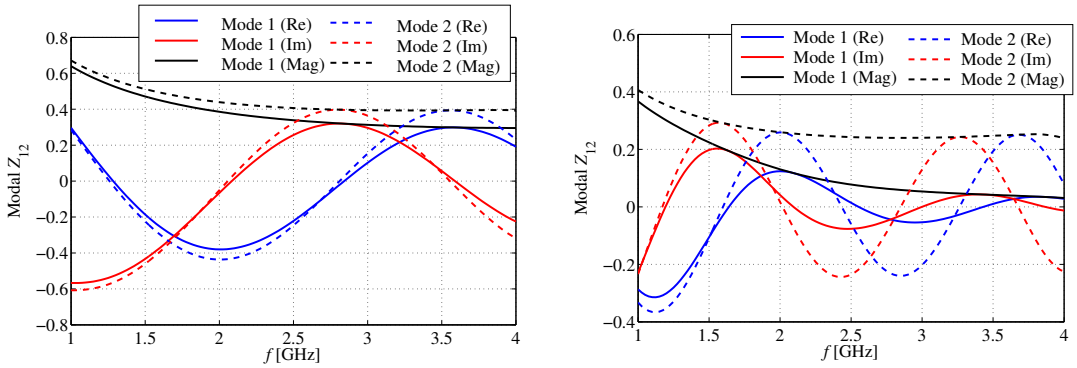

(a) Rectangular patch, $H = 50$ mm.

(b) SAU, $H = 90$ mm.

Figure 6.8: Frequency dependency of real part, imaginary part and magnitude of $Z_{21} = Z_{12}$.

6.6 Conclusion

A method of computing modes and antenna response to an excitation of a system of scatterers was derived and verified in this chapter. The key advantage of the ChMBF method is that it is able to quantify the coupling between individual modes of scatterers creating an antenna. The method can give accurate results if all modes were considered, which was demonstrated on a rectangular patch antenna and a SAU fractal motif fed by an L-probe. The procedure is particularly useful for antennas, where only several modes are dominantly excited. Than the ChMBF method provides information about relative amplitude of each mode, which can be clearly interpreted. It is possible to use the information e.g. to ensure equal excitation of two orthogonal on a motif to achieve a circular polarization.

The method has already been utilized for explaining the behavior of eigenvalues (and resonant frequency) of a patch above PEC and PMC infinite plane. A very good match

between ChMBF and TCM was observed and the oscillatory behavior of eigenvalues was addressed to the frequency behavior of mutual coupling between the patch and its image.

Although, numerical efficiency is not the main purpose of the method, it is interesting to note, that the smaller is the number of modes considered, the smaller matrix have to be inverted. Nonetheless, the elements of the modal $\mathbf{Z}$ matrix, which relate modes on different scatterers, have to be computed numerically. This fact may present computational advantage if the relative position of the scatterers have to be optimized.

7

Conclusion

7.1 Contributions of the Thesis

The most important contributions of the thesis are listed below:

- Designing a dual-band fractal antenna using the modal information and proposing a dual L-probe to match the antenna simultaneously in both bands, journal paper [64].
- Designing an active differentially fed antenna with a very low equivalent noise temperature, high CMMR, and wide bandwidth, conference paper [72].
- Explaining the effects of current distribution and height over an infinite PEC plane on resonant frequency and radiation quality factor of high-Q and low-Q modes through modal decomposition, journal paper [66].
- Developing a versatile surface mesh generation tool for the in-house modal analyzer, journal paper [73] (in review).
- Analyzing the effects of quadrature errors on the numerical computation of characteristic modes by the method of moments, journal paper [73] (in review).
- Formulating recommendations for a mesh refinement strategy, based on the error analysis, which have been verified in the in-house tool, as well as in the commercial FEKO package, journal paper [73] (in review).
- Deriving the ChMBF method for computing coupling coefficients between modes of individual scatterers.

7.2 Future Suggestions

Literature review, as well as the work contained in this thesis, indicate a rapidly increasing interest in the theory of characteristic modes. Significant attention is given to the usage of the TCM for MIMO antenna design and electrically small antennas. However, the potential application of TCM for intermediate size antennas, where several modes usually need to be used in combination, be is worth exploring. Frequency selective surfaces are also a lesser explored application of the TCM. Another appealing goal of modal design procedures is the utilization of TCM for active differentially fed antennas. Wideband stability, noise figure, gain and mixed mode S-parameters of such antennas have to be optimized simultaneously, and therefore, modal results may speedup the design process. To address these issues, ChMBF method has been proposed, however further research is necessary to solve the challenging problem of active antenna design.

From a computational point of view, routines for combined conducting bodies and dielectrics would increase the applicability of the modal approach and allow us to model more realistic geometries. Since the characteristic modes are closely related to the integral equations and method of moments, techniques, such as higher order basis functions or layered dielectrics, can be readily applied to TCM. Computation of modes by numerical techniques other than MoM is another largely unexplored research area. Certain improvements can also be reached in the eigenvalue tracking algorithms and criteria of modal significance in the sum of the modes. In particular, a method for obtaining the relative contribution of each mode without the necessity of computing all modes or direct EFIE solution will be of high interest.

Further research can also build up-on other authors' recent definitions of sub-structure and sub-system modes. It has already been shown, that these modes have similar properties to characteristic modes and can be utilized to design of antennas mounted on a PCB, or to reduce coupling between antenna elements. Rigorous study with regard to the physical meaning of parameters of these modes has yet to be conducted.

The work described in this thesis opened another area of research - a numerical convergence of the computational method based on EFIE and method of moments. It has already been shown that eigenvalue dependency on certain sources of error is quite different from the properties of a direct solution. However, rigorous handling of error sources in the TCM remains a challenge.

Index

References

[1] D. G. Swanson and W. J. R. Hoefer, *Microwave Circuit Modeling Using Electromagnetic Field Simulation*. Artech House, 2003.

[2] CST Computer Simulation Technology. [Online]. Available: www.cst.com

[3] ANSYS HFSS. [Online]. Available: www.ansys.com

[4] EM Software & Systems-S.A. FEKO. [Online]. Available: www.feko.info

[5] C. A. Balanis, *Antenna Theory Analysis and Design*, 3rd ed. John Wiley, 2005.

[6] COMSOL Multiphysics. [Online]. Available: www.comsol.com

[7] R. F. Harrington and J. R. Mautz, "Theory of characteristic modes for conducting bodies," *IEEE Trans. Antennas Propag.*, vol. 19, no. 5, pp. 622–628, Sept. 1971.

[8] P. Hazdra, "Planarni fraktalove antenni struktury," Ph.D. dissertation, CTU in Prague, 2009, (in czech).

[9] A. Taflove and S. C. Hagness, *Computational Electrodynamics: The Finite-Difference Time-Domain Method*. Artech House, 2004.

[10] J. L. Volakis, A. Chatterjee, and L. C. Kempel, *Finite Element Method Electromagnetics: Antennas, Microwave Circuits, and Scattering Applications*. Wiley-IEEE Press, 1998.

[11] R. F. Harrington, *Field Computation by Moment Methods*. John Wiley - IEEE Press, 1993.

[12] Y. Tretiakov and G. Pan, "Malvar wavelet based pocklington equation solutions to thin-wire antennas and scatterers," *Progress In Electromagnetics Research*, pp. 123–133, 2004.

[13] M. Cabedo-Fabres, E. Antonino-Daviu, A. Valero-Nogueira, and M. F. Bataller, "The theory of characteristic modes revisited: A contribution to the design of antennas for modern applications," *IEEE Antennas Propag. Magazine*, vol. 49, no. 5, pp. 52–68, Oct. 2007.

[14] B. A. Austin and K. P. Murray, "The application of characteristic-mode techniques to vehicle-mounted NVIS antennas," *IEEE Antennas Propag. Magazine*, vol. 40, pp. 7–21, 1998.

[15] A. Andujar, J. Anguera, and C. Puente, "Ground plane boosters as a compact antenna technology for wireless handheld devices," *IEEE Trans. Antennas Propag.*, vol. 59, no. 5, pp. 1668–1677, 2011.

[16] E. Antonino-Daviu, M. Cabedo-Fabres, M. Ferrando-Bataller, and V. M. R. Penarrocha, "Modal analysis and design of band-notched UWB planar monopole antennas," *IEEE Trans. Antennas Propag.*, vol. 58, pp. 1457–1467, 2010.

[17] R. Garbacz, "Modal expansions for resonance scattering phenomena," *Proceedings of the IEEE*, vol. 53, no. 8, pp. 856–864, Aug 1965.

[18] R. J. Garbacz, "A generalized expansion for radiated and scattered fields," Ph.D. dissertation, The Ohio State Univ., 1968.

[19] R. J. Garbacz and R. H. Turpin, "A generalized expansion for radiated and scattered fields," *IEEE Trans. Antennas Propag.*, vol. 19, no. 3, pp. 348–358, May 1971.

[20] R. F. Harrington and J. R. Mautz, "Computation of characteristic modes for conducting bodies," *IEEE Trans. Antennas Propag.*, vol. 19, no. 5, pp. 629–639, Sept. 1971.

[21] R. F. Harrington, J. R. Mautz, and Y. Chang, "Characteristic modes for dieletric and magnetic bodies," *IEEE Trans. Antennas Propag.*, vol. 20, no. 2, pp. 194–198, March 1972.

[22] Y. Chang and R. F. Harrington, "A surface formulation for characteristic modes of material bodies," *IEEE Trans. Antennas Propag.*, vol. 25, no. 6, pp. 789–795, Nov. 1977.

[23] R. F. Harrington and J. R. Mautz, "Characteristic modes for aperture problems," *IEEE Trans. Microwave Theory Tech.*, vol. 33, no. 6, pp. 500–505, June 1985.

[24] J. B. Knorr, "Consequences of symmetry in the computation of characteristic modes for conducting bodies," *IEEE Trans. Antennas Propag.*, vol. 21, no. 6, pp. 899–902, 1973.

[25] M. Cabedo-Fabres, "Systematic design of antennas using the theory of characteristic modes," Ph.D. dissertation, UPV, Feb. 2007.

[26] E. A. Daviu, "Analysis and design of antennas for wireless communications using modal methods," Ph.D. dissertation, UPV, Feb. 2008.

[27] E. Antonino-Daviu, M. Cabedo-Fabres, M. Gallo, M. F. Bataller, and M. Bozzetti, "Design of a multimode mimo antenna using characteristic modes," in *Proceedings of the 3rd European Conference on Antennas and Propagation (EUCAP)*, Berlin, Germany, March 2009, pp. 1840–1844.

[28] P. Hazdra and P. Hamouz, "On the modal superposition lying under the MoM matrix equations," *Radioengineering*, vol. 17, no. 3, pp. 42–46, Sept. 2008.

[29] P. Hamouz, P. Hazdra, M. Polivka, M. Capek, and M. Mazanek, "Radiation efficiency and Q factor study of franklin antenna using the theory of characteristic modes," in *Proceedings of the 5th European Conference on Antennas and Propagation (EUCAP)*, Rome, Italy, April 2011, pp. 1974–1977.

[30] P. Hamouz, M. Polivka, and P. Hazdra, "Efficiency treatment of two closely spaced metal sheets by characteristic mode theory," in *Antennas and Propagation, 2009. EuCAP 2009. 3rd European Conference on*, March 2009, pp. 178–181.

[31] J. Ethier and D. A. McNamara, "Modal significance measure in characteristic mode analysis of radiating structures," *Electronics Letters*, vol. 46, no. 2, pp. 107–108, Jan. 2010.

[32] ——, "Through the looking glass: A characteristic mode view of electromagnetic modeling & design," in *ANTEM-AMEREM*, July 2010, pp. 1–4.

[33] J. Ethier, "Antenna shape synthesis using characteristic mode concepts," Ph.D. dissertation, University of Ottawa, 2012.

[34] K. A. Obeidat, "Design methodology for wideband electrically small antennas based on the theory of characteristic modes," Ph.D. dissertation, Univ. of Illinois, 2010.

[35] B. D. Raines, "Systematic design of multiple antenna systems using characteristic modes," Ph.D. dissertation, The Ohio State University, 2011.

[36] J. Ethier and D. McNamara, "Sub-structure characteristic mode concept for antenna shape synthesis," *Electronics Letters*, vol. 48, no. 9, pp. 471–472, April 2012.

[37] R. Martens, E. Safin, and D. Manteuffel, "Inductive and capacitive excitation of the characteristic modes of small terminals," in *Loughborough Antennas & Propagation Conference*, 2011.

[38] R. Martens, J. Holopainen, E. Safin, J. Ilvonen, and D. Manteuffel, "Optimal dual-antenna design in a small terminal multiantenna system," *IEEE Antennas Wireless Propag. Lett.*, vol. 12, pp. 1700–1703, 2013.

[39] B. D. Raines and R. G. Rojas, "Wideband tracking of characteristic modes," in *Proceedings of the 5th European Conference on Antennas and Propagation (EUCAP)*, Rome, Italy, April 2011.

[40] ——, "Wideband characteristic mode tracking," *IEEE Trans. Antennas Propag.*, vol. 60, no. 7, pp. 3537–3541, July 2012.

[41] M. Capek, P. Hazdra, P. Hamouz, and J. Eichler, "A method for tracking characteristic numbers and vectors," *PIER-B*, vol. 33, pp. 115–134, 2011.

[42] E. Safin and D. Manteuffel, "Reconstruction of the characteristic modes on an antenna based on the radiated far field," *IEEE Trans. Antennas Propag.*, vol. 61, pp. 2964–2971, 2013.

[43] J. J. Adams and J. T. Bernhard, "Broadband equivalent circuit models for antenna impedances and fields using characteristic modes," *IEEE Trans. Antennas Propag.*, vol. 61, no. 8, pp. 3985–3994, 2013.

[44] A. Araghi and G. Dadashzadeh, "Oriented design of an antenna for MIMO applications using theory of characteristic modes," *IEEE Antennas Wireless Propag. Lett.*, vol. 11, pp. 1140–1143, 2012.

[45] J. Ethier and D. McNamara, "The use of generalized characteristic modes in the design of MIMO antennas," *Magnetics, IEEE Transactions on*, vol. 45, no. 3, pp. 1124–1127, March 2009.

[46] ——, "An interpretation of mode-decoupled MIMO antennas in terms of characteristic port modes," *Magnetics, IEEE Transactions on*, vol. 45, no. 3, pp. 1128–1131, March 2009.

[47] A. Krewski, W. Schroeder, and K. Solbach, "Bandwidth limitations and optimum low-band LTE MIMO antenna placement in mobile terminals using modal analysis," in *Antennas and Propagation (EUCAP), Proceedings of the 5th European Conference on*, April 2011, pp. 142–146.

[48] H. Li, Z. Miers, and B. K. Lau, "Generating multiple characteristic modes below 1GHz in small terminals for MIMO antenna design," in *Antennas and Propagation Society International Symposium (APSURSI), 2013 IEEE*, July 2013, pp. 180–181.

[49] Z. Miers, H. Li, and B. K. Lau, "Design of bandwidth-enhanced and multiband MIMO antennas using characteristic modes," *Antennas and Wireless Propagation Letters, IEEE*, vol. 12, pp. 1696–1699, 2013.

[50] A. Cabedo, J. Anguera, C. Picher, M. Ribo, and C. Puente, "Multiband handset antenna combining a PIFA, slots, and ground plane modes," *IEEE Trans. Antennas Propag.*, vol. 57, no. 9, pp. 2526–2533, 2009.

[51] M. Cabedo-Fabres, E. Antonino-Daviu, A. Valero-Nogueira, and M. Ferrando-Bataller, "Optimization of the polarization of reflectarrays using characteristic modes," in *Antennas and Propagation Society International Symposium, 2004. IEEE*, vol. 1, June 2004, pp. 13–16 Vol.1.

[52] Y. Chen and C.-F. Wang, "Synthesis of reactively controlled antenna arrays using characteristic modes and DE algorithm," *IEEE Antennas Wireless Propag. Lett.*, vol. 11, pp. 385–388, 2012.

[53] J. Ethier, M. Chaharmir, J. Shaker, and D. Lee, "Development of novel low-cost reflectarrays [antenna applications corner]," *Antennas and Propagation Magazine, IEEE*, vol. 54, no. 3, pp. 277–287, June 2012.

[54] S. Wang and H. Arai, "Analysis of an optimized notch array antenna by using the theory of characteristic modes," *Antennas and Wireless Propagation Letters, IEEE*, vol. 13, pp. 253–256, 2014.

[55] Y. Chen and C.-F. Wang, "Synthesis of platform integrated antennas for reconfigurable radiation patterns using the theory of characteristic modes," in *In proceedings of 10th International Symposium on Antennas, Propagation & EM Theory (ISAPE - 2012)*, 2012.

[56] ——, "Electrically small UAV antenna design using characteristic modes," *IEEE Trans. Antennas Propag.*, vol. 62, no. 2, pp. 535–545, 2014.

[57] J. Ethier and D. McNamara, "Multiband antenna synthesis using characteristic mode indicators as an objective function for optimization," in *Wireless Information Technology and Systems (ICWITS), 2010 IEEE International Conference on*, Aug 2010, pp. 1–4.

[58] F. Gallee, T. Bernabeu, M. Cabedo-Fabres, E. Daviu, and A. Nogueira, "Application of the theory of characteristic modes to the design of compact metallic strip antenna with multilayer technology (LTCC)," in *Antennas and Propagation (EuCAP), 2013 7th European Conference on*, April 2013, pp. 1891–1895.

[59] M. Hilbert, M. Tilston, and K. Balmain, "Resonance phenomena of log-periodic antennas: characteristic-mode analysis," *Antennas and Propagation, IEEE Transactions on*, vol. 37, no. 10, pp. 1224–1234, Oct 1989.

[60] K. Obeidat, B. Raines, R. Rojas, and B. Strojny, "Design of frequency reconfigurable antennas using the theory of network characteristic modes," *Antennas and Propagation, IEEE Transactions on*, vol. 58, no. 10, pp. 3106–3113, Oct 2010.

[61] W. Wu, B.-Z. Wang, X.-S. Yang, and Y. Zhang, "A pattern-reconfigurable planar fractal antenna and its characteristic-mode analysis," *Antennas and Propagation Magazine, IEEE*, vol. 49, no. 3, pp. 68–75, June 2007.

[62] Y. Chen and C.-F. Wang, "Characteristic-mode-based improvement of circularly polarized U-slot and E-shaped patch antennas," *IEEE Antennas Wireless Propag. Lett.*, vol. 11, pp. 1474–1477, 2012.

[63] W. Wu and Y.-P. Zhang, "Analysis of ultra-wideband printed planar quasi-monopole antennas using the theory of characteristic modes," *Antennas and Propagation Magazine, IEEE*, vol. 52, no. 6, pp. 67–77, Dec 2010.

[64] J. Eichler, P. Hazdra, M. Capek, T. Korinek, and P. Hamouz, "Design of a dual-band orthogonally polarized l-probe-fed fractal patch antenna using modal methods," *IEEE Antennas Wireless Propag. Lett.*, vol. 10, pp. 1389–1392, 2011.

[65] J. Eichler, "Multiband antenna with a fractal motif," Master's thesis, Czech Technical University in Prague, Prague, Czech Republic, 2010, (in czech).

[66] J. Eichler, P. Hazdra, M. Capek, and M. Mazanek, "Modal resonant frequencies and radiation quality factors of microstrip antennas," *International J. of Antenas and Propag.*, vol. 2012, pp. 1–9, 2012.

[67] G. A. E. Vandenbosch, "Reactive energies, impedance, and Q factor of radiating structures," *IEEE Trans. Antennas Propag.*, vol. 58, no. 4, pp. 1112–1127, Apr. 2010.

[68] M. Capek, P. Hazdra, and J. Eichler, "A method for the evaluation of radiation Q based on modal approach," *IEEE Trans. Antennas Propag.*, vol. 60, no. 10, pp. 4556–4567, Oct. 2012.

[69] S. M. Rao, D. R. Wilton, and A. W. Glisson, "Electromagnetic scattering by surfaces of arbitrary shape," *IEEE Trans. Antennas Propag.*, vol. 30, no. 3, pp. 409–418, May 1982.

[70] S. N. Makarov, *Antenna and EM Modeling with Matlab*. John Wiley, 2002.

[71] M. Capek, P. Hamouz, P. Hazdra, and J. Eichler, "Implementation of the Theory of Characteristic Modes in Matlab," *IEEE Antennas Propag. Magazine*, vol. 55, no. 2, pp. 176–189, April 2013.

[72] J. Eichler, D. Segovia-Vargas, P.Hazdra, M. Capek, and V. Gonzalez-Posadas, "Active low noise differentially fed dipole antenna," in *10th International Symposium on Antennas, Propagation & EM Theory (ISAPE - 2012)*, 2012.

[73] J. Eichler, P. Hazdra, and M. Capek, "Aspects of mesh generation for characteristic mode analysis," *IEEE Antennas Propag. Magazine*, (in review).

[74] R. F. Harrington, *Time-Harmonic Electromagnetic Fields*, 2nd ed. John Wiley - IEEE Press, 2001.

[75] D. Liu, R. J. Garbacz, and D. M. Pozar, "Antenna synthesis and optimization using generalized characteristic modes," *IEEE Trans. Antennas Propag.*, vol. 38, no. 6, pp. 862–868, June 1990.

[76] E. Newman, "Small antenna location synthesis using characteristic modes," *IEEE Trans. Antennas Propag.*, vol. 27, no. 4, pp. 530–531, July 1979.

[77] A. D. Yaghjian and S. R. Best, "Impedance, bandwidth and Q of antennas," *IEEE Trans. Antennas Propag.*, vol. 53, no. 4, pp. 1298–1324, April 2005,

[78] M. Capek, L. Jelinek, P. Hazdra, and J. Eichler, "The measurable q factor and observable energies of radiating structures," *Antennas and Propagation, IEEE Transactions on*, vol. 62, no. 1, pp. 311–318, Jan 2014.

[79] R. F. Harrington and J. R. Mautz, "Control of radar scattering by reactive loading," *IEEE Trans. Antennas Propag.*, vol. 20, no. 4, pp. 446–454, July 1972.

[80] S. J. Orfanidis. Electromagnetic waves & antennas. [Online]. Available: www.ece.rutgers.edu/~orfanidi/ewa

[81] W. C. Gibson, *The Method of Moments in Electromagnetics*, 1st ed. Chapman and Hall/CRC, 2007.

[82] A. O. Yee and R. J. Garbacz, "Self- and mutual-admittances of wire antennas in terms of characteristic modes," *IEEE Trans. Antennas Propag.*, vol. 21, no. 6, pp. 868–871, Nov. 1973.

[83] M. Capek, J. Eichler, and P. Hazdra, "Evaluating radiation efficiency from characteristic currents," *IET Microw. Antennas Propag.*, (in review).

[84] P. Hazdra, M. Mazanek, and J. Cermak, "Wideband rectangular microstrip patch antenna using L-probe feeding system," *Radioengineering*, vol. 16, no. 3, pp. 37–41, 2007.

[85] The MathWorks. The Matlab. [Online]. Available: www.mathworks.com

[86] M. Capek, P. Hazdra, P. Hamouz, and M. Mazanek, "Software tools for efficient generation, modelling and optimisation of fractal radiating structures," *IET Microw. Antennas Propag.*, vol. 5, no. 8, pp. 1002–1007, 2011.

[87] K. J. Falconer, *Fractal Geometry – Mathematical Foundations and Applications.* John Wiley, 2003.

[88] S. N. Sinha and N. Jain, "A self-affine fractal multiband antenna," *IEEE Antennas and Wireless Propag. Letters*, vol. 6, pp. 110–112, 207.

[89] CST Microwave Studio. http://www.cst.com/.

[90] J. Anguera, "Fractal and broadband techniques on miniature, multifrequency, and high-directivity microstrip patch antennas," Ph.D. dissertation, Dept. Signal Theory Commun., UPC, Barcelona, Spain, 2003.

[91] J. L. Volakis, C. Chen, and K. Fujimoto, *Small Antennas: Miniaturization Techniques & Applications.* McGraw-Hill, 2010.

[92] J. S. McLean, "A re-examination of the fundamental limits on the radiation Q of electrically small antennas," *IEEE Trans. Antennas Propag.*, vol. 44, no. 5, pp. 672–675, May 1996,

[93] D. R. Rhodes, "Observable stored energies of electromagnetic systems," *J. Franklin Inst.*, vol. 302, no. 3, pp. 225–237, 1976.

[94] ——, "A reactance theorem," *Proc. R. Soc. Lond. A.*, vol. 353, pp. 1–10, Feb. 1977,

[95] J. F. Shaeffer, "Mom3d method of moments code theory manual," Denmar, Marietta, Georgia, NAS1-18603 Rep. 189594, 1992.

[96] P. Arcioni, M. Bressan, and L. Perregrini, "On the evaluation of the double surface integrals arising in the application of the boundary integral method to 3-D problems," *IEEE Trans. Microwave Theory Tech.*, vol. 44, no. 3, pp. 436–438, March 1997.

[97] P. Bhartia, I. Bahl, R. Garg, and A. Ittipiboon, *Microstrip Antenna Design Handbook.* Norwood, Mass, USA: Artech House, 2000.

[98] J. R. James, P. S. Hall, and C. Wood, *Microstrip Antenna Theory and Design.* Peter Peregrinus Ltd., 1981.

[99] P. Hazdra, M. Capek, and J. Eichler, "Radiation Q-factors of thin-wire dipole arrangements," *IEEE Antennas Wireless Propag. Lett.*, vol. 10, pp. 556–560, 2011.

[100] C. Mak, K. Luk, K.-F. Lee, and Y. Chow, "Experimental study of a microstrip patch antenna with an L-shaped probe," *Antennas and Propagation, IEEE Transactions on*, vol. 48, no. 5, pp. 777–783, 2000.

[101] K. Chang, R. A. York, P. S. Hall, and T. Itoh, "Active integrated antennas," *IEEE Trans. Microwave Theory Tech.*, vol. 50, no. 3, pp. 937–944, 2002.

[102] W. R. Eisenstadt, B. Stengel, and B. M. Thompson, *Microwave Differential Circuit Design Using Mixed-Mode S-Parameters.* Artech House, 2006.

[103] D. E. Bockelman and W. R. Eisenstadt, "Combined differential and common-mode scattering parameters: Theory and simulation," *IEEE Trans. Microwave Theory Tech.*, vol. 43, no. 7, pp. 1530–1539, 1995.

[104] W. R. Deal, V. Radisic, Y. Qian, and T. Itoh, "Integrated-antenna push-pull power amplifiers," *IEEE Trans. Microwave Theory Tech.*, vol. 47, no. 8, pp. 1418–1425, 1999.

[105] K. Chan, E. Lee, P. Gardner, and T. Dodgson, "Differential aperture coupling technique for passive and active integrated antenna design," *IET Microw. Antennas Propag.*, vol. 1, no. 2, pp. 458–464, 2007.

[106] D. M. Pozar, "Microstrip antenna aperture coupled to a mictrostrip line," *Electronics Letters*, vol. 21, no. 2, pp. 49–50, 1985.

[107] M. Edwards and J. Sinsky, "A new criterion for linear 2-port stability using a single geometrically derived parameter," *IEEE Trans. on Microw. Theory Tech.*, vol. 40, no. 12, pp. 2303–2311, 1992.

[108] AWR. [Online]. Available: web.awrcorp.com

[109] O. Garcia-Perez, D. Segovia-Vargas, L. E. Garcia-Munoz, J. L. Jimenez-Martin, and V. Gonzalez-Posadas, "Broadband differential low noise amplifier for active differential arrays," *IEEE Trans. Microwave Theory Tech.*, vol. 59, pp. 108–115, 2011.

[110] Partial Differential Equation Toolbox. [Online]. Available: www.mathworks.com/help/toolbox/pde/ug/pdetool.html

[111] NETGEN. [Online]. Available: www.hpfem.jku.at/netgen/

[112] Computational Geometry Algorithms Library. [Online]. Available: www.cgal.org

[113] P.-O. Persson and G. Strang, "A simple mesh generator in MATLAB," *SIAM Review*, vol. 42, pp. 329–345, 2004.

[114] P.-O. Persson, "Mesh generation for implicit geometries," Ph.D. dissertation, MIT, 2006.

[115] (2014, February) Meshgen webpage. [Online]. Available: http://elmag.org/sites/default/files/users/eichler/files/MeshGenV03p.zip

[116] P. Kravanja, T. Sakurai, H. Sugiura, and M. V. Barel, "A perturbation result for generalized eigenvalue problems and its application to error estimation in a quadrature method for computing zeros of analytic functions," *Journal of Computational and Applied Mathematics*, vol. 161, pp. 339–347, 2003.

[117] D. J. Ludick, E. Lezar, and U. Jakobus, "Characteristic mode analysis of arbitrary electromagnetic structures using FEKO," in *ICEAA*, 2012, pp. 208–211.

[118] J. C. Rautio, "An investigation of an error cancellation mechanism with respect to subsectional electromagnetic analysis validation," *International Journal of Microwave and Millimeter-Wave Computer-Aided Engineering*, vol. 6, pp. 430–435, 1996.

[119] E. F. Kuester and D. D. Chang, "Closed-form expressions for the current or charge distribution on parallel strips or microstrip," *IEEE Trans. Microwave Theory Tech.*, vol. 28, no. 3, pp. 254–259, 1980.

[120] K.-L. Wong, *Compact and Broadband Microstrip Antennas*. John Wiley & Sons, 2002.

[121] V. V. S. Prakash and R. Mittra, "Characteristic basis function method: A new technique for efficient solution of method of moments matrix equations," *Microwave and Optical Technology Letters*, vol. 36, no. 2, pp. 95–100, 2003.

[122] M. Cabedo-Fabres, E. Antonino-Daviu, D. Escuderos, and V. Rodrigo-Penarrocha, "On the application of characteristic modes for the analysis of large scale antenna problems," in *Antennas and Propagation, 2007. EuCAP 2007. The Second European Conference on*, Nov 2007, pp. 1–7.

[123] N. R. Draper and H. Smith, *Applied Regresion Analysis*, 3rd ed. John Wiley & Sons, 1998.